Detection of a Local Mass Anomaly in the Shallow Subsurface by Applying a Matched Filter

by

Tin Lian Abt

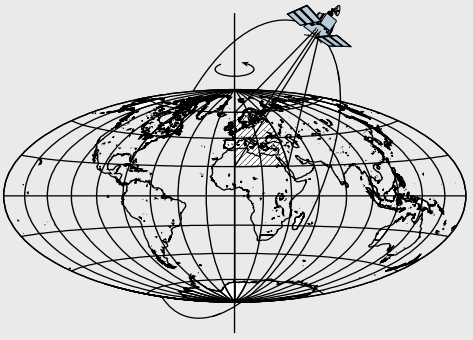

Report No. 497

Geodetic Science

The Ohio State University
Columbus, Ohio 43210

August 2011

PREFACE

This report was prepared for and submitted to the Graduate School of the Ohio State University as a dissertation in partial fulfillment of the requirements for the PhD degree.

Abstract

The task is to locate a mass anomaly, particularly a void, in the near subsurface based on gravity, gravity gradients, and magnetic field data. The motivation for this search rises from multiple areas of applications such as urban planning, mining, archeology, and extraterrestrial science. Assuming that the signal generated by the sought mass anomaly is approximately known and can be described by the signal of a three-dimensional prism, a Matched Filter (MF) is implemented to detect this signal buried in the relatively strong noise of the geologic background. The background noise is described in the filter function by covariances. One important aspect of the current study is, therefore, to derive the covariance matrix that accounts for the relation between gravity, gravity gradients, and the magnetic field. It turns out that the choice of covariance function can have a significant influence on the MF performance. The aim of this research is to answer some fundamental questions regarding the various combinations of data types, the estimation of the depth or orientation of the mass anomaly, as well as the optimal number of observed profiles. All tests are carried out by Monte Carlo simulations, which include randomized simulated background fields. In addition, a statistical interpretation based on the Neyman-Pearson hypothesis test is provided. It determines the probabilities that either a sought anomaly is not detected or that some background noise is mistaken for the sought anomaly. The simulation results lead to the conclusion that the MF is a very strong tool to detect the sought anomaly along an observed profile as it searches for the maximum Signal-to-Noise ratio. Therefore, the MF is able to detect anomalies buried in the background noise even if they are not directly visible in the data set. A data set of either gravity gradients or the magnetic field leads to more successful detections compared to a data set of gravity. The combination of several gravity gradient components as well as the magnetic field further improves the filter performance. The MF is highly sensitive to the depth of the sought anomaly but far less sensitive to its horizontal orientation. As a consequence, it is possible to determine a rough estimate for the depth but not for the orientation, which, however, can be approximated by measuring multiple profiles.

Acknowledgments

First and foremost, I would like to thank my Advisor, Dr. Chris Jekeli, for his guidance and support throughout my entire stay here at The Ohio State University. It has been a great experience working with him and I also gained tremendously from his phenomenal classes. Furthermore, I wish to thank Dr. C.K. Shum and Dr. Ralph von Frese for their help as committee members, class instructors, and great experts in their fields. I appreciate the open doors whenever I needed advice. Acknowledgments to my fellow students in the Geodetic Science and Surveying program for all the fruitful discussions that contributed to this research as well as the joyful evenings at our Geodetic Dinners. I am grateful for the many graduate students in the School of Earth Sciences, who introduced me to the American way of college life. Thank you for the great friendships and the lasting special memories. I am blessed to have met the wonderful people at St. Thomas More Newman Center, who became a true inspiration to my life. Thank you to Myra Dvoroznak and her family for inviting me to their home every Thanksgiving. I would also like to thank the OSU Co-ed Field Hockey Club. I feel honored to be part of this team. Many thanks to Kara, Maya, Melli, and Caitlin. Our long runs along the Olentangy river helped me clear my head from time to time. Finally, a huge thank you goes to my family, Tieneke & Otto Abt, and Jochen Bantle for their endless love and support.

Table of Contents

Chapter 1: Introduction

Geodesy on a global scale aims to determine the size and the shape of the Earth as well as their variations over time. A key property is thereby the gravity field, which is mainly influenced by the geometry, rotation, mass types, and mass distributions of the planet. Satellite missions such as CHAMP (CHAllenging Minisatellite Payload) [Reigber et al., 2003], GRACE (Gravity Recovery and Climate Experiment) [Tapley et al., 2004], and GOCE (Gravity field and steady-state Ocean Circulation Explorer) [Rummel et al., 2000] have specifically been designed and launched to observe the gravity field. On a regional or local scale, the acquisition of airborne and ground gravity data is not only of geodetic interest but also touches fields of geophysical explorations. In addition to the local determination of the geoid there is emphasis on understanding the structure of the subsurface and locating mass anomalies. A typical geophysical exploration project is the search for natural resources (oil, gas, coal) that occur at various depths in the Earth's crust. While this involves anomalies at depths of a couple of kilometers, which lies in the range of, for example, a seismic survey, local gravity gradient observations in contrast are mainly sensitive to the signals in the shallow subsurface ($< 100\,\mathsf{m}$). Exploring the near underground is a common task in many engineering and environmental applications. Based on this background, the scope of this dissertation is to localize a mass anomaly in the shallow subsurface by acquiring ground gravity data. Those data sets are enhanced by the observation of the spatial changes in gravity, i.e. the gravity gradients, and by the observation of the magnetic field. Gravity, gravity gradients, and magnetic field form some of the most fundamental properties of the Earth, which can be investigated without requiring any active sensors. Due to the local scale, the observations are not only sensitive to the sought anomaly but also to any variation in the geologic background of the local environment. This research concentrates on those cases at the edge where the signal of a sought mass anomaly is so weak that it is buried in the noise of the geologic background and where the application is directed to measure only a single or a few profiles of data across the anomaly. Hence, the sought signal is not imminently visible in the observed data set. A filtering process is required to localize the mass anomaly in the data. The Matched Filter (MF) is thereby considered advantageous over other filters as it looks for the maximum Signal-to-Noise Ratio (SNR) [Dumrongchai, 2007].

Most commonly, the mass anomaly is characterized by its low density compared to the surroundings such as an air-filled or water-filled cave in a limestone rock. The void is a special case of interest as it occurs in the majority of detection applications.

1.1 Applications for Void Detections

The search for those local mass anomalies, in particular voids, is a fundamental task, which finds its use in various environments, ranging from engineering problems to extraterrestrial science projects. Depending on the context, an underground void can either be a natural feature or a man-made construction. The following subsections present a summary of the major detection applications and introduce samples from the real world.

1.1.1 Hazard Analysis

Voids in the shallow subsurface pose hazards in urban areas as they may result in a collapse of land. Locating and delineating these voids is, therefore, an important aspect of a safety plan for urban areas or of a construction plan before the urbanization. Tests have, for example, been carried out in northern California, USA, to identify underground tubes produced by previous lava flows [FHWA, 2005]. Mapping those tubes is crucial for the construction and maintenance of future roads. Neglecting underground hazards in urban planning can lead to serious problems as reported in the Ebro Basin, Spain [Benito et al., 1995]. There, large damages to buildings and highways have already occurred caused by the formation of sinkholes. The underground in this area consists of gypsum karst mantled by alluvial deposits. Caves are produced from karstic processes and a mechanical erosion of the alluvial cover might lead to a collapse of these caves. Therefore, locating all voids helps to identify areas where sinkholes are likely to occur. The prediction of evolving sinkholes is also an issue in an area near the Dead Sea, where resorts, highways and a dam are in danger [Rybakov et al., 2005]. This is due to gravel sinkholes in alluvial fans and mud sinkholes in clay deposits.

Another type of hazard is generated by the subsurface conduits in the Woodville Karst Plain, Florida, USA [Chicken et al., 2008]. Those conduits transport water polluted from the urban areas to the nature preserves. In order to protect the environment the waterways of that area need to be understood. This requires that all relevant conduits are located and equipped with water monitoring devices.

1.1.2 Mining

The search for mass anomalies is related to all different aspects of mining. It can either mean to search for deposits directly, as, for example, [Keating, 1995] implements a

method to locate kimberlite pipes in the Kirkland Lake region, Ontario, Canada. Kimberlites are known as a possible source of diamonds. Or mass anomalies indicate danger areas in a mine, as, for example, [Gritto, 2005] tries to find gas-filled zones, which may trigger explosions due to the excavations of a coal mine. In addition, [Crouch et al., 1980] also point out that voids of abandoned underground coal-mines can be used as a source of drinking water supply.

1.1.3 Archeology

Underground voids might be man-made structures of archeological interest. While urbanization or agricultural treatment have likely destroyed any evidence in the topography, unmapped underground structures still exist. An affirmation for this is provided by an investigation site in Cornwall, Great Britain, where a fogou surrounded by a round enclosure as well as two additional void features are suspected in the subsurface [Linford, 1998]. A further void detection of archeological value is the search for air-filled cavities in Honduras [Luke et al., 1997]. Those cavities might contain burials of pre-Columbian settlements. Locating the cavities is, in this instance, helpful to guide the actual site excavations.

1.1.4 Border Tunnel

Hidden tunnels under the border are built and used by smugglers and illegal immigrants. [Allen et al., 2008] try to find a technique how to detect those unknown tunnels, for example, under the US border to Mexico and Canada.

1.1.5 Extraterrestrial Research

Caves are known for their own microclimate. Finding caves on Mars is an important approach in the search for life on Mars since they provide a protection of the harsh environmental conditions on the surface. This is the major aspect of the cave detection research by [Wynne et al., 2009]. Furthermore, the caves could also contain drinking water, oxygen, and hydrogen fuel resources for a future manned mission. A cave could even be the base for constructing a permanent station on Mars.

1.2 Sensors used in Previous Research

The applications introduced in Section 1.1 have the common aim to detect a local mass anomaly in the shallow subsurface. The type of acquired data, however, might differ for each individual project. While geodesy puts an emphasis on gravity surveys, a large range of geophysical techniques based on various sensors exists to collect local ground data. The most common methods are described in the classic textbook literature such as [Sharma, 1997], [Parasnis, 1997], [Telford et al., 1990], [Sharma, 1976],

[Dobrin and Savit, 1988], and [Burger et al., 2006]. A brief discussion about the possible sensors is presented in the following although this dissertation focuses only on the basic data, namely the gravity and magnetic field of the Earth. The presented overview of sensors serves as an introduction to alternatives that one day might be tied to geodetic gravity surveys but for now are considered less suitable for this particular void detection problem. All methods have in common that they are non-destructive – in contrast to drilling or excavation – and that they can be applied locally.

Gravity. The most straightforward approach to detect a mass anomaly is measuring the variation in gravity caused by the density contrast of the anomaly. The measurement setup is very simple as only one instrument, a relative gravimeter, is needed. The magnitude of the gravity anomaly is, however, much smaller than the overall gravity field of the Earth, which requires sensitive instrument care and precise fieldwork. This technique is, therefore, also referred to as microgravity. If the observation profile is not level, elevation corrections must be applied.

The major difficulty with gravimetry is that it poses an inverse problem of the potential field. While a geometric shape uniquely defines its gravity effect, an identical gravity field can be generated by unknown combinations of different sources. As a consequence, the interpretation of data might be challenging. The geologic background information as well as a table for rock type and mineral densities become relevant. Gravity gradiometry enhances the classic gravimetry as it adds more spatial information to the data. Furthermore, it emphasizes the short wavelengths of the signal and is, therefore, predisposed to show sharper contrasts in the data and to better delineate the contours of the mass anomaly. The main difficulty here is that, as a spatial derivative of the gravity vector, gravity gradiometer signals are even weaker than those of a gravity survey. That requires extra care when operating the highly sensitive instrument. While gravimeters (Section 2.2.1) are robust and mature instruments, applicable local gradiometers (Section 2.2.2) are still under development.

Magnetic. The principles of the magnetic survey are very similar to those of gravimetry since the magnetic potential is related to the gravitational potential (Section 2.1.3). The measurement setup is simple and only one instrument is utilized, a portable proton or a fluxgate magnetometer (Section 2.2.3). The observed magnetic field is a vector quantity consisting of the total field intensity and direction. The directional component makes the correct interpretation of the magnetic data even more difficult than the interpretation of the gravity data. An additional aspect is to ensure that no remanent properties or other magnetic sources disturb the field observations or if they do the observations need to be corrected. These effects are difficult to model. Furthermore, magnetization is generally low in sedimentary rocks and only moderate in soils. The signal generated by the mass anomaly is, therefore,

expected to be small but still within the measurable range of a magnetometer (order of $0.1\,\mathsf{nT}$).

Seismic. For the seismic method, seismic waves are generated, for example, by dropping a weight or by causing a small explosion, and observing the wave propagation over time. A void, for example, produces an anomalous perturbation in the travel-time curves. Refraction, reflection and resonance surveying distinguish the common seismic techniques. The first two techniques are successfully used for larger depths (e.g. search for oil) but detecting a small mass anomaly in the shallow subsurface is far more difficult. The low frequency (long wavelength) of the seismic waves might miss the small mass anomaly of a few cubic meters. Even if it is possible to determine the location of a void, its delineation still remains a challenge. An advanced spectral analysis is required. The major drawback of the seismic method (in contrast to gravity or magnetic) is its cost intensity and that the placing of geophones is rather laborious. Depending on the environmental conditions, nearby traffic or winds can further deteriorate the measurements.

Self-Potential. This technique lies among the electric methods such as induced polarization, resistivity and conductivity, but the electric current is here not generated artificially. The self-potentials of the Earth are also called spontaneous or natural potentials and are produced in the subsurface by either electrochemical actions between mineral and fluids or by electrokinetic processes based on ionic flows. The different potentials that can be observed are electrofiltration, thermoelectric, electrochemical, and mineralization potential. The measurement setup simply consists of two electrodes and a voltmeter to determine the potential gradients (differences in voltage). This allows for a rapid and inexpensive survey. The wires can be unpractical in the field though. A subsurface cave defines, for example, a basin for the groundwater flow. This results in a self-potential anomaly (accumulation of ions) and can be detected in the observed data. Heavy rainfall, on the other hand, might corrupt the interpretation of the data.

Induced Polarization. An electric current is temporarily applied to the ground. When the current is switched off, a fractional voltage is observed, which decays to zero. The ratio between the fractional and the original voltage describes the concentration of metallic minerals in the ground. The ionic conduction path in the ground is hindered by the mineral particles, in which the current is based on electrons. This leads to an accumulation of ions observed as the fractional voltage. Clay particles show a similar effect. This method is often utilized to search for groundwater.

Resistivity. In order to measure the resistivity of the subsurface (reciprocal of electrical conductivity), an artificial electric current is applied to the ground by a set

of electrodes. An additional set of electrodes observes then the potential differences. The apparent resistivity is determined by the observations and the specific positioning pattern of the electrodes. Voids will change the resistivity in contrast to an ideal homogeneous underground layer. However, deteriorations are also caused by the natural variations in the Earth's resistivity and other inhomogeneities in the ground. The resistivity method is relatively tedious since the electrodes need to be distributed while shallow anomalies require small electrode spacing.

Electromagnetic Conductivity. The basic idea is to induce an electromagnetic field in the subsurface. This primary field spreads out and induces a secondary electromagnetic field in the conductive materials of the subsurface. Measuring the resulting field provides information about the subsurface conductors. Materials that drastically enhance the conductivity within the Earth are fluids and metals. That means this is an appropriate method to detect salt-water-filled caves or tunnels that contain wires. A void, on the other hand, will be difficult to distinguish from the surrounding materials, except if the surrounding material is, for example, clay, or other materials of good conductivity. Advantages of this technique are its rapid use as the instrument does not require ground contact and its simple setup as no cables are needed.

GPR. The concept of Ground Penetrating Radar (GPR) is similar to the seismic reflection method. In this case, radio waves, which are part of the electromagnetic spectrum, are transmitted to the ground and their reflections are observed. The resulting travel-time curves map out the boundaries between subsurface features of different dielectric properties. GPR presents a rapid and high resolution method, where its depth is usually limited to the shallow subsurface. Restrictions are similar to those of the electromagnetic conductivity observations. GPR works well for ice, dry sand, and gravel but does not penetrate materials of high conductivity such as clay. This is a major drawback in case of a wet underground.

Radioactivity. This only requires a passive sensor since radioactivity is present in most of the rocks and minerals although only at a low level. The radioactive signature determines the underground rock type. The most basic instrument is the Geiger counter, which often records the radiation intensity as counts per minute. Topography, weathering, and background radiation can have disturbing effects on the observations. In geophysics, the radioactivity technique is mainly utilized to monitor movements of fluids in conjunction with groundwater and soil contamination. Radioactivity can also be used in faults and fracture zones but its usage in void detection is not obvious.

Geothermal. Nowadays, it is common to acquire geothermal data by infrared surveys. Thermal anomalies are, for example, found at cave entrances as the temperature of the entrance rock differs from the temperature of the surrounding rock. However, a correct thermal interpretation is very complex.

Many previous researches have studied and applied the above geophysical techniques to detect a void. The conclusion is that a single ideal technique does not exist since all techniques struggle with their specific difficulties. However, none of the above techniques can be completely dismissed either. Table 1.1 gives references to some of the previous void detection researches and their specific scope of techniques.

1.3 Current Approach and Outline

The task of this dissertation is to elaborate an effective solution to the localization of a void by suggesting the type of sensor, filter technique, and statistical interpretation from a geodetic point of view.

As shown in Section 1.2, the search for voids in the shallow subsurface has a broad range of practical applications. This dissertation will provide an approach on detecting a mass anomaly (void) in general, i.e. solving the geophysical inverse problem. The only specifications are that the mass anomaly is of very local dimensions (several meters), it has a horizontal, linear structure and its shape is simple enough to be approximated by a three-dimensional prism or a cylinder. These specifications cover most of the before mentioned applications. Depending on the characteristics of the mass anomaly and the environmental condition in each case, certain sensors are more successful than others. However, a general conclusion in many cases is to utilize a combination of two or more sensors. Here, the combination of gravity, gravity gradient, and magnetic field data are explored. Gravimetry and magnetometry are the most fundamental techniques in geophysics. They only require passive sensors, are robust to the weather conditions, cost-effective, and easy to apply. Adding the gravity gradients means to go beyond the standard observations and gaining additional spatial information. The field of all three data types, generated by a simple geometric feature, can be forward modeled by a closed analytic expression. While the relation between gravity and gravity gradients is obvious, the gravity gradients can also be linked to the magnetic field as shown by Poisson's Relation [Blakely, 1996]. This mathematical and physical relation will facilitate the statistical interpretation, such as a description of covariances and error estimations.

In contrast to previous implementations, this dissertation combines consistently all observed data (gravity, gravity gradients, magnetic field) into one simultaneous detection solution. A Matched Filter (MF) forms the basis for the detection of the mass anomaly and a statistical analysis interprets the outcome. The MF, which has originally been developed in communication theory, is a promising tool in geophysical

Previous Research	Sensor Technology									
	Gravity	Magnetic	Seismic	Self-Potential	Resistivity	Induced Polarization	Electromagnetic Conductivity	GPR	Radioactivity	Geothermal
[Allen et al., 2008]	●	·	●	·	●	·	●	●	·	●
[Beres et al., 2001]	●	·	·	·	·	·	·	●	·	·
[Butler, 1984]	●	·	·	·	·	·	·	·	·	·
[Chamberlain et al., 2000]	·	·	·	·	·	·	·	●	·	·
[El-Qady et al., 2005]	·	·	·	·	●	·	·	●	·	·
[FHWA, 2005]	●	●	●	·	●	·	●	●	·	·
[Fountain, 1976]	●	·	·	·	●	·	·	●	·	·
[Ghatge and Waldner, 1991]	●	●	●	·	●	·	●	·	·	·
[Gritto, 2005]	·	·	●	·	·	·	·	·	·	·
[Heath, 2007]	●	●	·	·	·	·	·	·	·	·
[Inazaki et al., 2004]	·	·	●	·	·	·	·	●	·	·
[Linford, 1998]	●	●	·	·	●	·	●	·	·	·
[Luke and Chase, 1997]	·	·	●	·	·	·	·	·	·	·
[McCann et al., 1987]	●	●	●	·	●	·	●	·	·	·
[Mochales et al., 2008]	●	●	·	·	·	·	·	●	·	·
[Munk and Sheets, 1997]	●	●	●	●	●	·	●	●	·	·
[Romaides et al., 2001]	●	·	·	·	·	·	·	·	·	·
[Sogade et al., 1999]	·	·	·	·	·	●	·	·	·	·
[Styles et al., 2005]	●	·	·	·	·	·	·	·	·	·
[Vichabian and Morgan, 2002]	·	·	·	●	·	·	·	·	·	·
[Wynne et al., 2009]	·	·	·	·	·	·	·	·	·	●

Table 1.1: Sensor Applications

exploration as it is sensitive to small variations in the SNR of the observations. The major challenge with this technique is that it requires to model the sought signal generated by the void. However, this model also serves as a constraint for the geophysical inverse problem, which otherwise would not have a unique solution.

The structure of this dissertation is such that the introduction in Chapter 1 is followed by the theoretical background in Chapter 2. The basic theory of the observed quantities as well as the mathematical derivation of the MF formula is presented. The central aspect of this research are the MF computations that simulate the detection problem. A detailed overview of the simulation setup and involved parameters is provided in the beginning of Chapter 3. Furthermore, Chapter 3 contains all MF simulations with their corresponding results and interpretations. Some of those simulations are even combined with actual field data. A statistical analysis of the MF simulations is developed and tested in Chapter 4. The document finalizes with a conclusion based on the evaluation of the MF simulations and an outlook for future research in Chapter 5.

Chapter 2: Theoretical Background

2.1 Observation Quantities

The data of interest in this research are the gravity, gravity gradients, and magnetic field data since they are the most fundamental observations in geophysics. It is open to future research to test if a combination of more data types will be reasonable and deliver an improvement to the detection problem. As indicated in Chapter 1, different sensors and combinations of sensors may have advantages depending on the specific application.

2.1.1 Gravity Field

The gravity potential, W, at an arbitrary point $\mathbf{x}$ on or above the surface of the Earth is the summation of the gravitational potential, V, caused by the mass of the Earth and of the centrifugal potential, Φ, caused by the rotation of the Earth (compare [Heiskanen and Moritz, 1967], [Moritz, 1989], or [Torge, 2001]):

$$W(\mathbf{x}) = V(\mathbf{x}) + \Phi(\mathbf{x}). \tag{2.1}$$

The gradients of these potentials describe the accelerations due to the respective fields:

$$\nabla W(\mathbf{x}) = \nabla V(\mathbf{x}) + \nabla \Phi(\mathbf{x}). \tag{2.2}$$

The gradient of the gravity potential is also defined as the gravity vector

$$\mathbf{g}(\mathbf{x}) = \nabla W(\mathbf{x}) = \begin{bmatrix} \partial W/\partial x_1 \\ \partial W/\partial x_2 \\ \partial W/\partial x_3 \end{bmatrix} = \begin{bmatrix} g_1 \\ g_2 \\ g_3 \end{bmatrix}, \tag{2.3}$$

which direction points in the direction of the plumb line (the vertical). Gravity, g, is defined as the norm of the gravity vector, $\mathbf{g}$.

Taking the spatial derivatives of the gravity vector results in the gravity gradient tensor

$$\Gamma(\mathbf{x}) = \nabla \mathbf{g}(\mathbf{x}) = \begin{bmatrix} \partial g_1/\partial x_1 & \partial g_2/\partial x_1 & \partial g_3/\partial x_1 \\ \partial g_1/\partial x_2 & \partial g_2/\partial x_2 & \partial g_3/\partial x_2 \\ \partial g_1/\partial x_3 & \partial g_2/\partial x_3 & \partial g_3/\partial x_3 \end{bmatrix} = \begin{bmatrix} \Gamma_{11} & \Gamma_{12} & \Gamma_{13} \\ \Gamma_{21} & \Gamma_{22} & \Gamma_{23} \\ \Gamma_{31} & \Gamma_{32} & \Gamma_{33} \end{bmatrix}, \tag{2.4}$$

which presents the changes in gravity along the coordinate axes of the defined system.

The gravity potential, W, of the Earth can be approximated by a normal potential, U, which is the gravity potential of a known reference field, such as, for example, the Geodetic Reference System 1980 (GRS80) or the World Geodetic System 1984 (WGS84). The reference field is defined as a rotational ellipsoid representing an equipotential surface of the normal gravity field. U is the sum of the normal gravitational potential and the centrifugal potential. The gradient of U is the normal gravity vector, which magnitude is called normal gravity, γ. The disturbing potential, T, is defined as the remaining difference between the gravity potential and the normal potential, which eliminates the centrifugal part:

$$T(\mathbf{x}) = W(\mathbf{x}) - U(\mathbf{x}). \tag{2.5}$$

Consequently, the gravity disturbance, δg, is the difference between gravity and normal gravity

$$\delta g(\mathbf{x}) = g(\mathbf{x}) - \gamma(\mathbf{x}), \tag{2.6}$$

and the disturbing gradients are the difference between the gravity gradients and the normal gravity gradients.

From this point on, gravity, g, and gravity gradients, Γ, will refer to the disturbances, skipping the δ sign in order to simplify the notation. All MF simulations in Chapter 3 are also based on the disturbing data. However, one has to note that actual static measurements on the ground always refer to the gravity potential while airborne measurements can be processed to yield gradient disturbances.

Only five of the nine gravity gradient tensor components are mutually independent due to following symmetries of the off-diagonal elements:

$$\begin{aligned} \Gamma_{12} &= \Gamma_{21} \\ \Gamma_{13} &= \Gamma_{31} \\ \Gamma_{23} &= \Gamma_{32}, \end{aligned} \tag{2.7}$$

and due to the following condition given by Laplace's Equation:

$$\Gamma_{11} + \Gamma_{22} + \Gamma_{33} = 0. \tag{2.8}$$

In geodetic applications, the unit of gravity is presented in milligal with $1\,\mathsf{mgal} = 10^{-5}\,\mathsf{m/s^2}$ and the unit of the gravity gradient tensor is Eötvös with $1\,\mathsf{E} = 10^{-9}\,\mathsf{1/s^2}$. These units better represent the small magnitudes that are measured in the real world.

2.1.2 Magnetic Field

The magnetic field strength $\mathbf{H}$ induces a magnetic flux. The density of this magnetic flux is given by the magnetic field $\mathbf{B}$. The equation

$$\mathbf{B} = \mu\mathbf{H} \tag{2.9}$$

shows the most general relationship between $\mathbf{B}$ and $\mathbf{H}$ where μ is the absolute permeability of the medium. In case of free space, the magnetic permeability is given by

$$\mu = \mu_0 = 4\pi \cdot 10^{-7} \frac{\mathsf{N}}{\mathsf{A}^2}. \tag{2.10}$$

Inside a medium the absolute permeability is adjusted to $\mu = \mu_0 \mu_m$, which can be inserted in (2.9). This leads to the derivation of a more complete equation for the magnetic field [Parasnis, 1997]:

$$\begin{aligned} \mathbf{B} &= \mu_0 \mu_m \mathbf{H} \\ &= \mu_0 \mathbf{H} + \mu_0 \left(\mu_m - 1\right) \mathbf{H} \\ &= \mu_0 \mathbf{H} + \mu_0 \chi \mathbf{H} \\ &= \mu_0 \left(\mathbf{H} + \mathbf{M}_i\right). \end{aligned} \tag{2.11}$$

The term $(\mu_m - 1)$ is substituted by χ, the susceptibility of the medium (e.g. defined by the type of rocks). The susceptibility, χ, is not necessarily a proportionality constant, in some cases it might even be a tensor. In the case of a local field and where the induced magnetization is only generated by the main magnetic field of the Earth, a proportionality constant can be assumed. From (2.11), it becomes obvious that inside a medium an additional field strength is introduced. This field strength is the induced magnetization, $\mathbf{M}_i = \chi \mathbf{H}$. Some bodies, as for example a bar magnet, contain magnetization, which is not induced by an external field strength. This type of magnetization is called remanent magnetization, $\mathbf{M}_r$, and leads to the extended equation of the total magnetic field:

$$\mathbf{B} = \mu_0 \left(\mathbf{H} + \mathbf{M}_i + \mathbf{M}_r\right). \tag{2.12}$$

Remanent magnetization poses a special case in the real world and will here be set to zero to simplify the simulations.

Similar to the gravity case, where disturbances are derived by subtracting the properties generated by a normal gravity field from the properties of the total gravity field, as in (2.5) and (2.6), the magnetic case as well defines a residual field of perturbation. The perturbation, $\mathbf{F}$, is the difference between the total magnetic field, $\mathbf{B}$, and the main field, $\mathbf{B}_0 = \mu_0 \mathbf{H}$,

$$\mathbf{F} = \mathbf{B} - \mathbf{B}_0 \tag{2.13}$$

where the latter can be estimated by the International Geomagnetic Reference Field (IGRF) model of the specific survey date [IAGA, 2010]. While a magnetometer usually measures the magnitude of the total magnetic field (2.12), the data of interest are the magnitude of the magnetic field anomaly. The anomaly, ΔB, is defined as the difference in magnitudes of the total magnetic field and the main field:

$$\Delta B = \|\mathbf{B}\| - \|\mathbf{B}_0\|. \tag{2.14}$$

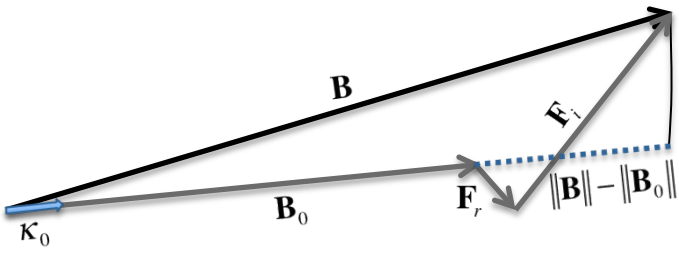

Figure 2.1: Magnetic Field Directions

Under the assumption that the magnitude of the main magnetic field is much larger than the magnitude of the perturbation, $\mathbf{F}$, generated by a magnetic anomaly

$$\|\mathbf{B}_0\| \gg \|\mathbf{F}\|, \tag{2.15}$$

the magnetic field anomaly can be approximated by the perturbation in direction of the main magnetic field

$$\Delta B \approx \kappa_0^T \cdot \mathbf{F} \tag{2.16}$$

where κ_0 is the unit vector in direction of the main magnetic field [Blakely, 1996]. All vector quantities are illustrated in Figure 2.1. In the special case that remanent magnetization does occur, the magnetic field perturbation is the superposition of the induced magnetic field and the remanent magnetic field:

$$\mathbf{F} = \mathbf{F}_i + \mathbf{F}_r = \mu_0 \chi \mathbf{H} + \mu_0 \mathbf{M}_r. \tag{2.17}$$

2.1.3 Poisson's Relation

[Poisson, 1826] points out the similar structure of the gravitational and the magnetic field. Based on that, he relates magnetometry to gravity gradiometry (for other additional details, see [Blakely, 1996]).

The gravitational potential due to a mass source with the density distribution, $\rho(\mathbf{x}') = \rho(x_1', x_2', x_3')$, is given for an arbitrary point, $\mathbf{x} = \begin{bmatrix} x_1 & x_2 & x_3 \end{bmatrix}^T$, above this mass source by

$$V_{\text{grav}}(\mathbf{x}) = G \iiint_v \frac{\rho(\mathbf{x}')}{\sqrt{(x_1 - x_1')^2 + (x_2 - x_2')^2 + (x_3 - x_3')^2}} \mathrm{d}x_1' \mathrm{d}x_2' \mathrm{d}x_3'. \tag{2.18}$$

The scalar magnetic potential due to a source with the magnetization distribution, $\mathbf{M}(\mathbf{x}') = \mathbf{M}(x_1', x_2', x_3')$, is given for an arbitrary point, $\mathbf{x} = \begin{bmatrix} x_1 & x_2 & x_3 \end{bmatrix}^T$, above

this source by

$$V_{\text{mag}}(\mathbf{x}) = \frac{\mu_0}{4\pi} \iiint_v \mathbf{M}^T(\mathbf{x}') \nabla_{(\mathbf{x}')} \left(\frac{1}{\sqrt{(x_1 - x_1')^2 + (x_2 - x_2')^2 + (x_3 - x_3')^2}} \right) \mathrm{d}x_1' \mathrm{d}x_2' \mathrm{d}x_3'. \tag{2.19}$$

Both potentials are described as a volume integral over the inverse distance between the integration points, $\mathbf{x}$, and the source points, $\mathbf{x}'$. As the gravitational potential depends on the scalar density in (2.18) the magnetic potential depends in the same way on the magnetization vector in (2.19). Furthermore, V_{grav} contains the gravitational constant, $G = 6.673 \cdot 10^{-11}\,\mathsf{m}^3/(\mathsf{kg}\,\mathsf{s}^2)$, while V_{mag} also includes the gradient operation $\nabla_{(\mathbf{x}')}$.

Poisson's Relation, derived below, only holds under the two conditions that:

1. The gravitational and the magnetic potential are generated by the same body.
2. The ratio of magnetization to density of this body is constant (2.20). While the magnitude of the magnetization may vary, its direction must be constant.

$$\frac{\|\mathbf{M}(\mathbf{x}')\|}{\rho(\mathbf{x}')} = \text{const} \tag{2.20}$$

If the second condition is not fulfilled, the body source can be subdivided into parts, which each fulfill the second assumption. Superposition will then realize Poisson's relation again.

The derivation is simplified by assuming that the body source has only one constant density

$$\rho(\mathbf{x}') = \rho. \tag{2.21}$$

Similarly, the magnetization throughout the source is assumed constant along the directions of magnetization implemented by a unit direction vector κ:

$$\mathbf{M}(\mathbf{x}') = M\kappa. \tag{2.22}$$

Expressing the distance between observation and source point by

$$\|\mathbf{x} - \mathbf{x}'\| = \sqrt{(x_1 - x_1')^2 + (x_2 - x_2')^2 + (x_3 - x_3')^2} \tag{2.23}$$

and with

$$\nabla_{(\mathbf{x}')} \frac{1}{\|\mathbf{x} - \mathbf{x}'\|} = -\nabla_{(\mathbf{x})} \frac{1}{\|\mathbf{x} - \mathbf{x}'\|} \tag{2.24}$$

the equations for the gravitational and magnetic potential are modified to

$$V_{\text{grav}}(\mathbf{x}) = G\rho \iiint_v \frac{1}{\|\mathbf{x} - \mathbf{x}'\|} \mathrm{d}\mathbf{x}' \tag{2.25}$$

$$V_{\text{mag}}(\mathbf{x}) = -\frac{\mu_0}{4\pi} M \kappa^T \nabla_{(\mathbf{x})} \iiint_v \frac{1}{\|\mathbf{x}-\mathbf{x}'\|} \mathrm{d}\mathbf{x}'. \tag{2.26}$$

Rearranging (2.25) to

$$\iiint_v \frac{1}{\|\mathbf{x}-\mathbf{x}'\|} \mathrm{d}\mathbf{x}' = \frac{V_{\text{grav}}(\mathbf{x})}{G\rho} \tag{2.27}$$

and inserting (2.27) into (2.26) leads to the formula of Poisson's Relation

$$V_{\text{mag}}(\mathbf{x}) = -\frac{\mu_0}{4\pi} \frac{M}{G\rho} \kappa^T \nabla_{(\mathbf{x})} V_{\text{grav}}(\mathbf{x}), \tag{2.28}$$

which now phrases the magnetic potential in terms of the gravitational potential [Blakely, 1996]. The right side of it is also called the pseudo-magnetic potential.

Considering that the gradient of the gravitational potential is the gravitational acceleration vector

$$\mathbf{g}(\mathbf{x}) = \nabla_{(\mathbf{x})} V_{\text{grav}}(\mathbf{x}) \tag{2.29}$$

equation (2.28) is rewritten to

$$V_{\text{mag}}(\mathbf{x}) = -\frac{\mu_0}{4\pi} \frac{M}{G\rho} \mathbf{g}^T(\mathbf{x}) \kappa. \tag{2.30}$$

Poisson's Relation can be developed one step further by taking the gradient on both sides of (2.30), leading to

$$\nabla_{(\mathbf{x})} V_{\text{mag}}(\mathbf{x}) = -\frac{\mu_0}{4\pi} \frac{M}{G\rho} \nabla_{(\mathbf{x})} \mathbf{g}^T(\mathbf{x}) \kappa. \tag{2.31}$$

The gradient of $\mathbf{g}(\mathbf{x})$ is the gravitational gradient tensor

$$\Gamma(\mathbf{x}) = \nabla_{(\mathbf{x})} \mathbf{g}^T(\mathbf{x}) \tag{2.32}$$

and the negative gradient of the magnetic potential is defined as the magnetic field vector

$$\mathbf{B}(\mathbf{x}) = -\nabla_{(\mathbf{x})} V_{\text{mag}}(\mathbf{x}). \tag{2.33}$$

In order to derive the magnitude of the total magnetic field in the direction of magnetization, the magnetic field is multiplied by the unit vector pointing in the direction of magnetization:

$$B(\mathbf{x}) = \kappa^T \mathbf{B}(\mathbf{x}). \tag{2.34}$$

Substituting (2.32) to (2.34) in (2.31), results in the final Poisson's Relation that expresses the magnetic field in terms of the gravitational gradient tensor:

$$B(\mathbf{x}) = \frac{\mu_0}{4\pi} \frac{M}{G\rho} \kappa_0^T \Gamma(\mathbf{x}) \kappa_0. \tag{2.35}$$

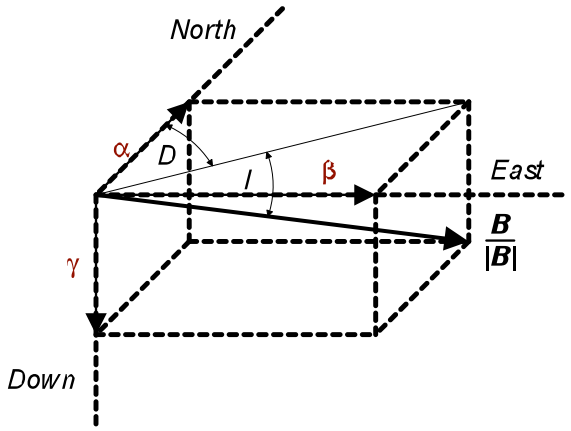

Figure 2.2: Inclination and Declination

Here, the direction of magnetization is approximated by $\kappa \approx \kappa_0$, which is the unit vector in direction of the main magnetic field, Figure 2.1. This is a justified approximation in cases where the main magnetic field is much greater than the disturbing magnetic field (2.15). If the special case of remanent magnetization is neglected and the magnetization of an anomaly is simply $M = \chi H$, the magnetic field in (2.35) stands for the magnetic field anomaly ΔB as described in (2.16). However, in the following the magnetic field anomaly will simply be noted as B. The tensor Γ in (2.35) consists of the gravitational gradients since Poisson's Relation is derived from the gravitational potential, which does not contain the centrifugal potential. As defined in Section 2.1.1, Γ, will from now on refer to the disturbing gravity gradients. This substitution is legitimate since the disturbing gravity gradients also do not contain a centrifugal part. As mentioned above, the disturbing gravity gradients will simply be called gravity gradients in the following. The right side of (2.35) is also labelled pseudo-magnetic field anomaly. All parameters require units given in the SI system (Système international d'unités).

The components of the unit vector κ_0 consist of the direction cosines

$$\begin{aligned} \alpha &= \cos(-I)\cos(-D) \\ \beta &= \cos(-I)\sin(-D) \\ \gamma &= \sin(-I)\,. \end{aligned} \tag{2.36}$$

I and D are thereby the inclination and the declination of the Earth's gravity field, respectively. Figure 2.2 presents those angles within the assumed North-East-Down (NED) coordinate system of the gravity field. The inclination is the vertical angle to the magnetic field from the horizontal plane. The declination is the horizontal angle to the magnetic field from North.

The negative signs in (2.36) account for the fact that I and D are commonly defined in the NED system while this dissertation refers all values to the North-West-Up (NWU) system. If all gravity gradients are known, the magnetic field can be computed considering Poisson's relation and the direction $\kappa_0 = \begin{bmatrix} \alpha & \beta & \gamma \end{bmatrix}^T$. The components of the magnetic field vector are given below:

$$B_1 = \frac{\mu_0}{4\pi} \frac{\chi H}{G\rho} \left(\alpha\Gamma_{11} + \beta\Gamma_{12} + \gamma\Gamma_{13}\right), \tag{2.37}$$

$$B_2 = \frac{\mu_0}{4\pi} \frac{\chi H}{G\rho} \left(\alpha\Gamma_{21} + \beta\Gamma_{22} + \gamma\Gamma_{23}\right), \tag{2.38}$$

$$B_3 = \frac{\mu_0}{4\pi} \frac{\chi H}{G\rho} \left(\alpha\Gamma_{31} + \beta\Gamma_{32} + \gamma\Gamma_{33}\right). \tag{2.39}$$

Those components are given with respect to the coordinate axes of the gravity field. It is common, however, to measure the total magnetic field in direction of the magnetization as shown in the next computation step

$$B = \alpha B_1 + \beta B_2 + \gamma B_3. \tag{2.40}$$

While Poisson's Relation is a valid theory, the question arises how practical it is in a real world example. Remanent magnetization, for example, is very difficult to handle as it can alter the direction of magnetization significantly. The key aspect is the homogeneity of the survey area. A comparison between magnetic and pseudo-magnetic data of various areas in the USA shows evidence that Poisson's Relation is hardly applicable on a regional scale [Jekeli et al., 2011]. While, there, the compared maps prove some correlation, highly magnetic features are not presented in the pseudo-magnetic maps and, on the other hand, strong gravity signals caused by a change in topography are not reflected in the magnetic maps. This lack in correlation is due to the fact that the conditions of Poisson's Relation are violated, namely the magnetization to density ratio (2.20) is not constant throughout the investigated area. However, preliminary gradient measurements based on a relative gravity gravimeter and magnetic field measurements based on a proton-precession magnetometer in the same area show clearly a correlation on a local scale [Abt et al., 2011]. In conclusion, the above experiments show that Poisson's Relation strongly depends on the mass density and magnetization and is only reasonable in a local area at a time. Since this research concentrates only on small observation grids ($100\,\mathsf{m} \times 100\,\mathsf{m}$), Poisson's Relation is confidently applied to derive statistical functions such as the covariances between the gravity and the magnetic field. Furthermore, closed formulas for gravity gradient signals generated by a specific source, can easily be transformed into closed formulas for magnetic field signals as presented in [Telford et al., 1990]. Extra caution has to be paid if the survey area is located in an urban environment as other artificial sources such as wires are likely to interfere with the magnetic measurements and strongly overpower the signal of the sought magnetic anomaly.

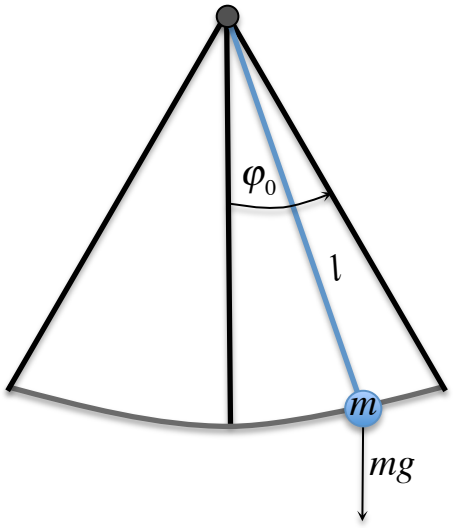

Figure 2.3: Simple Pendulum

2.2 Measurement Instruments

Studies of interest in Geodesy occur at all scales spanning from close-range, local, regional, up to global applications. All data collecting sensors need, therefore, be adjusted to the corresponding scale. Typically, sensors are divided into ground, airborne, and satellite instruments. Since, the MF application of this research applies to a local area, mainly the ground instruments are of interest and will be presented in the following. This section briefly introduces the basic concepts of the gravimeter, gravity gradiometer, and magnetometer. Detailed instrument descriptions and mathematical derivations of the observation equations are provided in [Torge, 1989] for gravity related measurements and in [Burger et al., 2006] and [Parasnis, 1997] for magnetic related measurements.

2.2.1 Gravimeter

The early gravity measurements starting with Galileo Galilei are carried out with a pendulum device (Figure 2.3) [Torge, 2001]. In an ideal mathematical case, a point mass, m, is suspended from a massless string of a constant length, l, and freely swings in the vertical plane with an oscillation period, T, at a small amplitude, φ_0. Under those circumstances the oscillation period is approximately expressed by

$$T = 2\pi\sqrt{\frac{l}{g}} \tag{2.41}$$

as derived, for example, by [Fishbane et al., 2005, p.379] or [Halliday et al., 2001, p.356]. Knowing the length of the string and measuring the oscillation period can solve for gravity

$$g = \frac{4\pi^2 l}{T^2}. \tag{2.42}$$

Any physical realization of the pendulum device leads to the problem to accurately determine T and l, which are not stable quantities. Taking the difference between two gravity readings of the same pendulum at two different observation points will reduce some errors such as those caused by the unstable effect of the length, l. However, even the most elaborate pendulum devices are still limited to an accuracy of 0.1 mgal [Parasnis, 1997].

Nowadays, a different approach results in more compact, less time-intensive, and more accurate measurement devices. The instruments are thereby divided into absolute and relative gravimeters. Absolute gravimeters, as for example the FG5 [Carter et al., 1994], are based on Galileo's law of falling bodies [Fishbane et al., 2005, p.45]

$$z = \frac{1}{2} g t^2. \tag{2.43}$$

The concept of a free falling mass avoids the additional force caused by the tension in the string of the pendulum device. z is the local vertical distance the body covers over a time period, t. Measuring both quantities solves for gravity under the assumption that it is constant over distance. High accuracies are achieved by measuring the time with a small atomic clock and by measuring the distance based on laser interferometry. Due to the difficulty to accurately determine the starting point of the instrument, z_0, at time, t_0, and due to small seismic accelerations, $\dot{z}_0$, (2.43) is modified to

$$z(t) = z_0 + \dot{z}_0 (t - t_0) + \frac{1}{2} g (t - t_0)^2 . \tag{2.44}$$

This equation of three unknowns requires at least three measurements in order to be solvable. An actual measurement at one station is based on several hundreds of mass drops to average out most of the random errors. Absolute gravity measurements are expensive and time-intensive and are, therefore, only used for special tasks such as establishing a gravity network. The standard gravity applications mostly require just a relative gravity measurement that can be acquired by the less expensive and more practical relative gravimeter. Many systematic errors are thereby eliminated automatically due to the differencing but the overall accuracy (0.01 mgal [Torge, 2001]) is less than in case of the absolute gravimeter (0.002 mgal [Niebauer et al., 1995]).

Relative gravimeters are designed by the concept of a proof mass on an elastic spring. A change of gravity between two stations is observed by the difference in the extension of the spring. In order to increase the sensitivity of the spring the concept of the zero-length spring is adopted. A zero-length spring is pre-stressed in such a way that its extension equals its actual physical length, i.e. if no mass were

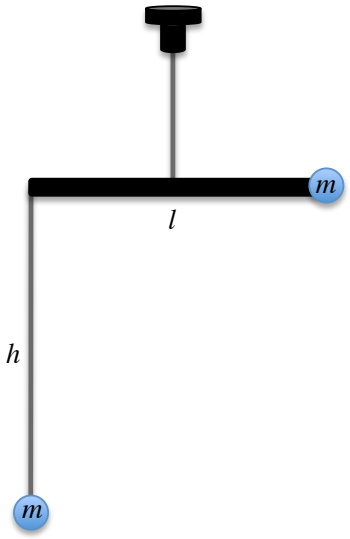

Figure 2.4: Torsion Balance

attached it would theoretically collapse to zero length. A more advanced realization of this basic concept is to attach the mass to a rotating lever, which is connected to the spring. The torque applied to the spring in order to generate an equilibrium of torques can be related to the torque generated by gravity. Since the elasticity of the spring is the most critical feature of the relative gravimeter, the instrument is internally kept at a constant temperature, under constant air-pressure, and shielded from outside magnetic fields. Modern relative gravimeters such as, for example, the CG-5 Scintrex Autograv System [SCINTREXLimited, 1997], already perform an Earth tide reduction (based on input coordinates) as well as a drift control (based on instrument calibration) in their observations. However, some drift and tares of the spring are unavoidable, which cause changes in the zero reading of the instrument. In order to reduce the resulting errors, a base station is repeatedly observed throughout a measurement campaign, which allows to model the residual drifts. A further error source in a practical application is the leveling of the instrument, which has a standard deviation of 0.002 mgal [Torge, 1989]. Overall, the measurements take a few minutes per station.

2.2.2 Gradiometer

The first instrument to measure all independent components of the gravity gradient tensor (except Γ_{33}) is the torsion balance developed by Loránd Eötvös around 1900. The instrument was developed from Coulomb's torsion balance [Fishbane et al., 2005, p.618] and is schematically drawn in Figure 2.4. The torsion balance consists of two

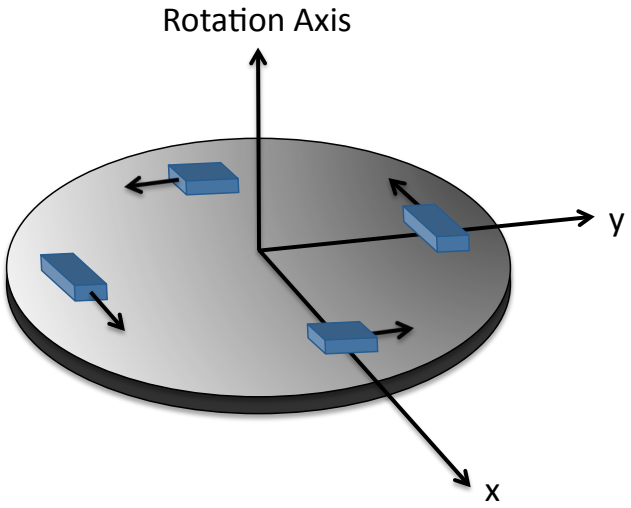

Figure 2.5: Airborne Gradiometer Disk

equal masses, m, connected by a rigid horizontal beam of length, l. One mass is lowered from the beam by the height difference, h. The horizontal components of the gravity vector generate a torque acting on the two masses and cause a twist in the torque wire, which is placed at the center of the instrument. Rotating the beam around the vertical axis leads to an equilibrium of torques, which is described by a combination of the gravity gradient components, $\Gamma_{22}-\Gamma_{11}$, Γ_{12}, Γ_{13}, Γ_{23} [Torge, 1989]. In order to estimate those components at least five observations at various azimuths are necessary. The observations are very laborious and time intensive, especially in uneven terrain. This technique is, therefore, rather outdated.

A more common approach based on the somewhat different concept of differential accelerometry is used in systems that are currently being deployed on aircraft and ships. Airborne gradiometry, in particular, is capable to cover a regional area in a short time span with a point resolution between $50\,\mathsf{m} - 2000\,\mathsf{m}$ and a standard deviation of $5\,\mathsf{E}$ [Murphy, 2004]. Bell Aerospace developed, for example, a rotating gradiometer system that is now operated by Bell Geospace, Inc. This Full Tensor Gravity Gradiometry system (FTG), contains two pairs of accelerometers mounted orthogonally on a rotating disk [Jekeli, 1988] as illustrated in Figure 2.5. The difference in the reading of one accelerometer pair is the gravity gradient along their particular axis. The rotation of the disk modulates the undesired difference in scale factor of the accelerometer pair and allows to adjust for this error. Furthermore, the rotation modulates the gradient observation to a higher frequency and allows to eliminate the low frequency noise (red noise) caused by the individual accelerometer. Three of those disks containing each two accelerometer pairs are mounted together in

such an arrangement that the five independent gravity gradients can be determined by linearly combining the accelerometer differences of the individual disks [Jekeli, 1988]. The introduction of two more accelerometer pairs on each disk will lead to redundant measurements that improve the precision. Furthermore, if five rather than three of those disks are appropriately mounted together, it will be possible to measure each of the nine tensor components independently [Jekeli, 2006]. Independent measurements are important when postprocessing the data set. An identified anomaly in one gravity gradient component is expected to have a corresponding response in the other components. If this is not the case, the signal of the assumed anomaly is declared as noise and removed from the data set. In contrast to airborne gravity measurements, gravity gradiometry automatically eliminates the first order acceleration of the aircraft by taking the differences of the accelerometers. The same advantage also applies if the gradiometer is alternatively mounted on a vessel for marine research.

The first full-tensor gravity gradiometer orbiting the Earth has been launched with the Gravity field and steady-state Ocean Circulation Explorer (GOCE) satellite in 2009 [Rummel et al., 2000]. This might inspire researchers to a further improvement of ground gravity gradiometry as well and to develop a more accurate and feasible alternative to the torsion balance.

2.2.3 Magnetometer

The two types of magnetometers that are widely in use are the proton-precession magnetometer and the flux-gate magnetometer. Both instruments measure the total magnetic field as described in Section 2.1.2. The proton-precession magnetometer was developed by Varian Associates in 1955. It consists of a cylindrical container filled with a hydrogen-rich fluid and is surrounded by a coil. The flow of a direct current through that coil generates a magnetic field with field lines parallel to the axes of the coil. A few hydrogen protons in the liquid align themselves to the resultant of the generated and the magnetic field of the Earth. As soon as the direct current is interrupted, the protons are not instantaneously reverted to their original direction but will instead precess under the torque caused by the total magnetic field, $\mathbf{B}$. This precession causes a small alternating voltage in the coil. The precession frequency, f_{precess}, of this voltage is the measured quantity as it is proportional to the magnitude of the total magnetic field

$$B = \frac{2\pi f_{\text{precess}}}{\gamma_{\text{gyro}}}. \tag{2.45}$$

The voltage decays exponentially as the protons reach their original orientation. The proportionality constant in (2.45) is called the gyromagnetic ratio of a proton, $\gamma_{\text{gyro}} = 2.667520 \cdot 10^8 \, (\mathsf{T}\,\mathsf{s})^{-1}$. The major advantage of the proton-precession magnetometer is that it does not require leveling or stabilization of the instrument. This ensures a very rapid and easy measurement procedure for collecting ground as well as airborne

data. A disadvantage is that it, unlike the flux-gate magnetometer, only determines the quantity of the total magnetic field but not its direction.

The flux-gate magnetometer was invented by Victor Vacquier in the 1930s. Ten years later, it was modified to make it also applicable for airborne projects. A typical flux-gate magnetometer consists of two parallel metal bars with high permeability. Each bar is wrapped by a primary coil. The windings of these coils are, however, reversed so that the flow of an alternating current induces two magnetic fields that are antiparallel in orientation. A set of two secondary coils are wrapped around the primary coils. Under the assumption of no external magnetic field, the voltage in the secondary coils are zero as both induced magnetic fields cancel each other out. If the instrument is aligned along a component of an external field though, one bar will damp the external field while the other will reinforce it. Due to this difference a voltage is induced in the secondary coils. This induced voltage is proportional to the corresponding magnetic filed component of the external field. Depending on the orientation of the instrument, the magnetic field is measured in different directions. This is an advantage but at the same time makes the placing of the instrument in an actual survey more challenging.

In general, magnetic measurements are performed more rapidly than gravity measurements but they are also more vulnerable to disturbing sources from the outside. The operator can already cause magnetic noise with the zipper of his jacket or the metal rings that hold his shoelaces.

2.3 Matched Filter

The detection of the mass anomaly is here solved by applying a Matched Filter (MF). The MF is in general used as a technique to identify the signal of a specific source within a noisy background field. The sought signal generated by the source is thereby "matched" with the observed data in the area of interest. This requires that the signal generated by the source is known, which is often the case for man-made mass anomalies. Geologic features, on the other hand, can most likely be approximated by an object of simple known structure as, for example, a prism or a cylinder. If the shape of the geologic feature is more advanced, such as a fault, the combination of several prisms is suggested. Furthermore, the MF requires that the noise of the background field can be statistically described by a covariance function as part of the MF input. Since the MF searches for the maximum Signal-to-Noise Ratio (SNR), it is able to detect a signal hidden within the noise where other techniques might fail. The MF is simple to implement and does not require too much computational effort.

2.3.1 History

Due to the general character of the MF, its applications range over a huge variety of different tasks. Some common applications exist in communication, medicine, electrical engineering and astrophysics. Specific MF examples, that are closer related to geosciences, are the processing of stellar images in order to detect, recover, and track near-Earth asteroids [Gural et al., 2005] as well as the processing of InSAR (Interferometric Synthetic Aperture Radar) measurements in order to study the crustal deformation of the Earth [Zebker, 2000]. Matched filtering of infrared images with a three-dimensional object model is used by [Lundberg and Gu, 1999] to detect and locate land mines in the shallow subsurface. The infrared images account for the fact that land mines produce a thermal contrast to the soil over time. A further MF example is given by [Dobbs et al., 2005], who develop a low-cost fiber-based LIDAR (Light Detection and Ranging) method for atmospheric exploration of the Earth.

Contributions of the MF to the studies of the Earth's gravity field are rare and this suggests, therefore, a new area to explore. Based on the available literature, the MF is slightly more common for magnetic applications. The simultaneous combination of magnetic field data, gravity, and gravity gradients in a MF process still needs to be further investigated. One of the early approaches based on an MF and magnetic data is provided by [Naudy, 1971]. He developed a method that locates a magnetic anomaly source such as a bottomless prism (dike) or a thin layer and determines their depths. His method is based on the MF although he does not name it so. The aeromagnetic data of an observed profile are compared to the theoretically generated profile. The profile signal is separated into a symmetric and an anti-symmetric component. The MF is applied twice. First to the symmetric part and then to the anti-symmetric part after it has been made symmetric by reducing it to the pole, i.e. modifying the magnetic data as if the inclination, I, (2.36) were $90\,^{\circ}$. A further MF example provided by [Keating, 1995] is based on magnetics and the detection of kimberlites, a major source for diamonds. Kimberlites are best modeled by a finite vertical cylinder. This model and the actual magnetic data are compared by a pattern recognition technique that involves a moving window. [Keating, 1995] does not provide any detailed formulas but his ideas sound similar to matched filtering. The drawbacks are that the diameters and depths of the kimberlites must be estimated a priori. An application that is based on the gravity field of the Earth is [White et al., 1983] where the MF is used to locate seamounts from satellite radar altimetry. Airborne gravity gradients are applied in [Dumrongchai, 2007]'s project. He uses the MF as a tool to detect man-made mass anomalies in the shallow subsurface. The present dissertation can be seen as a continuation and extension of this project applied to local ground data.

2.3.2 Mathematical Derivation

The MF is a convolution of the input vector, z, which contains the observations, and the filter function, h, leading to the equation

$$y\left(x_r\right) = \sum_j h^T\left(x_r - x_j\right) z\left(x_j\right) = \sum_j h^T\left(x_j\right) z\left(x_r - x_j\right) \tag{2.46}$$

where y is the scalar filter output as also described by [Dumrongchai, 2007] and [Jekeli and Abt, 2010]. All values are here discrete and depend on their spatial coordinate x. It is assumed that the observed points have a constant interval and lie on a horizontal plane. The vertical coordinate is, therefore, neglected. The horizontal coordinate can either describe a profile, $x_j \mathrel{\widehat{=}} x_{j_1}$, or a grid of observations, $x_j \mathrel{\widehat{=}} x_{j_1,j_2} = (x_{j_1}, x_{j_2})$ with $j_1 = j_2 = 1, 2, \ldots$. In case of a survey grid, each summation in (2.46) and the following equations is replaced by a double sum over both horizontal coordinates. The observation vector, z, is defined by the summation of the sought signal, s, and of the noise vector, n, and can be written as

$$z\left(x_j\right) = s\left(x_j - x_m\right) + n\left(x_j\right). \tag{2.47}$$

While the sought signal is generated by the source at the unknown location, x_m, the noise vector is mainly generated by the correlated gravity background field as well as by some random instrument errors. Hence, the MF output can be split into a sought signal and a noise part after inserting (2.47) into (2.46):

$$y\left(x_r\right) = \sum_j h^T\left(x_j\right) s\left(x_r - x_j - x_m\right) + \sum_j h^T\left(x_j\right) n\left(x_r - x_j\right). \tag{2.48}$$

The Signal-to-Noise Ratio (SNR) of the MF is here defined by the squared norms of the sought signal and noise part:

$$\mathrm{SNR}\left(x_r\right) = \frac{\left(\sum_j h^T\left(x_j\right) s\left(x_r - x_j - x_m\right)\right)^2}{\varepsilon\left(\left(\sum_j h^T\left(x_j\right) n\left(x_r - x_j\right)\right)^2\right)}. \tag{2.49}$$

ε stands for the statistical expectation as the actual values of the noise are unknown. The input of the MF requires that the noise is statistical described by a covariance matrix of the following expression:

$$\mathrm{cov}\big(n\left(x_r - x_j\right), n\left(x_r - x_k\right)\big) = \varepsilon\big(n\left(x_r - x_j\right) n\left(x_r - x_k\right)\big). \tag{2.50}$$

The noise is assumed to be a Gaussian stationary process with a zero-mean. The covariance function that describes this noise, therefore, depends only on the horizontal

coordinate differences. The notation of this covariance function is defined as:

$$\begin{aligned}\phi\big((x_r - x_j) - (x_r - x_k)\big) &= \phi\big(-x_j - (-x_k)\big) \\ &\widehat{=} \phi\left(-x_j, -x_k\right).\end{aligned} \tag{2.51}$$

Here, the coordinate difference between two points is defined as the coordinates of the first observation point minus the coordinates of the second observation point. If the values of the background field were uncorrelated ϕ would be a diagonal matrix. However, it is assumed that the background field is correlated and that ϕ is a full matrix.

After the derivation of the noise covariance matrix , it is now possible to determine the filter function, h. The noise part can be described by the denominator of (2.49)

$$P\left(x_r\right) = \sum_j \sum_k h^T\left(x_j\right) \phi\left(-x_j, -x_k\right) h\left(x_k\right). \tag{2.52}$$

A more compact notation of the summations is introduced in order to facilitate the derivation of the filter function. For that reason all $h\left(x_j\right)$ are summarized in one vector, $\mathbf{h}$, and all covariance submatrices, ϕ, are summarized in one global covariance matrix, Φ_-, where the minus sign in the index is a reminder of the negative input coordinates (2.51). In the same way all signal values of the summation in (2.48) are summarized in one vector $s_{r,m} \widehat{=} s\left(x_r - x_j - x_m\right)$. Considering this vector notation,

$$P\left(x_r\right) = \mathbf{h}^T \Phi_- \mathbf{h} \tag{2.53}$$

presents the noise and

$$Q\left(x_r\right) = \left(\mathbf{h}^T \mathbf{s}_{r,m}\right)^2 \tag{2.54}$$

presents the signal part (numerator of (2.49)) of the MF, respectively.

The aim is to define a filter function that maximizes the SNR at the location of the sought signal, $x_r = x_m$. In that specific case the signal vector, $s_{r,m}$, is given by

$$\mathbf{s}_{m,m} = \sum_j s\left(-x_j\right) \widehat{=} \mathbf{s}_-. \tag{2.55}$$

The SNR is independent of the scale of the filter function (2.49) and P is independent of the x_r-coordinate. In conclusion, the denominator of (2.49) can be represented by a positive constant, const^2. A cost function with Lagrange multiplier [Bronshteĭn, 2007, p.403] is established,

$$\Lambda = \left(\mathbf{h}^T \mathbf{s}_-\right)^2 + \lambda^2 \left(\text{const}^2 - \mathbf{h}^T \Phi_- \mathbf{h}\right), \tag{2.56}$$

that maximizes Q (2.54) under the constraint that P (2.52) equals const^2. Taking the derivatives of Λ with respect to the two unknowns lead to the two equations:

$$\frac{\partial \Lambda}{\partial \mathbf{h}} = 2\mathbf{h}^T \mathbf{s}_- \mathbf{s}_-^T - \lambda^2 \left(\mathbf{h}^T \Phi_- + \mathbf{h}^T \Phi_-^T\right) \tag{2.57}$$

and

$$\frac{\partial \Lambda}{\partial (\lambda^2)} = \text{const}^2 - \mathbf{h}^T \Phi_- \mathbf{h}. \tag{2.58}$$

The next computational step is achieved by setting the derivatives to zero and by assuming that the covariance matrix is symmetric.

$$\lambda^2 \mathbf{h}^T \Phi_- = \mathbf{h}^T \mathbf{s}_- \mathbf{s}_-^T \tag{2.59}$$

$$\mathbf{h}^T \Phi_- \mathbf{h} = \text{const}^2 \tag{2.60}$$

Multiplying (2.59) by $\mathbf{h}$ from the right on both sides and inserting (2.60) solves for the maximum SNR:

$$\lambda^2 = \frac{\mathbf{h}^T \mathbf{s}_- \mathbf{s}_-^T \mathbf{h}}{\text{const}^2}. \tag{2.61}$$

Taking the transpose of (2.59) and then multiplying by Φ_-^{-1} from the left on both sides of the equation computes the next line

$$\Phi_-^{-1} \mathbf{s}_- \mathbf{s}_-^T \mathbf{h} = \lambda^2 \mathbf{h}. \tag{2.62}$$

Φ_- is always invertible. $\Phi_-^{-1} \mathbf{s}_- \mathbf{s}_-^T$ is a matrix of rank 1 and has, therefore, only one non-zero eigenvalue. The corresponding eigenvector is

$$\mathbf{h} = \frac{\text{const}}{\sqrt{\mathbf{s}_-^T \Phi_-^{-1} \mathbf{s}_-}} \Phi_-^{-1} \mathbf{s}_- \tag{2.63}$$

for the eigenvalue

$$\lambda^2 = \mathbf{s}_-^T \Phi_-^{-1} \mathbf{s}_- \tag{2.64}$$

based on (2.61) and (2.62). This eigenvalue also equals the trace of the matrix,$\Phi_-^{-1} \mathbf{s}_- \mathbf{s}_-^T$.

Since the scale of the filter has no influence on the SNR of the MF, as stated above, const^2 is simply set to 1. This results in the filter function

$$\mathbf{h} = \frac{1}{\lambda} \Phi_-^{-1} \mathbf{s}_- \tag{2.65}$$

Turning back to the original notation including summations, the filter function is expressed by

$$h(x_j) = \frac{1}{\lambda} \sum_k \phi^{-1}(-x_j, -x_k)\, \bar{s}(-x_k). \tag{2.66}$$

While the parameter s in (2.47) stands for the actual sought signal generated by the source, the parameter $\bar{s}$ in (2.66) denotes the modeled sought signal, which ideally equals s but might differ in practice. The superscript '-1' indicates that the matrix element, ϕ, is taken from the inverted covariance matrix, Φ, and does not stand for the inverse of the individual matrix element.

The filter function is scaled by the reciprocal of λ derived from the eigenvalue

$$\lambda^2 = \sum_j \sum_k \bar{s}^T(-x_j)\,\phi^{-1}(-x_j, -x_k)\,\bar{s}(-x_k), \tag{2.67}$$

which is also the maximum of the SNR at the location $x_r = x_m$:

$$\max_r\big(\mathrm{SNR}(x_r)\big) = \lambda^2. \tag{2.68}$$

The final equation for the MF output is given by

$$y(x_r) = \frac{1}{\lambda} \sum_j \sum_k \bar{s}^T(-x_k)\,\phi^{-1}(-x_j, -x_k)\,z(x_r - x_j). \tag{2.69}$$

The filter function, h, is determined from the covariances, ϕ, and the sought signal, s. The matrix ϕ contains the covariances of the background field noise at the corresponding observation points.

Due to the assumed zero-mean of the noise, the statistical mean of the filter output becomes

$$\mu_r = \varepsilon\big(y(x_r)\big) = \frac{1}{\lambda} \sum_j \sum_k \bar{s}^T(-x_k)\,\phi^{-1}(-x_j, -x_k)\,s(x_r - x_j - x_m) \tag{2.70}$$

and the variance of the filter output is

$$\mathrm{var}\big(y(x_r)\big) = 1 \tag{2.71}$$

as derived in [Jekeli and Abt, 2010]. Setting $x_r = x_m$ in (2.70) and inserting (2.67) leads to the maximum filter output

$$\max_r\Big(\varepsilon\big(y(x_r)\big)\Big) = \varepsilon\big(y(x_m)\big) = \lambda. \tag{2.72}$$

This validates the initial goal to design a filter function that locates the sought signal by the maximum filter output.

Due to the subtraction of coordinates in the implementation of the MF (2.69) and through the above derivation, some signal and observation values lie outside the domain of the finite survey area. This problem is solved by periodically repeating the signal and observation of the entire survey area with a period equal to the initially defined domain. An alternative solution would be zero-padding along the borders of the defined survey area. However, since the noise in a real application is unlikely to be zero, periodicity is a more realistic generalization. In addition, periodicity is a requirement if the MF computations are carried out in the frequency domain using the discrete Fourier transform. Since the scope of this research is limited to a local area with a manageable amount of survey points, a transfer into the frequency domain is not necessary at this point.

Chapter 3: Simulations

3.1 Setup

The ability of the Matched Filter (MF) to detect a local mass anomaly in the shallow subsurface is first tested by setting up a simulation that describes the typical environment of a future application. The area of interest is designed to be level and of $100\,\mathsf{m}^2$ size. The data points of that area lie on a grid with a constant point interval of $1\,\mathsf{m}$ along both directions. In order to simplify the computations it is assumed that the observations of different sensors (gravity, gravity gradients, magnetic field) refer to exactly the same observation points and one observation point lies exactly above the center of the sought anomaly. Furthermore, no remanent magnetization is taken into account.

3.1.1 Sought Signal

The sought signal, s, is generated by a three-dimensional prism, which is defined by its center coordinates $\left[\begin{array}{ccc} x_1{}' & x_2{}' & x_3{}' \end{array}\right]^T$ and its width, a, length, b, and height, c, as drawn in Figure 3.1. Throughout this dissertation, a local North-West-Up (NWU)

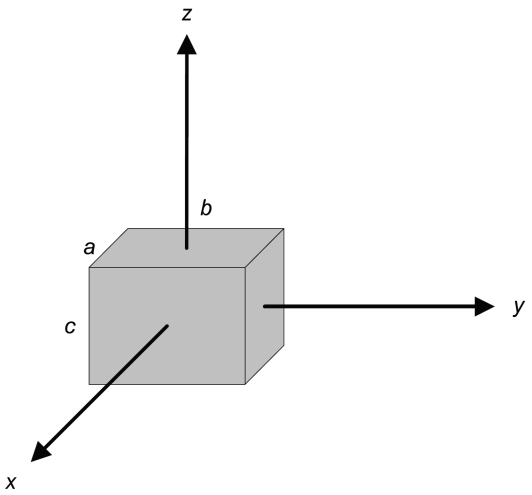

Figure 3.1: 3d Prism simulates Mass Anomaly

coordinate system is utilized. As derived in [Jekeli, 2003a], the gravity gradient components above such a prism can be computed by closed formulas:

$$
\begin{aligned}
\Gamma_{11} &= \arctan \frac{(x_2 - {x_2}')\,(x_3 - {x_3}')}{(x_1 - {x_1}')\,r}\Big|_{x_1=-\frac{a}{2}}^{\frac{a}{2}}\Big|_{x_2=-\frac{b}{2}}^{\frac{b}{2}}\Big|_{x_3=-\frac{c}{2}}^{\frac{c}{2}} \\
\Gamma_{22} &= \arctan \frac{(x_1 - {x_1}')\,(x_3 - {x_3}')}{(x_2 - {x_2}')\,r}\Big|_{x_1=-\frac{a}{2}}^{\frac{a}{2}}\Big|_{x_2=-\frac{b}{2}}^{\frac{b}{2}}\Big|_{x_3=-\frac{c}{2}}^{\frac{c}{2}} \\
\Gamma_{33} &= \arctan \frac{(x_1 - {x_1}')\,(x_2 - {x_2}')}{(x_3 - {x_3}')\,r}\Big|_{x_1=-\frac{a}{2}}^{\frac{a}{2}}\Big|_{x_2=-\frac{b}{2}}^{\frac{b}{2}}\Big|_{x_3=-\frac{c}{2}}^{\frac{c}{2}} \\
\Gamma_{12} &= -\ln\left(x_3 - {x_3}' + r\right)\Big|_{x_1=-\frac{a}{2}}^{\frac{a}{2}}\Big|_{x_2=-\frac{b}{2}}^{\frac{b}{2}}\Big|_{x_3=-\frac{c}{2}}^{\frac{c}{2}} \\
\Gamma_{13} &= -\ln\left(x_2 - {x_2}' + r\right)\Big|_{x_1=-\frac{a}{2}}^{\frac{a}{2}}\Big|_{x_2=-\frac{b}{2}}^{\frac{b}{2}}\Big|_{x_3=-\frac{c}{2}}^{\frac{c}{2}} \\
\Gamma_{23} &= -\ln\left(x_1 - {x_1}' + r\right)\Big|_{x_1=-\frac{a}{2}}^{\frac{a}{2}}\Big|_{x_2=-\frac{b}{2}}^{\frac{b}{2}}\Big|_{x_3=-\frac{c}{2}}^{\frac{c}{2}}\,.
\end{aligned}
\tag{3.1}
$$

Those closed formulas correspond to the magnetic gradients formulas presented in [Sharma, 1997, Appendix C]. However, the latter are based on coordinate axes pointing North-East-Down (NED) while (3.1) is based on the NWU axes system. Depending on the type of gradiometer not all of the above gradient components are necessarily measured. The corresponding gravity value is

$$\begin{aligned} g_3 = &- (x_3 - {x_3}') \arctan\left(\frac{(x_1 - {x_1}')\,(x_2 - {x_2}')}{(x_3 - {x_3}')\,r}\right) \\ &- (x_1 - {x_1}') \ln(x_2 - {x_2}' + r) \\ &- (x_2 - {x_2}') \ln(x_1 - {x_1}' + r)\big|_{x_1=-\frac{a}{2}}^{\frac{a}{2}}\Big|_{x_2=-\frac{b}{2}}^{\frac{b}{2}}\Big|_{x_3=-\frac{c}{2}}^{\frac{c}{2}} \end{aligned} \tag{3.2}$$

in the NWU coordinate system. It is conventional to define gravity as pointing positively downward. Since the vertical coordinate axis is here pointing upwards the following relation holds

$$g_3 = -\frac{\partial T}{\partial x_3} \tag{3.3}$$

with T being the disturbing potential (Section 2.1.1).

In the current example, the following parameters of the prism are used: $a = 1\,\mathsf{m}$, $b = 100\,\mathsf{m}$, and $c = 2\,\mathsf{m}$. The length of the prism, b, is set arbitrarily long to reduce the two-dimensional detection problem into a one-dimensional problem. The sought signal has the same dimensions as the observations. In order to derive the sought signal for the filter function the horizontal center coordinates of the prism are set to zero in (3.1) and (3.2) while the computation points are $x_1 = -\frac{(N_1-1)}{2}\Delta x_1, \ldots, \frac{(N_1-1)}{2}\Delta x_1$ and $x_2 = -\frac{(N_2-1)}{2}\Delta x_2, \ldots, \frac{(N_2-1)}{2}\Delta x_2$. N_1 and N_2 are the dimensions of the observation grid. The point interval is given by Δx_1 and Δx_2. Assuming an observation field of 101×101 grid points with a $1\,\mathsf{m}$ spacing leads to $x_1 = x_2 = -50, \ldots, 50$. If the vertical center coordinate of the prism is, for example, ${x_3}' = -3\,\mathsf{m}$, the depth to the top of the prism defined above is $2\,\mathsf{m}$, assuming the observation grid is at zero elevation, $x_3 = 0\,\mathsf{m}$.

In order to ensure that the gravity gradients are given in Eötvös, (3.1) is multiplied by the Gravitational Constant, $G = 6.673 \cdot 10^{-11}\,\mathsf{m}^3/(\mathsf{kg}\,\mathsf{s}^2)$, a scale factor of 10^9, and the density, ρ. However, a void is not simulated by zero density but by the assumed density difference, $\Delta\rho = -2670\,\mathsf{kg}/\mathsf{m}^3$, in contrast to the surrounding rocks. The same multiplications hold for gravity (3.2) in milligal, except that the scale factor is 10^5. The magnetic field generated by the prism is just a combination of the above gravity gradients (3.1) applying Poisson's Relation (2.40). Both the Gravitational Constant and the density contrast thereby cancel out. The scale factor is also 10^9 implying nano-Tesla. Similarly, the magnetic field of the void does not include zero magnetization but the difference in magnetization $\Delta M = \Delta\chi H = -0.005 \cdot 5600\,\mathsf{nT}$.

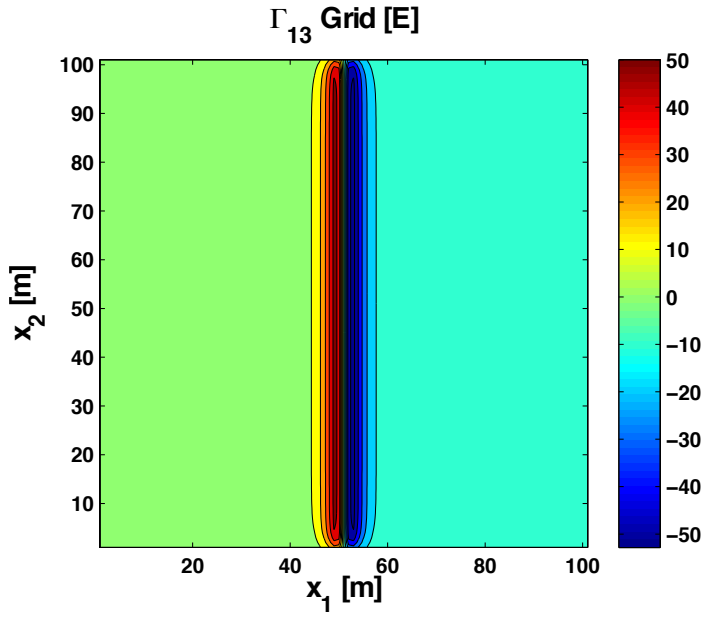

Figure 3.2: Grid of Γ_{13} Signal

The assumed inclination and declination in radians in the NED system are

$$I = 68° \frac{\pi}{180°} \tag{3.4}$$

and

$$D = -7° \frac{\pi}{180°}. \tag{3.5}$$

The actual angles for a specific day are provided online by the National Oceanic and Atmospheric Administration (NOAA).

The simulated sought signal in case of the gradient component Γ_{13}, is plotted in Figure 3.2. The center of the signal (origin of source coordinate system) is moved to the center of the simulated field. The signal is generated by a prism of the above dimensions at 2 m depth to the top of the prism. The length of the prism is clearly reflected in the x_2-direction. The sought signal is zero or close to zero anywhere but above the mass anomaly or in its proximity.

The extension of the mass anomaly in the x_2-direction is designed in order to reduce the initial two-dimensional detection problem to a one-dimensional problem. Now, only the x_1-coordinate of the location is of interest. The sought signal can, therefore, be described by a single horizontal profile taken from the entire grid. The center profile for gravity, the gravity gradients, and the magnetic field is plotted in Figure 3.3 and Figure 3.4, respectively. Since the simulated signal does not vary in x_2-direction, the gravity gradient components Γ_{12} and Γ_{23} equal zero. Γ_{22} is not

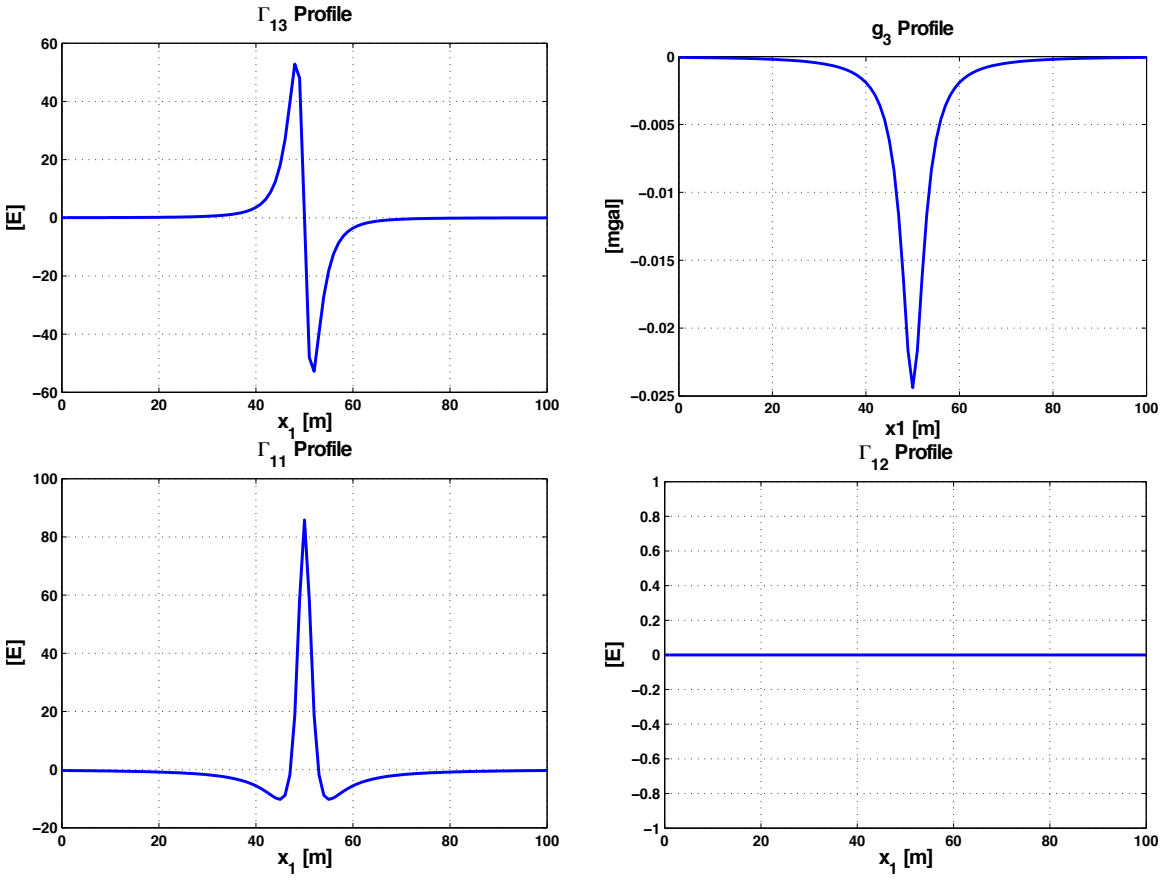

Figure 3.3: a) - d) Sought Signal Profiles

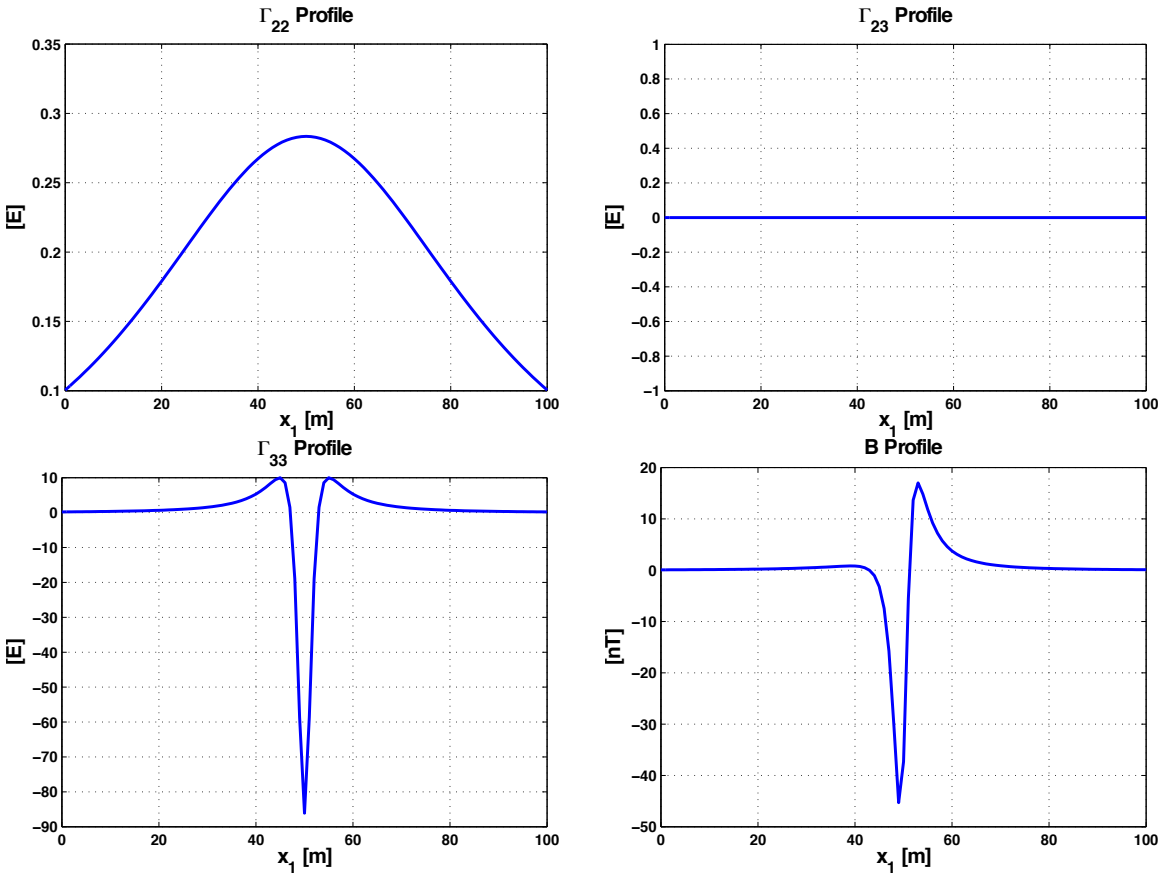

Figure 3.4: e) - h) Sought Signal Profiles

exactly zero due to the finite extension of the prism (100 m in x_2-direction) but as shown here it is still very small (maximum is 0.28 E). Here, due to Laplace's Equation (2.8), $\Gamma_{11} = -\Gamma_{33}$. The asymmetry in B is caused by the direction of the magnetic field.

If an application requires to model the signal of a source that is more advanced in its shape, one possible solution is to combine several three-dimensional prisms together in a way that best fits this shape. The resulting gravity gradients are the total sum of the gravity gradients generated by the individual prisms. Alternatively, other closed formulas as, for example, for a dike or fault [Telford et al., 1990, p.40] can be implemented. This dissertation will only focus on single prism examples but it can easily be updated for other source signal shapes. It has to be regarded though that the signal is restricted to a local extension, i.e. the sought signal is zero for most part of the profile along x_1 except above or close to the anomaly. Otherwise, the MF will encounter edge effects that make it difficult to identify the sought signal.

3.1.2 Observation

The observation vector (2.47), $\mathbf{z}$, consists of a superposition of three signals:

1. The sought signal, $\mathbf{s}$, at the location, $x_1 = x_m$,
2. The noise signal of the background field, and
3. Some random instrument noise.

The sought signal is generated as in Section 3.1.1 but shifted to the left side (x_1-direction) of the field to simulate a new "unknown" location of the source at $x_1 = 30$ m. The random instrument noise is simulated by white noise with zero mean and the respective standard deviations for gravity, σ_g, gravity gradients, σ_Γ, and the magnetic field, σ_B, (Table 3.1).

The major part of the observation, however, is derived from the background field. The background field is based on a covariance model (Section 3.2) for the disturbing potential, T, between two points at $\mathbf{x}$ and $\mathbf{x}'$. The model is introduced in [Jekeli, 2003b] and describes a stationary, Gaussian, stochastic process with zero-mean. The assumption that those properties also apply to the background field is further discussed and justified in [Jekeli and Abt, 2011]. The Fourier transform of the covariance of T results in the corresponding Power Spectral Density (psd) in the frequency domain

$$\Phi_T(\mu_1, \mu_2; x_3, {x_3}') = \sum_j \frac{\sigma_j^2}{\alpha_j \mu} e^{-\frac{2\pi\mu}{\alpha_j}} e^{-2\pi\mu(x_3 + {x_3}')} \tag{3.6}$$

containing the model parameters α_j and σ_j, which are empirically determined from actual data and given in Appendix A. The model presents a sum of functions based

on the different model parameter pairs. The psd depends on the cyclical frequencies

$$\begin{aligned} \mu_1 &= \frac{n_1}{\Delta x_1 N_1} \\ \mu_2 &= \frac{n_2}{\Delta x_2 N_2} \end{aligned} \tag{3.7}$$

and

$$\mu = \sqrt{\mu_1^2 + \mu_2^2}, \tag{3.8}$$

which are defined by the integers

$$\begin{aligned} n_1 &= -\frac{(N_1 - 1)}{2}, \ldots, 0, \ldots, \frac{(N_1 - 1)}{2} \\ n_2 &= -\frac{(N_2 - 1)}{2}, \ldots, 0, \ldots, \frac{(N_2 - 1)}{2}, \end{aligned} \tag{3.9}$$

the point intervals ($\Delta x_1 = \Delta x_2 = 1\,\mathsf{m}$), as well as the dimension of the observation grid ($N_1 = N_2 = 101$).

Assuming that the observation grid is level and at zero height ($x_3 = x_3{}' = 0\,\mathsf{m}$), the psd will simplify to

$$\Phi_T(\mu) = \sum_j \frac{\sigma_j^2}{\alpha_j \mu} e^{-\frac{2\pi\mu}{\alpha_j}}. \tag{3.10}$$

The spectrum of the disturbing potential, T_0, is finally computed from the psd by

$$(T_0)_{n_1,n_2} = (\eta_{n_1,n_2} + i\zeta_{n_1,n_2}) \sqrt{\Delta x_1 N_1 \Delta x_2 N_2} \sqrt{\Phi_T(\mu)} \tag{3.11}$$

(compare (3.45)).

The index n_1, n_2, indicates that T_0 is a matrix of the same dimensions as those of the observation grid in the space domain ($N_2 \times N_1$). The psd, Φ_T, only depends on the magnitude of the cyclical frequencies μ, which on the other hand depends on n_1, n_2. The two newly introduced variables,

$$\begin{aligned} \eta_{n_1,n_2} &\sim \mathcal{N}\left(0, \frac{1}{\sqrt{2}}\right) \\ \zeta_{n_1,n_2} &\sim \mathcal{N}\left(0, \frac{1}{\sqrt{2}}\right), \end{aligned} \tag{3.12}$$

are normally distributed random numbers that will synthesize a random background field. That means a specific set of these random numbers defines one specific background field in the simulations. Up to 1000 different background fields are simulated and evaluated in this research. The two variables have a zero-mean and a standard deviation of $1/\sqrt{2}$ (3.12). This ensures that the variance of the psd of the synthesized field per frequency is equal to the psd of the model.

In the space domain, the gravity and gravity gradients are derived from the first and second spatial derivative of the disturbing potential, respectively. Similar but simpler relationships hold in the frequency domain, leading to the spectra of gravity

$$\begin{aligned} G_1 &= i2\pi\mu_1 T_0 \\ G_2 &= i2\pi\mu_2 T_0 \\ \tilde{G}_3 &= -2\pi\mu T_0 \end{aligned} \tag{3.13}$$

and gravity gradients

$$\begin{aligned} G_{11} &= -4\pi^2\mu_1^2 T_0 \\ G_{12} &= -4\pi^2\mu_1\mu_2 T_0 \\ G_{13} &= -i4\pi^2\mu_1\mu T_0 \\ G_{22} &= -4\pi^2\mu_2^2 T_0 \\ G_{23} &= -i4\pi^2\mu_2\mu T_0 \\ G_{33} &= 4\pi^2\mu^2 T_0. \end{aligned} \tag{3.14}$$

$\tilde{G}_3$ implies the consequent derivative in the NWU coordinate system. However, since gravity is commonly defined as positive downward (in direction towards the mass anomaly), $G_3 = -\tilde{G}_3$ will be utilized in the following. This step is equivalent to the definition of equation (3.3) in the space domain.

The Inverse Fourier Transformation of the above spectra provides the gravity vector (g_1, g_2, g_3) and gravity gradient tensor components (Γ_{11}, Γ_{12}, Γ_{13}, Γ_{22}, Γ_{23}, Γ_{33}) in the space domain. Furthermore, the gradients can be combined as, for example,

$$\begin{aligned} &2\Gamma_{12} \\ &\Gamma_{22} - \Gamma_{11}, \end{aligned} \tag{3.15}$$

which is measured in the specific instrument frame by the Bell Aerospace/Lockheed Martin gradiometer [Jekeli, 1988].

In order to preserve consistency, all gravity and gravity gradient components are based on the same T_0, which again is defined by its specific set of random variables, η and ζ. The magnetic field, B, in the space domain is computed, by combining the gravity gradients according to Poisson's Relation (2.40) with the values of (2.10), (3.4), and (3.5).

Figure 3.5, Figure 3.6, and Figure 3.7 present the background realizations of the first out of 1000 fields for g_3, Γ_{33}, and B, respectively. The black line in each plot shows a profile at $x_2 = 37\,\mathsf{m}$, which is taken for the further simulations. Instead of searching the entire area of $100\,\mathsf{m}^2$, only this profile of $100\,\mathsf{m}$ length will be analyzed. The simulated setup is shown by Figure 3.8. It has to be noted that while the entire area has a zero-mean this is not necessarily true for the single profile. At this point, the synthetic observations are not entirely consistent with the covariance function anymore, which assumes a zero-mean.

Figure 3.9 a) summarizes the three signals that go into the superposition of the observation vector, z, in case of the gradient component Γ_{33}. The prism is modeled at a depth of 2 m. Figure 3.9 b) plots the resulting observation profile. The center of the sought signal at $x_1 = 30\,\mathsf{m}$ is not obvious in these observations.

3.2 Covariance Model

The covariance model [Jekeli, 2003b], which is used to describe the noise of the background field, is based on the following planar reciprocal distance model

$$\phi_T\left(\mathrm{dx}_1, \mathrm{dx}_2; x_3, x_3'\right) = \sum_j \frac{\sigma_j^2}{\sqrt{\left(1 + \alpha_j\left(x_3 + x_3'\right)\right)^2 + \alpha_j^2 r^2}}. \tag{3.16}$$

It is a sum of functions with various model parameter values, α_j and σ_j. The psd (3.10) is the Fourier Transform of (3.16) including the same model parameters (Appendix A); therefore, the covariance model is consistent with the synthetically generated background field. The covariance matrix, ϕ_T, designed for the disturbing potential, T, is symmetric and positive definite since the noise generated by the background field is assumed to be stationary with a zero-mean.

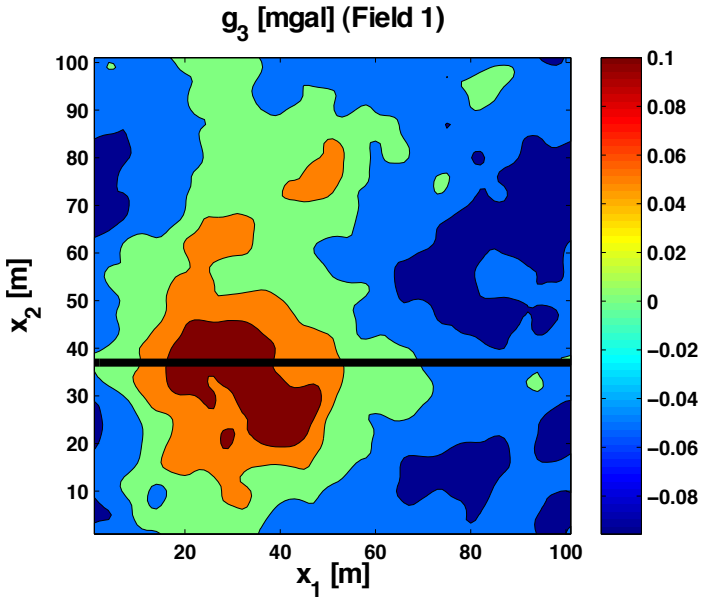

Figure 3.5: g_3 Background with Observation Profile

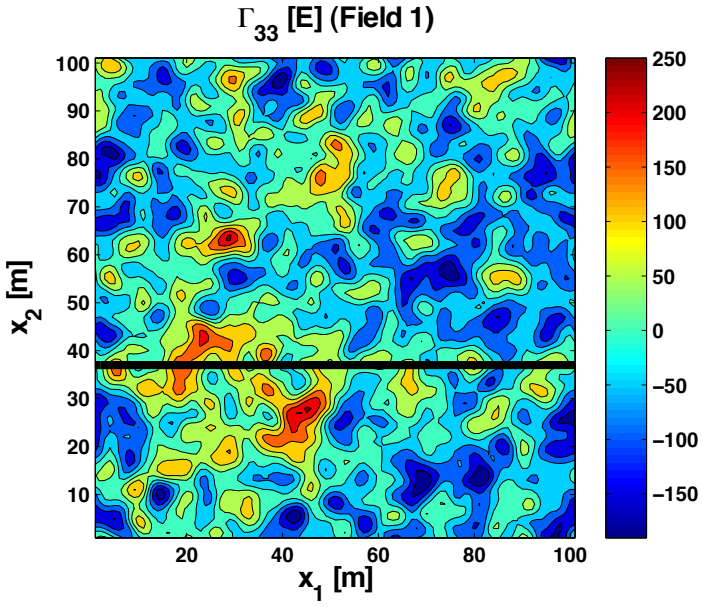

Figure 3.6: Γ_{33} Background with Observation Profile

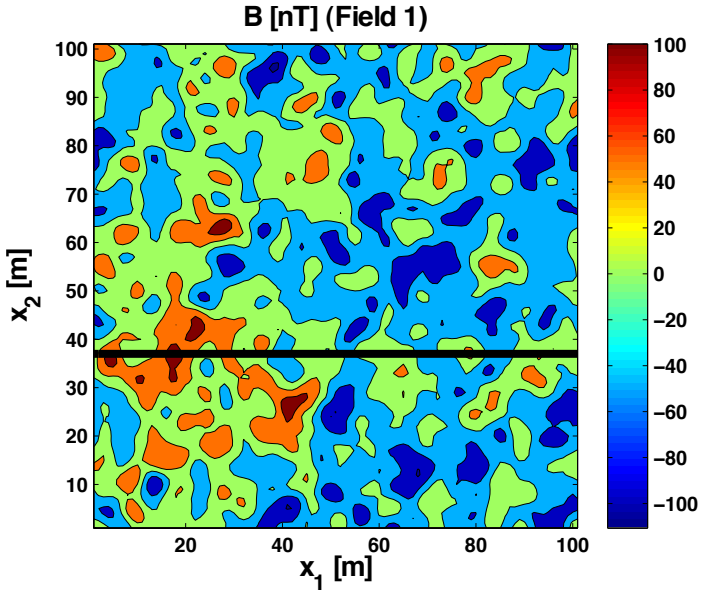

Figure 3.7: B Background with Observation Profile

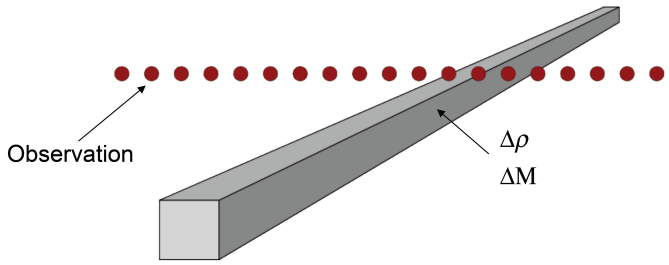

Figure 3.8: Schematic Setup of Observation Profile

The horizontal coordinate differences,

$$\begin{aligned} \mathrm{dx}_1 &= x_1 - x_1{}' \\ \mathrm{dx}_2 &= x_2 - x_2{}', \end{aligned} \tag{3.17}$$

are defined as the coordinates of the first point minus the coordinates of the second point. The horizontal distance is, therefore,

$$r = \sqrt{\mathrm{dx}_1^2 + \mathrm{dx}_2^2}. \tag{3.18}$$

Assuming again, that all points lie on a planar grid at a height of $x_3 = x_3{}' = 0$ and defining the following abbreviations

$$\begin{aligned} \beta_j &= 1 + \alpha_j \left(x_3 + x_3{}'\right) \\ M_j &= \beta_j^2 + \alpha_j^2 r^2 \end{aligned} \tag{3.19}$$

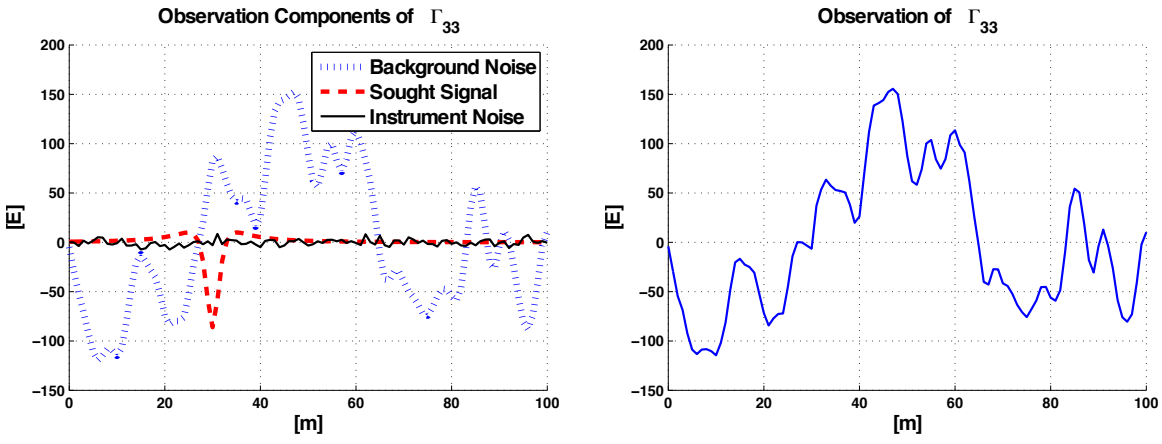

Figure 3.9: a) Observation Components b) Total Observation

Observation Type		Instrument Noise
Gravity	σ_g	0.01 mgal
Gravity Gradients	σ_Γ	3 E
Magnetic Field	σ_B	1 nT

Table 3.1: Sensor Specific Standard Deviations

where $\beta_j = 1$, leads to the simplified covariance model for the disturbing potential T

$$\phi_T\left(\mathrm{dx}_1, \mathrm{dx}_2\right) = \sum_j \frac{\sigma_j^2}{\sqrt{M_j}}. \tag{3.20}$$

ϕ_T is isotropic as it only depends on the distance, r, between two points, (x_1, x_2) and $(x_1{}', x_2{}')$.

The element in the MF function, $\phi^{-1}\left(-x_j, -x_k\right)$, as defined in (2.51) and derived in Section 2.3.2, is an element (for one data type) or a submatrix (for a combination of data types) of the inverse of the entire covariance matrix, Φ. The covariance matrix is a summation of the matrix that describes the noise of the background field, Φ_{bg}, and the matrix that describes the instrument noise, Φ_i, as given by

$$\Phi = \Phi_{\mathrm{bg}} + \Phi_i. \tag{3.21}$$

While Φ_{bg} is based on the model function (3.16) and will be derived in the following sections, Φ_i is simply a diagonal matrix as the instrument noise is uncorrelated. The diagonal elements are the noise variances of the corresponding sensor. Typical standard deviations for gravimeter, gradiometer, and magnetometer noise are provided in Table 3.1. The noise generated by the background field and by the instrument is uncorrelated to each other. The dimension of Φ is

$$\left(N_1 \cdot N_2 \cdot n_{\mathrm{data}}\right) \times \left(N_1 \cdot N_2 \cdot n_{\mathrm{data}}\right) \tag{3.22}$$

with n_{data} being the number of observation types. For example, if $n_{\mathrm{data}} = 3$ for an observation combination of g_3, Γ_{33}, and Γ_{13}, and a profile ($N_2 = 1$) of $N_1 = 101$ observed points leads to a covariance matrix of 303×303 size. While the covariance model for gravity and gravity gradients is designed for local and regional applications, it should be reminded, that the following covariances for the magnetic field only hold within a restricted area where the conditions for Poisson's Relation (2.20) are not violated.

3.2.1 Gravity and Gravity Gradients

The covariances of the gravity and gravity gradient tensor components can be derived by applying covariance propagation [Moritz, 1989, p.86] to the basic covariance model of the disturbing potential (3.20). This is possible since g and Γ are directly related to T (compare (2.3), (2.4), and (2.5)).

The covariances of the components g_3,

$$\phi_{g_3} = \frac{\sigma_j^2 \alpha_j^2}{M_j^{\frac{5}{2}}} \left(2\beta_j^2 - \alpha_j^2 r^2\right), \tag{3.23}$$

and Γ_{33},

$$\phi_{\Gamma_{33}} = \frac{3\sigma_j^2 \alpha_j^4}{M_j^{\frac{9}{2}}} \left(8\beta_j^2 - 24\beta_j^2 \alpha_j^2 r^2 + 3\alpha_j^4 r^4\right), \tag{3.24}$$

are also isotropic but other components might depend on dx_1 or dx_2 (3.17).

Covariance propagation also computes the cross-covariances between the gravity and gravity gradients, as e.g.

$$\phi_{g_3,\Gamma_{33}} = \frac{3\sigma_j^2 \alpha_j^3 \beta_j}{M_j^{\frac{7}{2}}} \left(-2\beta_j^2 + 3\alpha_j^2 r^2\right) = \phi_{\Gamma_{33},g_3}. \tag{3.25}$$

Furthermore, the covariances of linear gravity gradient combinations (3.15) such as described in Section 3.1.2 are also derived by covariance propagation assuming a zero mean:

$$\begin{aligned} \phi_{\Gamma_{22}-\Gamma_{11}} &= \varepsilon\big((\Gamma_{22} - \Gamma_{11})\,(\Gamma_{22} - \Gamma_{11})\big) \\ &= \varepsilon\left(\Gamma_{22}^2 - 2\Gamma_{11}\Gamma_{22} + \Gamma_{11}^2\right) \\ &= \phi_{\Gamma_{11}} + \phi_{\Gamma_{22}} - 2\phi_{\Gamma_{11},\Gamma_{22}}, \end{aligned} \tag{3.26}$$

$$\phi_{2\Gamma_{12}} = 4\phi_{\Gamma_{12}}^2, \tag{3.27}$$

$$\phi_{2\Gamma_{12},\Gamma_{22}-\Gamma_{11}} = 2\phi_{\Gamma_{12},\Gamma_{22}} - 2\phi_{\Gamma_{12},\Gamma_{11}}. \tag{3.28}$$

All of the above covariance equations refer to the NWU coordinate system where gravity is defined to point positively downward according to (3.3).

3.2.2 Gravity Gradients and Magnetic Field

Poisson's Relation states that under certain conditions (2.20) the magnetic field is directly related to the gravity gradients. Hence, covariances between B and Γ can be propagated in the same way (assuming zero mean) as the covariances between g and Γ, if the conditions are fulfilled and the direction cosines of magnetization (α, β, γ) are known (2.36). The resulting covariances, for example, for Γ_{33} and B are

$$\phi_{\Gamma_{33},B} = \alpha\phi_{\Gamma_{33},B_1} + \beta\phi_{\Gamma_{33},B_2} + \gamma\phi_{\Gamma_{33},B_3} \tag{3.29}$$

and

$$\phi_{B,\Gamma_{33}} = \alpha\phi_{B_1,\Gamma_{33}} + \beta\phi_{B_2,\Gamma_{33}} + \gamma\phi_{B_3,\Gamma_{33}}. \tag{3.30}$$

The above covariances are based on the covariances between gravity gradients and the magnetic field vector components:

$$\phi_{\Gamma_{33},B_1} = \frac{\mu_0\chi H}{4\pi G\rho}\left(\alpha\phi_{\Gamma_{33},\Gamma_{11}} + \beta\phi_{\Gamma_{33},\Gamma_{12}} + \gamma\phi_{\Gamma_{33},\Gamma_{13}}\right), \tag{3.31}$$

$$\phi_{\Gamma_{33},B_2} = \frac{\mu_0\chi H}{4\pi G\rho}\left(\alpha\phi_{\Gamma_{33},\Gamma_{12}} + \beta\phi_{\Gamma_{33},\Gamma_{22}} + \gamma\phi_{\Gamma_{33},\Gamma_{23}}\right), \tag{3.32}$$

$$\phi_{\Gamma_{33},B_3} = \frac{\mu_0\chi H}{4\pi G\rho}\left(\alpha\phi_{\Gamma_{33},\Gamma_{13}} + \beta\phi_{\Gamma_{33},\Gamma_{23}} + \gamma\phi_{\Gamma_{33}}\right), \tag{3.33}$$

$$\phi_{B_1,\Gamma_{33}} = \frac{\mu_0\chi H}{4\pi G\rho}\left(\alpha\phi_{\Gamma_{11},\Gamma_{33}} + \beta\phi_{\Gamma_{12},\Gamma_{33}} + \gamma\phi_{\Gamma_{13},\Gamma_{33}}\right), \tag{3.34}$$

$$\phi_{B_2,\Gamma_{33}} = \frac{\mu_0\chi H}{4\pi G\rho}\left(\alpha\phi_{\Gamma_{12},\Gamma_{33}} + \beta\phi_{\Gamma_{22},\Gamma_{33}} + \gamma\phi_{\Gamma_{23},\Gamma_{33}}\right), \tag{3.35}$$

$$\phi_{B_3,\Gamma_{33}} = \frac{\mu_0\chi H}{4\pi G\rho}\left(\alpha\phi_{\Gamma_{13},\Gamma_{33}} + \beta\phi_{\Gamma_{23},\Gamma_{33}} + \gamma\phi_{\Gamma_{33}}\right). \tag{3.36}$$

A complete list of the gravity gradient and magnetic field covariances is provided in Appendix B. The auto-covariance for B is also derived by covariance propagation

$$\phi_B = \alpha^2\phi_{B_1} + 2\alpha\beta\phi_{B_1,B_2} + \beta^2\phi_{B_2} + \gamma^2\phi_{B_3} \tag{3.37}$$

where some cross-covariances cancel out according to the negative symmetries in the covariances between certain gradient combinations. Equation (3.37) includes the auto-covariances of the magnetic field vector components:

$$\phi_{B_1} = \left(\frac{\mu_0\chi H}{4\pi G\rho}\right)^2\left(\alpha^2\phi_{\Gamma_{11}} + 2\alpha\beta\phi_{\Gamma_{11},\Gamma_{12}} + \beta^2\phi_{\Gamma_{12}} + \gamma^2\phi_{\Gamma_{13}}\right), \tag{3.38}$$

$$\phi_{B_2} = \left(\frac{\mu_0\chi H}{4\pi G\rho}\right)^2\left(\alpha^2\phi_{\Gamma_{12}} + 2\alpha\beta\phi_{\Gamma_{12},\Gamma_{22}} + \beta^2\phi_{\Gamma_{22}} + \gamma^2\phi_{\Gamma_{23}}\right), \tag{3.39}$$

$$\phi_{B_3} = \left(\frac{\mu_0\chi H}{4\pi G\rho}\right)^2\left(\alpha^2\phi_{\Gamma_{13}} + 2\alpha\beta\phi_{\Gamma_{13},\Gamma_{23}} + \beta^2\phi_{\Gamma_{23}} + \gamma^2\phi_{\Gamma_{33}}\right). \tag{3.40}$$

A full list of the magnetic field covariances is provided in Appendix C.

3.2.3 Magnetic Field and Gravity

In contrast to Section 3.2.1 and Section 3.2.2, there is no simple relationship between gravity and the magnetic field. This complicates a covariance propagation in the space domain. For that reason the problem is transformed to the frequency domain. [Jekeli, 2009] derives an expression for the spectrum of the magnetic field. This expression utilizes Poisson's Relation in the frequency domain and is either based on the spectrum of the gravitational potential

$$B^{(V)}(\mu_1, \mu_2, z) = \frac{\mu_0 \chi H}{4\pi G\rho} \left(2\pi i \left(\alpha\mu_1 + \beta\mu_2\right) - \gamma\mu\right)^2 V(\mu_1, \mu_2, z), \tag{3.41}$$

the spectrum of the gravity vector components, as, for example,

$$B^{(g_3)}(\mu_1, \mu_2, z) = \frac{\mu_0 \chi H}{4\pi G\rho} \frac{\left(2\pi i \left(\alpha\mu_1 + \beta\mu_2\right) - \gamma\mu\right)^2}{-\mu} \frac{\partial V}{\partial z}(\mu_1, \mu_2, z) \tag{3.42}$$

or the spectrum of the gravity gradients such as

$$B^{(\Gamma_{33})}(\mu_1, \mu_2, z) = \frac{\mu_0 \chi H}{4\pi G\rho} \frac{\left(2\pi i \left(\alpha\mu_1 + \beta\mu_2\right) - \gamma\mu\right)^2}{\mu^3} G_{33}(\mu_1, \mu_2, z) \tag{3.43}$$

and

$$B^{(\Gamma_{31})}(\mu_1, \mu_2, z) = \frac{\mu_0 \chi H}{4\pi G\rho} \frac{\left(i \left(\alpha\mu_1 + \beta\mu_2\right) - \gamma\mu\right)^2}{-i\mu_1\mu} G_{31}(\mu_1, \mu_2, z). \tag{3.44}$$

The above equations are in the NWU coordinate system and the cyclical frequencies μ_1, μ_2 (3.7), μ (3.8) indicate that the magnetic field, the gravity potential and its derivatives are given in the frequency domain. The output of each equation is theoretically the same, however, the latter ones have to compensate for the division by zero since the zero frequency is included. This is due to the fact that the zero frequency components of g_3 in (3.13) and Γ_{33} in (3.14) are zero and by Poisson's Relation, the pseudo-magnetic field must also have zero for the zero-frequency term. If those cases are simply set to zero, some information will be lost, so that, for example $B^{(V)} \neq B^{(\Gamma_{33})}$. For that reason, the magnetic field is here only derived from the gravitational potential, using (3.41). A quick test of the simulations shows that the Inverse Fourier Transformation of (3.41) equals the pseudo-magnetic field directly computed in the space domain (2.40) up to residuals about $10^{-14}\,\mathsf{nT}$.

An auto-periodogram of an observation field is computed by multiplying the spectrum of a data set with its complex conjugate

$$\Phi_{gg} = \frac{1}{\Delta x_1 N_1 \Delta x_2 N_2} G^*_{k_1 k_2}(\mu_1, \mu_2)\, G_{k_1 k_2}(\mu_1, \mu_2) \tag{3.45}$$

where Δx_1, Δx_2 are the point intervals, $N_1 \times N_2$ is the dimension of the grid and $*$ denotes the complex conjugate.

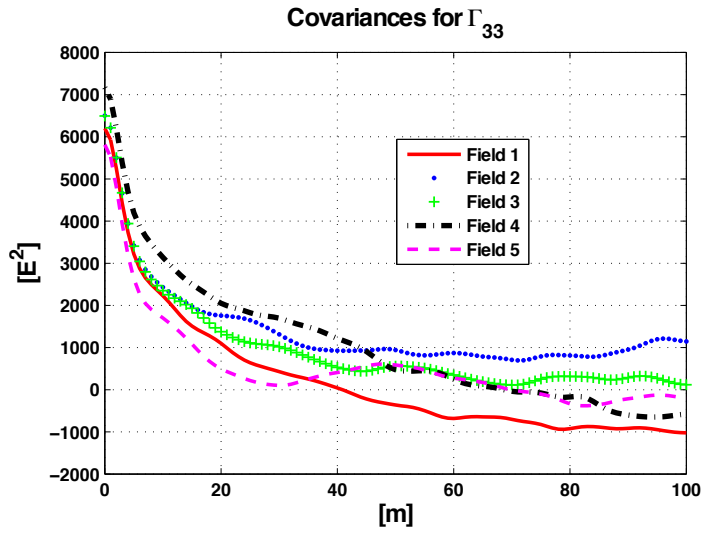

Figure 3.10: Empirical Covariances based on Individual Fields

A cross-periodogram of an observation field is computed by multiplying the spectra of two different types of data, e.g. insert for G the Fourier transform of g_3 and for H the Fourier transform of B:

$$\Phi_{gh} = \frac{1}{\Delta x_1 N_1 \Delta x_2 N_2} G^*_{k_1 k_2}(\mu_1, \mu_2)\, H_{k_1 k_2}(\mu_1, \mu_2)\,. \tag{3.46}$$

Transforming the periodogram into the space domain

$$\begin{aligned}(\phi_{gh})_{l_1 l_2} &= \mathrm{IDFT}\,(\Phi_{gh})_{k_1 k_2} \\ &= \frac{1}{\Delta x_1 N_1 \Delta x_2 N_2} \sum_{k_1=0}^{N_1-1} \sum_{k_2=0}^{N_2-1} (\Phi_{gh})_{k_1 k_2}\, e^{i2\pi\left(\frac{k_1 l_1}{N_1} + \frac{k_2 l_2}{N_2}\right)}\end{aligned} \tag{3.47}$$

results in the covariance matrix between the corresponding data combinations, as e.g. $\phi_{g_3,B}$.

Figure 3.10 shows the resulting covariances of Γ_{33} for five different fields generated by five different sets of random numbers. For simplifications, Figure 3.10 only shows the covariances over distance instead of the arrangements of the entire covariance matrix of size (3.22). Field 1 through Field 5 do not generate exactly the same covariances. This occurs mostly for the long wavelengths due to the limitation of data. In order to determine the covariances for a distance of up to 100 m along the coordinate axes, a 201×201 periodogram is produced, i.e. N_1 and N_2 in (3.46) are set to 201. Figure 3.11 represents ϕ_{gh} for the data combination $G = B^{(V)}$ and $H = G_{13}$ based on Field 1 and Field 5, respectively. Here, the zero-distance component is shifted to the

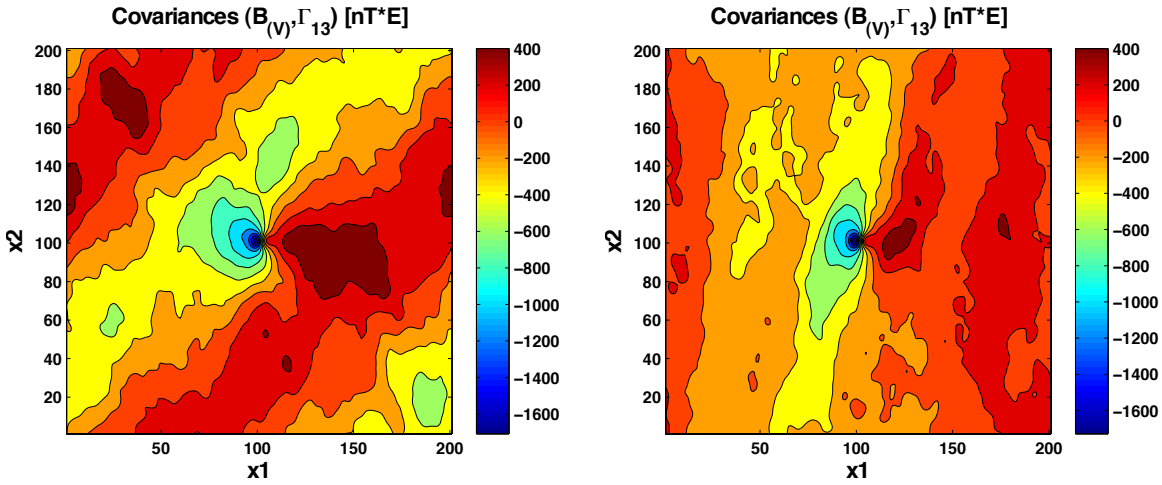

Figure 3.11: Covariances derived from a) Field 1 b) Field 5

center of the grid so that the center of the plot defines the cross-variance at the same observation point. Covariances between two different points depend on their relative horizontal distances ($\mathrm{dx}_1 = -100\,\mathrm{m}, \ldots, 100\,\mathrm{m}$ and $\mathrm{dx}_2 = -100\,\mathrm{m}, \ldots, 100\,\mathrm{m}$). Since ϕ_{gh} differs depending on the Field, which is defined by its set of random numbers, the mean of the 1000 simulated fields is computed. The resulting $\bar{\phi}_{gh}$ are presented in Figure 3.12, Figure 3.13, and Figure 3.14.

3.2.4 Verification

In contrast to the covariances defined by the model [Jekeli, 2003b], the covariances computed from the periodogram are empirical covariances. This section compares the empirical covariances to the model covariances by plotting both over distance. These theoretical and empirical covariances are supposed to be the same since the same model is also used to generate the psd for the 1000 simulated fields in the periodogams. However, as Figure 3.10 in the example for Γ_{33} illustrates, the empirical covariances of various fields diverge over the longer distances, which correspond to the longer wavelengths. This divergence is explained by the limitation of data in the periodogram. A 101×101 observation grid requires a periodogram of the size of at least 201×201 entries. Hence, the 1x101 simulated profile of 100m length in this thesis requires at least a 1×201 point periodogram. Figure 3.15 illustrates, however, if more data are involved, e.g. a periodogram of 1×1001 points generating a $500\,\mathrm{m}$ profile, the covariances derived from the periodogram move closer to the model. This effect corresponds to the rule of thumb that empirical covariances are only reliable up to a lag distance that is 10 % of the available data domain. For that reason, all

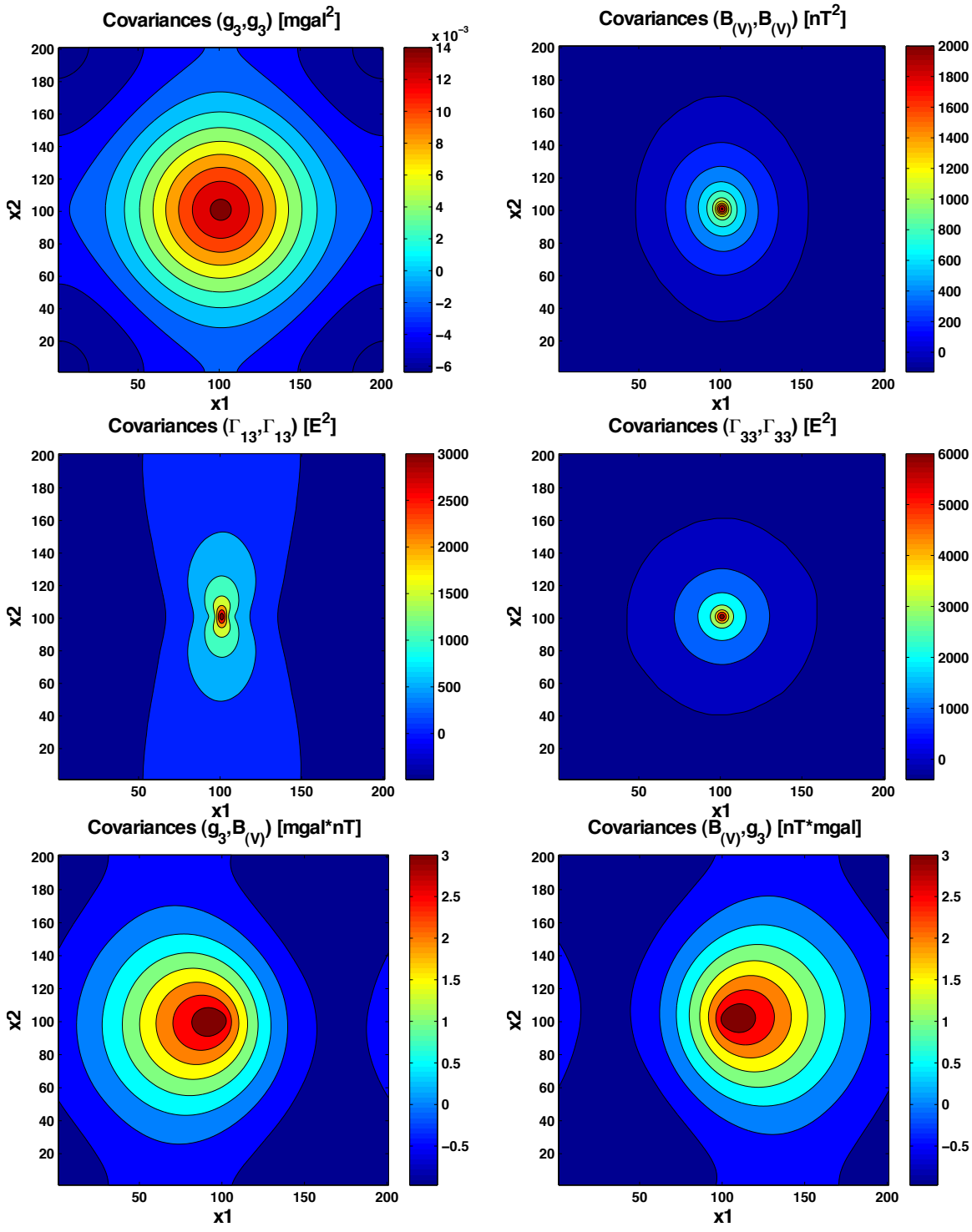

Figure 3.12: a) - f) Covariances derived from Field 1-1000

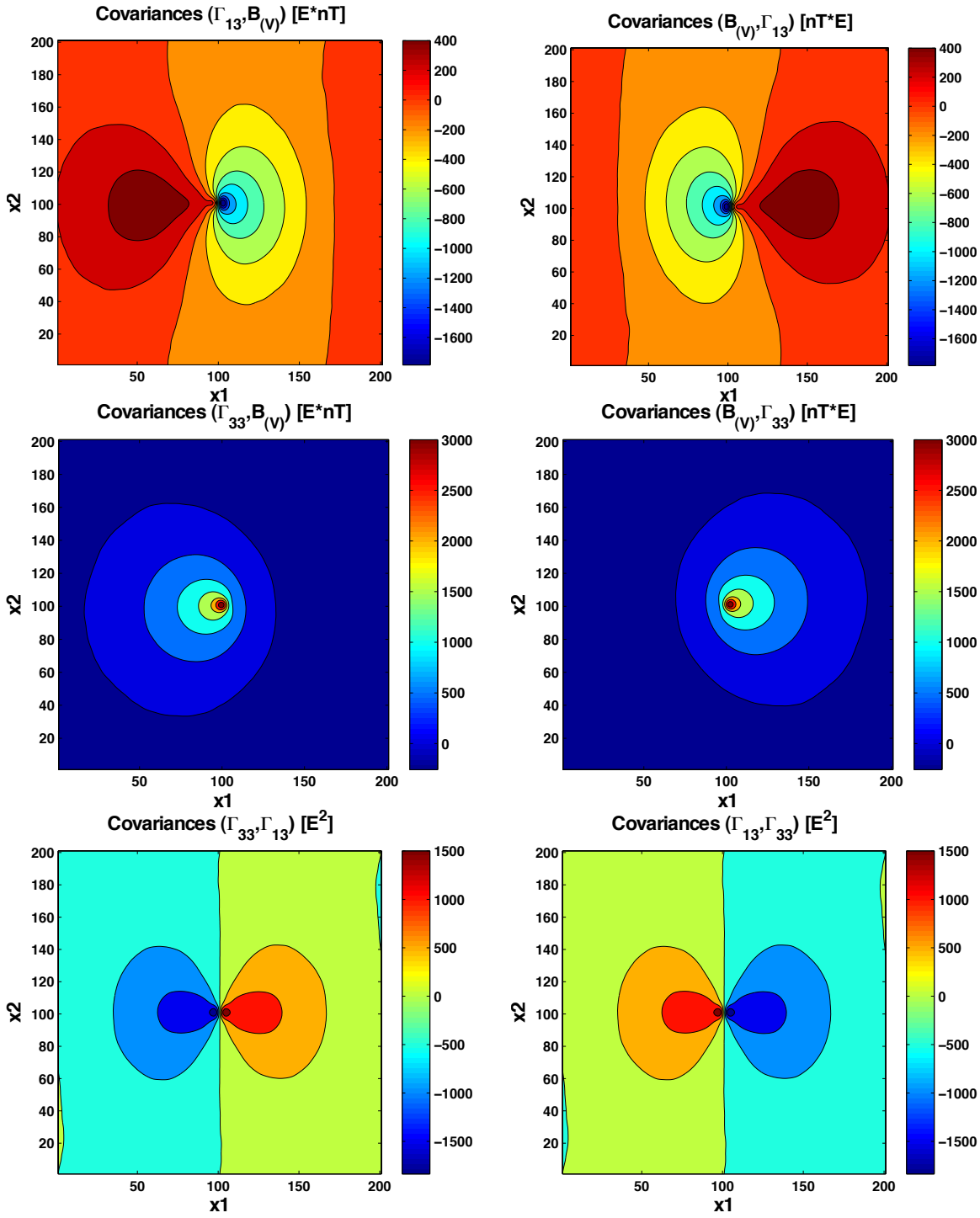

Figure 3.13: g) - l) Covariances derived from Field 1-1000

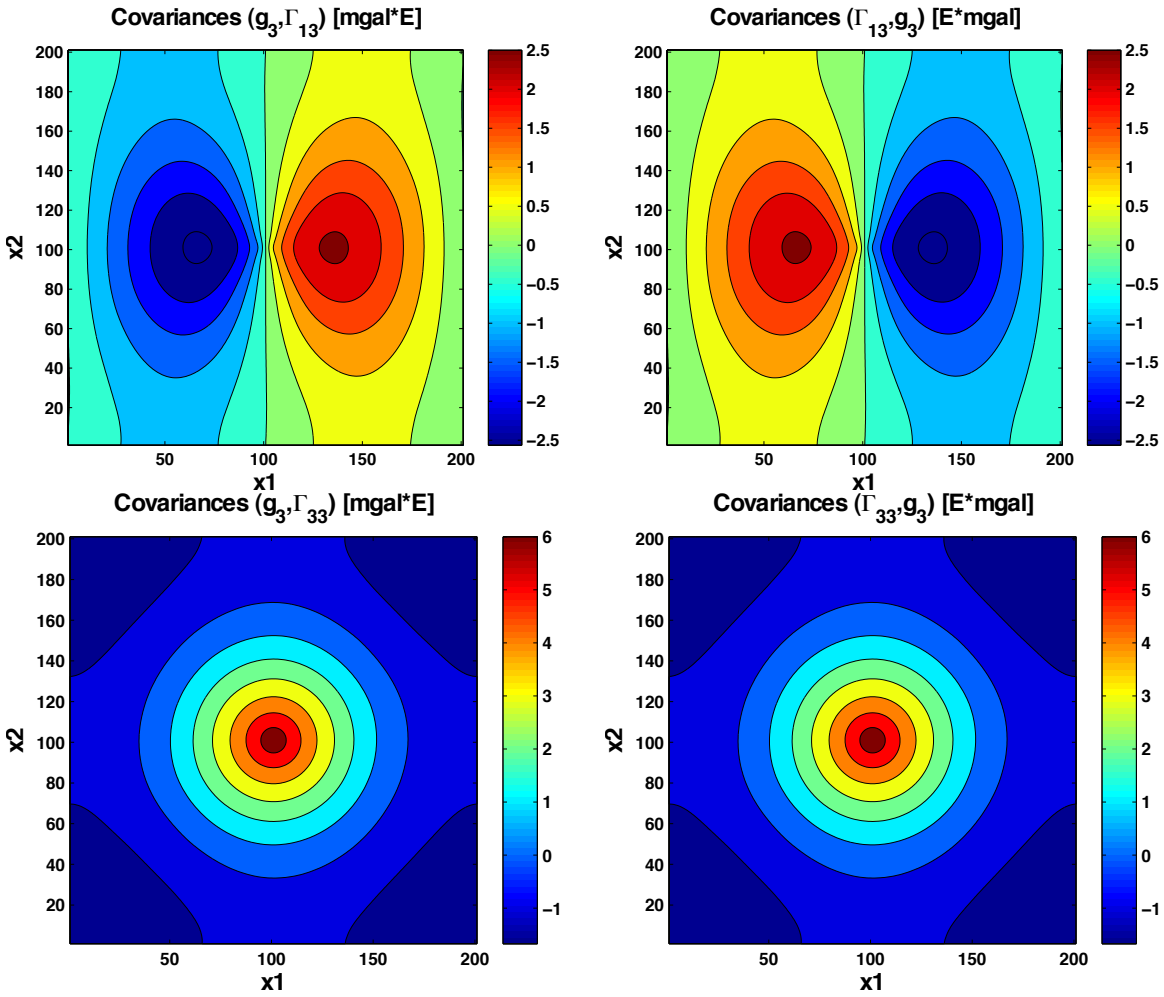

Figure 3.14: m) - p) Covariances derived from Field 1-1000

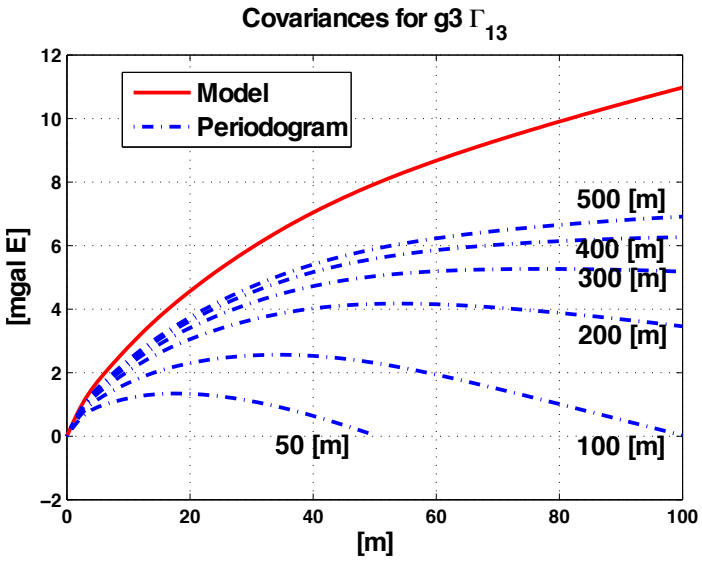

Figure 3.15: Influence of Grid Size in Periodogram Method

empirical covariances that are derived from the periodogram in this dissertation are from now on based on a 1×1001 periodogram. The resulting empirical covariances are compared to the model in Figure 3.16 and Figure 3.17. The covariances of the gravity gradients, Γ_{33} and Γ_{13}, seem to be consistent with regard to the comparison of model versus periodogram and so are the covariances of the magnetic field, B. A constant needs to be subtracted from the covariances generated by the periodograms in order to adjust those curves to the model. The remaining plots point out that in some cases an adjusting constant is necessary while for some other combinations it is not. This can be explained by the fact that the model takes into account the long wavelength signals of the Earth, which are not properly represented in the limited area that derives the empirical covariances. However, simulations show that this constant does not influence the overall detection performance of the MF.

The covariances for gravity diverge more strongly for a point distance longer than 30 m. However, it has to be considered that the overall quantities in this case are small compared to the covariances of the other data components. The covariances of data combinations start to diverge after around 30 m distance (e.g. $\phi_{\Gamma_{33},\Gamma_{13}}$) or stay close up to a distance of almost 80 m (e.g. $\phi_{\Gamma_{33},B}$). $\phi_{g_3,\Gamma_{13}}$ drifts apart after only a few meters although the overall values in that case are also relatively small. This entire exercise demonstrates that it is legitimate to compute the covariances by applying the periodogram method. This is necessary in the case of gravity and magnetic field combinations as there is no linear equation that relates those two quantities to each other, which would allow for covariance propagation. An alternative in the

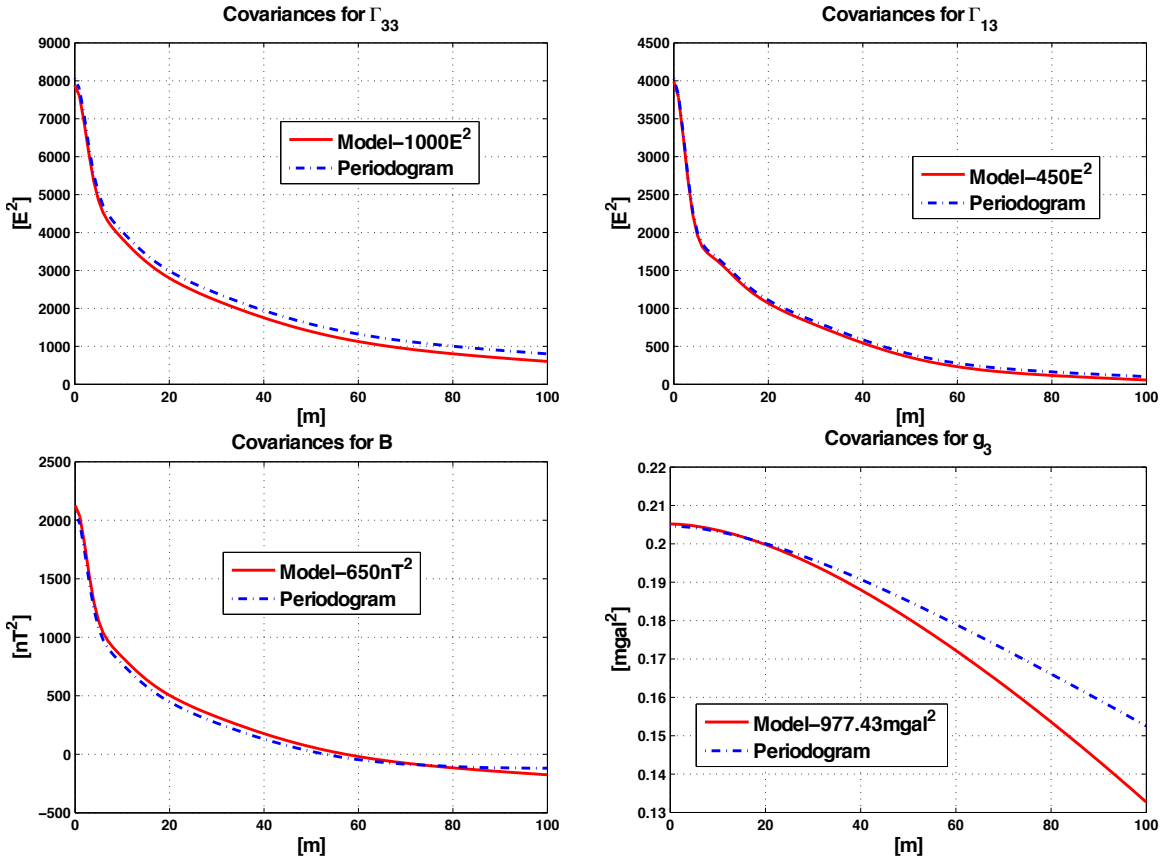

Figure 3.16: a) - d) Model vs. Periodogram

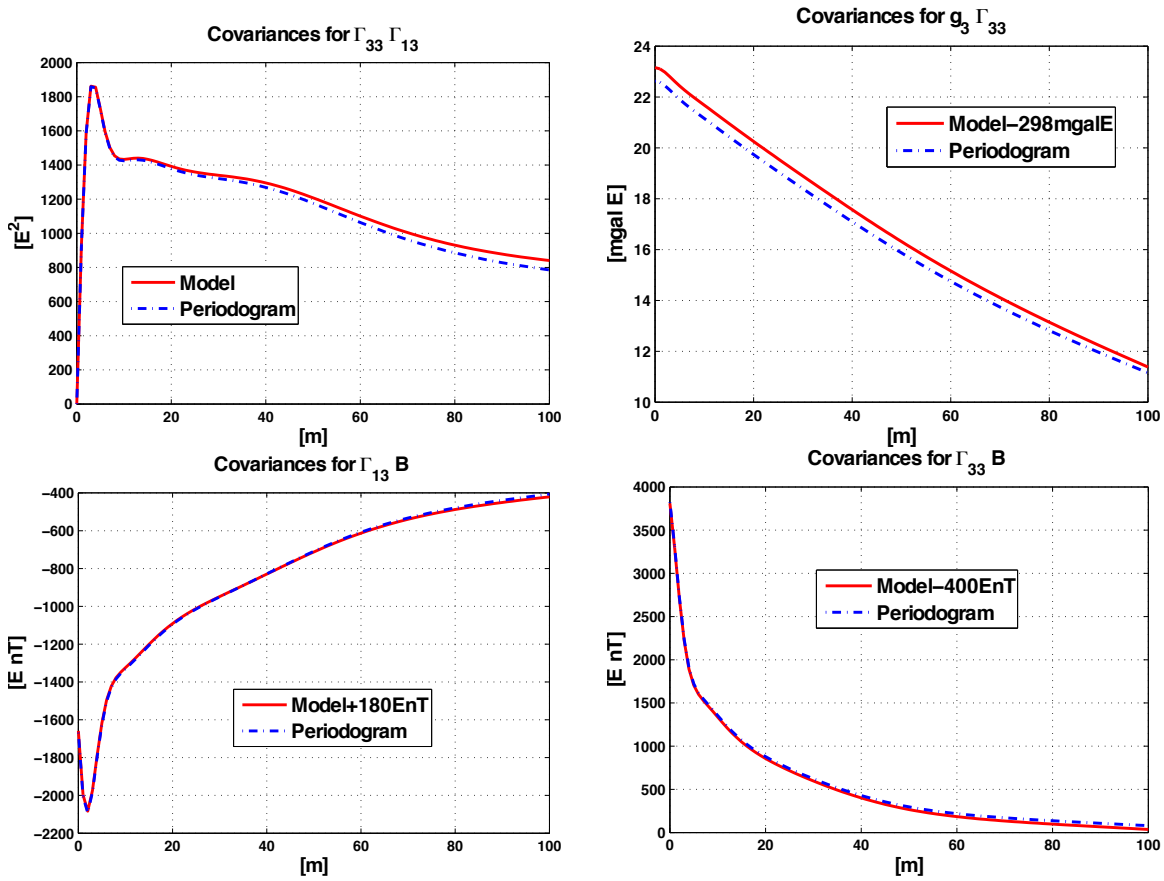

Figure 3.17: e) - h) Model vs. Periodogram

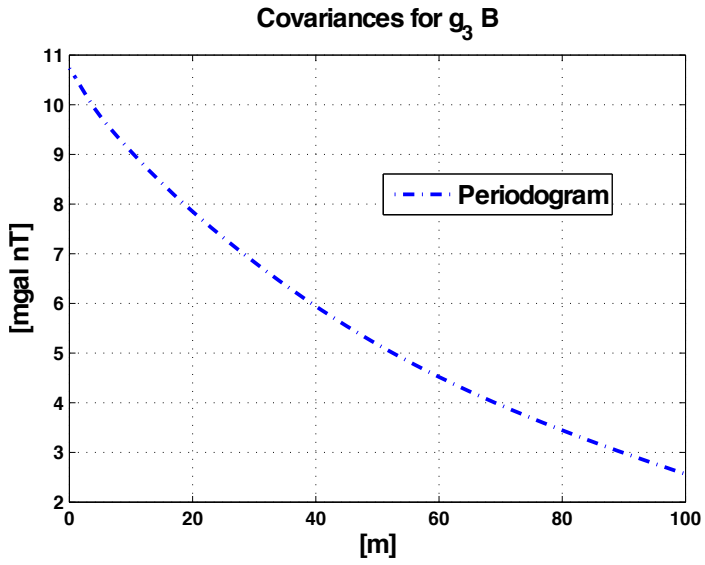

Figure 3.18: Periodogram Method Result for $\phi_{g_3,B}$

space domain would be the empirical determination of the covariance function. This, however, requires a high computational effort in order to yield reasonable results.

The periodogram method finally allows to derive $\phi_{g_3,B}$ (Figure 3.18), which is required for the upcoming MF simulations in Section 3.3. All covariance matrices that do not require $\phi_{g_3,B}$ remain as described in Section 3.2.1 and Section 3.2.2, which are based on the covariance model (3.20).

3.3 Matched Filter Performance

The domain of the MF output equals the domain of the observations. That means a 1×101 observation profile results in a y vector of 1×101 entries, where the maximum, $y_{\max}$, indicates the location of the mass anomaly. Each entry of the filter output is computed by the general equation

$$\underset{[1\times1]}{y} = \underset{[1\times1]}{1/\lambda} \cdot \underset{[1\times101]}{\bar{\mathbf{s}}^T} \cdot \underset{[101\times101]}{\Phi^{-1}} \cdot \underset{[101\times1]}{\mathbf{z}}, \tag{3.48}$$

which also labels the matrix dimensions in case only one type of data is utilized. More data types will alter the dimensions of the observation and sought signal vectors as well as the dimension of the covariance matrix, respectively. (3.48) is a computational sub-step for each x_{r} of the summation in (2.69). Φ stands for the covariance matrix as defined in (2.51) and as derived in Section 3.2.

Observation Type		Detection Rate [%] 2 m	3 m	4 m	5 m
Gravity	g_3	24.7	15.1	10.6	9.4
Gravity Gradients	Γ_{11}	90.2	21.7	14.0	11.6
	Γ_{33}	88.2	19.2	12.6	10.9
	Γ_{13}	84.9	16.0	10.5	8.6
Magnetic Field	B	96.1	17.4	10.5	9.7

Table 3.2: Detection Rates for Individual Type of Data Components and Depths

3.3.1 Comparison of Types of Data

A Monte Carlo simulation is carried out based on the setup described in Section 3.1. 1000 fields, each defined by a specific set of random numbers that simulate the background noise, are generated and entered in the simulations. This number is sufficient to analyze the characteristics of the MF as tests have shown that even only 100 different fields lead to very similar filter results. The input data for the MF is either the simulated g_3, Γ_{11}, Γ_{33}, Γ_{13}, or B. As described above, the source is a prism with the dimensions of $a = 1\,\mathsf{m}$, $b = 100\,\mathsf{m}$, $c = 2\,\mathsf{m}$ placed at various depths. Table 3.2 summarizes the percentage of successful detections out of the 1000 simulation runs, where success means $y_{\max}$ is located in the range of $x_1 = 30\,\mathsf{m} \pm 2\,\mathsf{m}$. The columns correspond to the various depths of the top of the mass anomaly. The results demonstrate that, in comparison, gravity is the least successful data while the results of all the gravity gradient components are similar to each other. The results of the magnetic field are in a similar range than the gravity gradients since B is derived from their linear combination. Γ_{11} is slightly more successful than Γ_{33}. Both components generate the same sought signal with opposite signs due to Laplace's Equation (2.8) and $\Gamma_{22} \approx 0$. However, the background noise defined by Γ_{33} is generally larger than that defined by Γ_{11}. The predominance of Γ_{11} over Γ_{33} in the success rate of MF is, therefore, consistent with a larger SNR. In general, as the signal strength decreases with depth, the MF performance attenuates as well. Figure 3.19 illustrates the dependence between depth and successful detection. The figure also contains the results from Table 3.2. The data g_3, Γ_{33} and B are hereby analyzed.

It becomes again obvious that the MF performance based on g_3 stands out as being the least effective in contrast to those of the other components. Even if the prism is only half a meter deep, the g_3 component detects the prism in less than 90 % of the times. Utilizing B, has an effect similar to utilizing Γ_{33}. One exception is at the depth of 2 m where the magnetic field is about 10 % more successful than

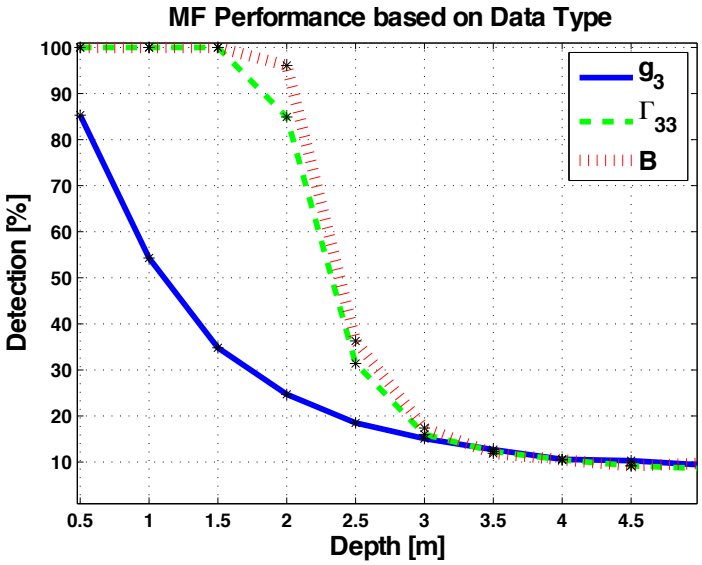

Figure 3.19: Detection Rates for Different Types of Data

the gradient. This can be explained by the fact that B is derived from a weighted combination of gradients, where Γ_{33} has the most significant influence. The sought signal is weaker in B than in Γ_{33} (compare Figure 3.4) but at the same time the background noise of B is correspondingly weaker than the background noise of Γ_{33} (compare Figure 3.7 and Figure 3.6). The performance of B and Γ_{33} are, therefore, supposed to be similar. Nevertheless, the instrument noise is assumed to have a standard deviation of $\sigma_B = 1\,\mathsf{nT}$ in the magnetic case and $\sigma_\Gamma = 3\,\mathsf{E}$ in the gravity gradient case (Table 3.1). This advantage of the magnetic field observation is mirrored in its outstanding performance at the $2\,\mathsf{m}$ depth. With larger depths though, the overall noise increases and this advantage diminishes. Tests have shown that an increase of the assumed magnetic instrument noise leads to a closer resemblance of the MF performance curves for B and Γ_{33}. A drastic decline in detection can be witnessed once the depth reaches $2\,\mathsf{m}$, which corresponds to the height, c, of the prism. Interestingly, the detections based on g_3 are able to catch up with those for the other data for depths of $3\,\mathsf{m}$ and below, where the decrease in successful detection of all four graphs slows down. When the depth, d, approaches infinity, the detection turns into the case where the sought signal does not exist in the observations. The maximum filter output, $y_{\max}$, will fall at a random position of the profile. The histogram of $y_{\max}$ locations of the Monte Carlo simulations with, for example Γ_{33}, is presented in Figure 3.20. The maximum output indicates a random position after each MF run. Each position is thereby hit between $0.4\,\%$ and $1.7\,\%$ of the 1000 filter runs. Ideally, each location would have been chosen $1\,\%$ of the times. Under the

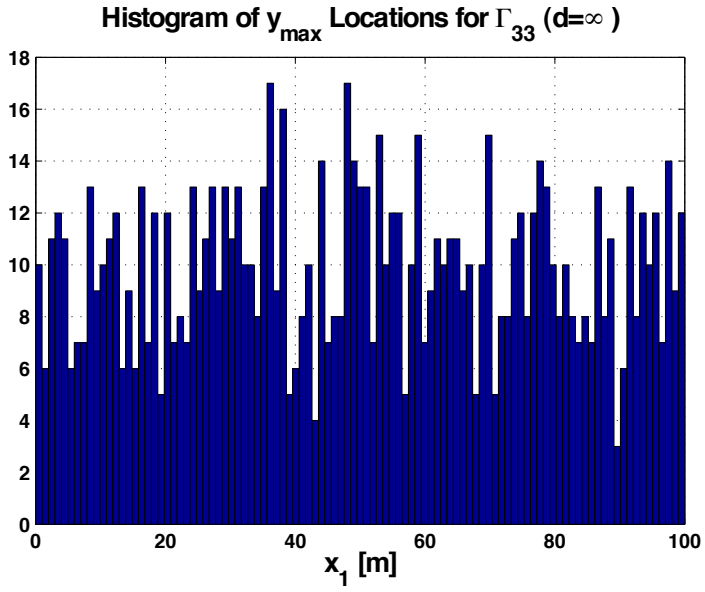

Figure 3.20: Filter Output Locations if Anomaly is at Infinite Depth

assumption that the conditions of Poisson's Relation are fulfilled (2.20), a preliminary conclusion can be drawn that the magnetic field data is the most successful in the very shallow subsurface (here, around 2 m depth), while gravity gradients show a similar performance. Gravity, however, seems to contribute more to the detection problem at slightly lower depths (> 3 m). The results in the 2 m case mainly depend on the differences in instrument noise. Simulations show that all three sensors will have a 100 % detection rate if the instrument noise is set to zero. For the 3 m case, however, the detection rate based on, g_3, Γ_{33}, and B, are without instrument noise 17.7 %, 21.2 %, and 23.2 %, respectively. These variations clearly do not depend on the instrument noise but are due to the specific signal and background noise properties and are similar to the variations in Table 3.2.

In order to better understand the characteristics of the different data types, the Signal-to-Instrument-Noise Ratio is determined by

$$\mathrm{SN}_{\mathrm{Instrument}}\mathrm{R} = \frac{\max \|\mathbf{s}(\mathbf{x})\|}{\sigma_{\mathrm{Instrument}}}. \tag{3.49}$$

It is defined as the extremum of the sought signal, s, divided by the standard deviation of the random instrument noise. The extrema are

$$\begin{aligned} \max \|g_3(\mathbf{x})\| &= 0.024 \text{ mgal} \\ \max \|\Gamma_{33}(\mathbf{x})\| &= 86.107 \text{ E} \\ \max \|B(\mathbf{x})\| &= 45.309 \text{ nT} \end{aligned} \tag{3.50}$$

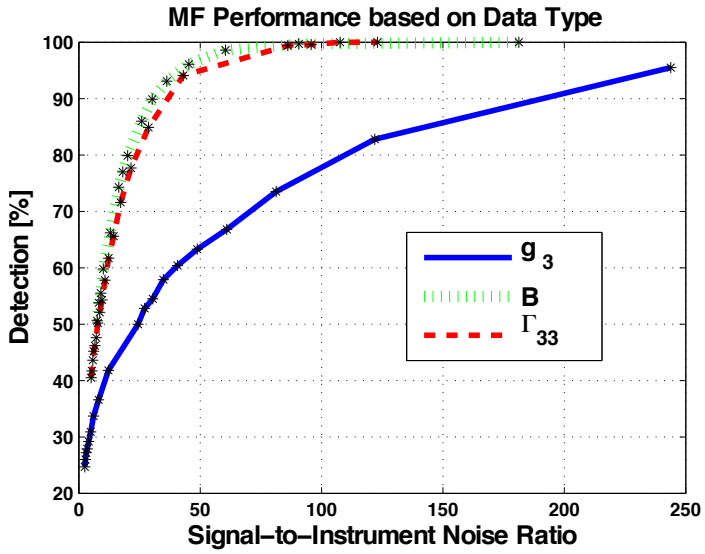

Figure 3.21: $\mathrm{SN}_{\mathrm{Instrument}}\mathrm{R}$ for a Prism at 2 m Depth

if the signal is generated by a prism at 2 m depth under the conditions specified in Section 3.1.1. With the typical standard deviations as previously introduced (Table 3.1), $\sigma_g = 0.01\,\mathsf{mgal}$, $\sigma_\Gamma = 3\,\mathsf{E}$, and $\sigma_B = 1\,\mathsf{nT}$, the $\mathrm{SN}_{\mathrm{Instrument}}\mathrm{R}$ values are expected to be

$$\begin{aligned} \mathrm{SN}_{\mathrm{Instrument}}\mathrm{R}^{(g_3)} &= 2.400 \\ \mathrm{SN}_{\mathrm{Instrument}}\mathrm{R}^{(\Gamma_{33})} &= 28.702 \\ \mathrm{SN}_{\mathrm{Instrument}}\mathrm{R}^{(B)} &= 45.309. \end{aligned} \tag{3.51}$$

Figure 3.21 plots the amount of successful detections with respect to various $\mathrm{SN}_{\mathrm{Instrument}}\mathrm{R}$ values. This underlines the above conclusion that the MF performance based on gravity data is less reliable than the MF performance based on the vertical gravity gradient or on the magnetic field data. One reason is the high instrument noise of the gravimeter relative to the quantity of the signal (3.51). In addition to that, the $\mathrm{SN}_{\mathrm{Instrument}}\mathrm{R}$ based on g_3 has to increase to 200 in order to reach 90 % success in detection. This is only a theoretical number, which will not be achieved in a real application (compare Section 2.2.1). However, the above analysis also demonstrates that even if the instrument noise is approaching zero, the gradiometer is still superior over the gravimeter. An explanation for that is the difference in their corresponding signal structure. The gradiometer components are more represented by the high frequencies and show a signal with sharp contours while the gravity signal is rather spread out and less distinct in comparison (Figure 3.3 and Figure 3.4).

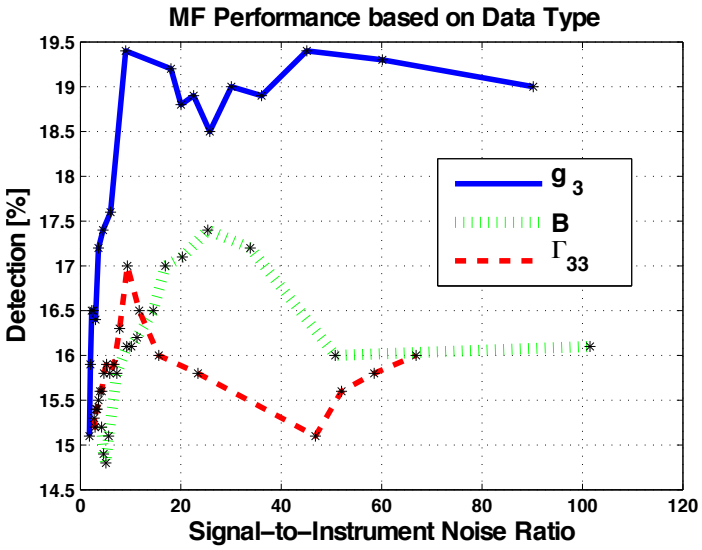

Figure 3.22: $\mathrm{SN}_{\mathrm{Instrument}}\mathrm{R}$ for a Prism at 3 m Depth

The same tests as above are also executed for the case where the prism is simulated at 3 m depth. The respective extrema of the sought signal are

$$\begin{aligned} \max \|g_3(\mathbf{x})\| &= 0.018 \text{ mgal} \\ \max \|\Gamma_{33}(\mathbf{x})\| &= 46.807 \text{ E} \\ \max \|B(\mathbf{x})\| &= 25.376 \text{ nT}. \end{aligned} \tag{3.52}$$

The resulting $\mathrm{SN}_{\mathrm{Instrument}}\mathrm{R}$ based on the typical standard deviations (Table 3.1) lead to

$$\begin{aligned} \mathrm{SN}_{\mathrm{Instrument}}\mathrm{R}^{(g_3)} &= 1.800 \\ \mathrm{SN}_{\mathrm{Instrument}}\mathrm{R}^{(\Gamma_{33})} &= 15.602 \\ \mathrm{SN}_{\mathrm{Instrument}}\mathrm{R}^{(B)} &= 25.376. \end{aligned} \tag{3.53}$$

As the greater depth decreases the signal strength of each data type, the $\mathrm{SN}_{\mathrm{Instrument}}\mathrm{R}$ decreases as well. Figure 3.22 plots the detection rate versus the $\mathrm{SN}_{\mathrm{Instrument}}\mathrm{R}$ based on a prism located at 3 m depth. Again, most of the assumed instrument noise values are just theoretical and do not occur in a real application but it is interesting to realize that a small decrease in the gravimeter instrument noise (equals a small increase of the low $\mathrm{SN}_{\mathrm{Instrument}}\mathrm{R}$) has a large effect on the MF performance. A decrease of the gradiometer or magnetometer instrument noise, on the other hand, hardly yields any improvement. However, it has to be noted that the success rate of the detection is low in general and that all three data types are relatively close to each other in contrast to the case of 2 m depth in Figure 3.21. Therefore, less emphasis should be put on

the differences in Figure 3.22. The above observations correspond to the conclusions from Figure 3.19 that the superiority of the magnetic field and the gravity gradients over gravity vanishes at larger depths.

3.3.2 Comparison of Various Data Combinations

So far, each type of observation has been tested individually. In the following, a MF is simulated with its input consisting of various types of data combinations. The setup is otherwise the same as described in Section 3.1 and simulated in Section 3.3.1. The outputs of several possible data combinations are summarized in Table 3.3. The columns are divided according to the different depths at which the prism is located ($2\,\mathsf{m} - 5\,\mathsf{m}$). For each depth and data combination, the percent of the successful detection out of 1000 runs, the square root of the maximum SNR (2.68) and the mean value of 1000 maximum filter outputs are presented. The combinations that simultaneously contain g_3 and B utilize a noise covariance matrix derived from the periodogram (Section 3.2.3), all other covariance matrices are directly derived from the covariance model [Jekeli, 2003b]. The variance of the instrument noise, ϕ_i, that is added to the background covariances (3.21), is identical for both cases.

The simulation results emphasize the advantage of data combinations as in most cases they significantly improve the results of the single data in Table 3.2. The combination (Γ_{33}, Γ_{31}), for instance, has around 10 % more successful detections than those gradients individually in the case where the anomaly is at $2\,\mathsf{m}$ depth. Adding the component Γ_{11} to the above combination will even further improve the detection with an additional 2.5 %. In comparison to that, the use of all six gravity gradient components, on the other hand, shows hardly any impact, as the gravity changes in x_2-direction are too small in this simulation setup. These simulation results match the beforehand expectations.

According to the simulations, adding gravity to the other data does not significantly improve the MF performance. Comparing Table 3.3 and Table 3.2, for example, shows that (g_3, Γ_{13}, Γ_{33}) yields results similar to (Γ_{13}, Γ_{33}). Adding g_3 to the observations might even lead to a small disadvantage as shown by the results of (g_3, Γ_{13}, Γ_{33}, B) and (Γ_{13}, Γ_{33}, B) in the case of $2\,\mathsf{m}$ depth.

Except for g_3, the simulations show that any other combination advances the MF detection. The more data components the better the performance. The overall shape of the performance curve is still the same as plotted in Figure 3.19. The combination of data will improve the detections but the drastic decline from an anomaly at $2\,\mathsf{m}$ depth to an anomaly at $3\,\mathsf{m}$ depth still exists. A further notable finding is that the detections are most successful in those cases where $\bar{y}_{\max}$ is close to the value of λ. This corresponds to the fact that the expectation of $y_{\max}$ equals λ if the sought signal exists (2.72).

Combination	2 m			3 m			4 m			5 m		
	%	λ	$\bar{y}_{\max}$	%	λ	$\bar{y}_{\max}$	%	λ	$\bar{y}_{\max}$	%	λ	$\bar{y}_{\max}$
$2\Gamma_{12}$, $\Gamma_{22}-\Gamma_{11}$	99.1	4.245	4.247	27.4	1.432	2.470	16.1	0.768	2.331	11.8	0.504	2.220
Γ_{33}, Γ_{13}	96.2	4.329	4.321	22.4	1.370	2.552	14.8	0.744	2.341	11.6	0.498	2.209
Γ_{11}, Γ_{33}, Γ_{13}	98.7	4.785	4.777	28.1	1.517	2.574	16.8	0.845	2.353	13.9	0.576	2.225
Γ_{11}, Γ_{12}, Γ_{13}, Γ_{22}, Γ_{23}, Γ_{33}	98.9	4.851	4.845	29.9	1.540	2.574	16.7	0.852	2.354	13.7	0.579	2.230
g_3, Γ_{13}	88.1	3.777	3.825	19.0	1.198	2.543	12.6	0.632	2.371	10.8	0.421	2.239
g_3, Γ_{33}, Γ_{13}	96.3	4.329	4.322	22.5	1.370	2.552	14.9	0.744	2.342	11.8	0.498	2.209
g_3, B	96.7	4.448	4.480	18.1	1.208	2.557	12.8	0.628	2.358	9.7	0.428	2.207
g_3, Γ_{33}, B	99.1	4.787	4.804	21.9	1.360	2.550	14.3	0.724	2.343	10.9	0.498	2.209
g_3, Γ_{13}, B	98.5	4.831	4.845	22.7	1.402	2.571	14.1	0.748	2.350	11.7	0.500	2.214
Γ_{13}, B	98.5	4.831	4.845	22.8	1.402	2.571	13.9	0.748	2.350	11.9	0.500	2.214
Γ_{33}, Γ_{13}, B	99.7	5.012	5.019	23.5	1.419	2.567	14.0	0.752	2.347	11.1	0.501	2.214
g_3, Γ_{33}, Γ_{13}, B	98.5	4.851	4.845	23.4	1.419	2.568	14.1	0.753	2.348	11.0	0.502	2.215
g_3, Γ_{11}, Γ_{33}, Γ_{13}, B	98.3	5.317	5.330	25.5	1.557	2.811	17.4	0.853	2.463	14.1	0.579	2.266

Table 3.3: MF Simulations with Respect to Depth of Anomaly

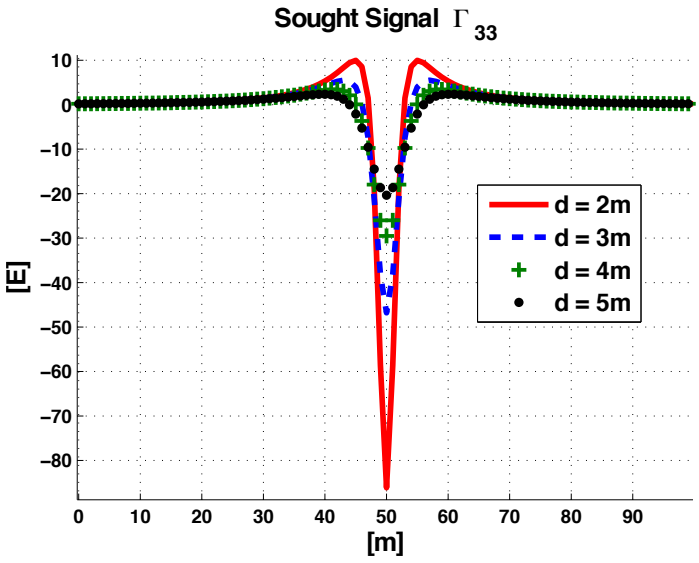

Figure 3.23: Signal Strength Depending on Depth

3.3.3 Estimation of Depth

The MF technique is in general used to locate an anomaly in a plane or along a profile. This section analyzes whether it is also possible to extract some information about the depth, d, of the anomaly. The depth is not treated as an unknown parameter but as a characteristic of the sought signal (Section 3.1.1). Alternatively, it could also be seen as a characteristic of the background noise magnitude. Since it is required for the MF to model the sought signal, the depth of the anomaly must be known or estimated a priori. While the size of the simulated prism (a, b, c) determines the shape of the sought signal, the estimated depth of the prism defines the amplitude of the sought signal: the shallower the location of the anomaly the stronger the signal. The putative signal, for example, for Γ_{33} is plotted in Figure 3.23, representing the different cases of d. If the actual anomaly depth in the observation is unknown, the modeled depth in the filter function may be wrong. Figure 3.24 presents the results for four different cases where the actual anomaly is at $2\,\mathsf{m}$, $2.5\,\mathsf{m}$, $3\,\mathsf{m}$, and $3.5\,\mathsf{m}$, respectively. The data consist of Γ_{13} only. The abscissa indicates the anomaly depth that is modeled for the sought signal. The ordinate refers to the successful detection out of 1000 simulations. Hence, the circle tags the cases where assumed and actual depth fall together. The MF performance is clearly sensitive to the assumed depth and is most successful if the correct depth is assumed. However, this property vanishes with larger depths ($3.5\,\mathsf{m}$). In any case, making the modeled signal stronger (shallower depth) than the actual observed signal diminishes the success rate of locating the anomaly.

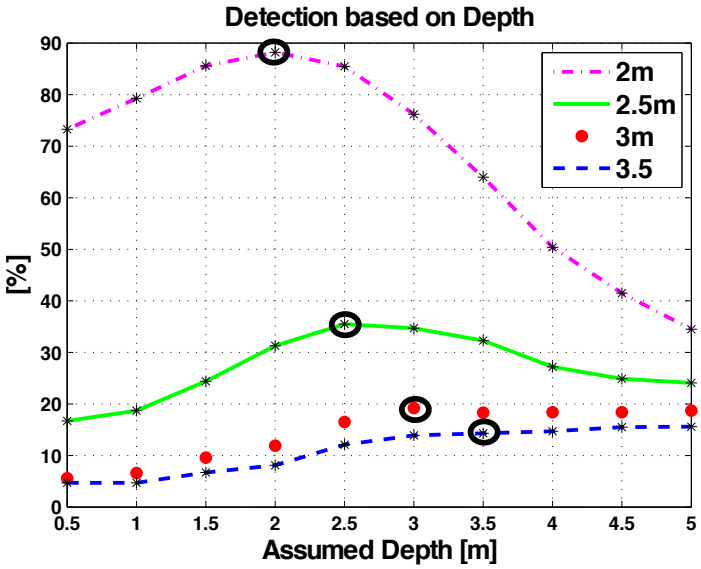

Figure 3.24: MF Performance under Assumed Depths for Γ_{13}

A further conclusion is that the maximum of the graph is not very sharp. The MF performance based on 0.5 m more or less than the actual depth is still very close to the results produced by the correct depth. This is an important conclusion for a practical application. Under similar circumstances (size of anomaly, noise level of background field), the depth of the anomaly should ideally be known or estimated within 0.5 m.

Figure 3.25 plots the mean value of the maximum filter outputs of the 1000 simulations against the assumed depths. Those are the corresponding graphs to the detections in Figure 3.24. The symbol [-] indicates that the values are unitless. Similarly, the maximum of each graph corresponds to the correctly assumed depth (circled), except for the case of $d = 3.5$ m. In a real world application, the MF can be run several times, where each time the modeled signal assumes a different anomaly depth. The maximum of all the maximum filter outputs,

$$\underset{\max}{\underbrace{y}} = \max\left(y_{\max}^{\text{Assumed Depth}}\right), \tag{3.54}$$

is most likely the one based on the correct anomaly depth, also assuming that the maximum filter output is most likely at the location of the sought signal. However, it has to be taken into account that the results in Figure 3.24 refer to the mean of 1000 detections per depth, while in real life there is, of course, only a single field. The standard deviation for the 1000 $y_{\max}$ at each of the assumed depths is around 0.8. This is relatively high considering that all the $y_{\max}$ in Figure 3.25 lie in the range from 2 to 4. However, this is to be expected since the standard deviation of the filter

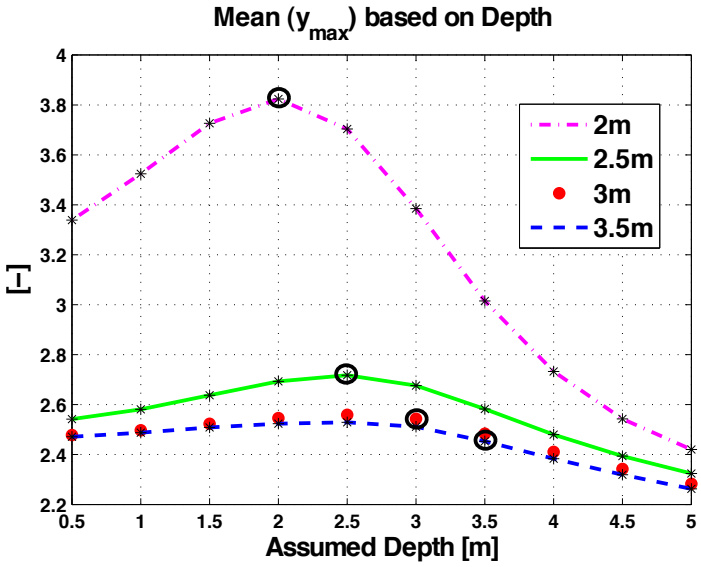

Figure 3.25: Mean of the Maximum Filter Output under Assumed Depths for Γ_{13}

output, y, is one (2.71). In order to underline these studies, the same tests are carried out for the Γ_{33} gradient component leading to very similar results.

The purpose of the next MF simulations is to have a more detailed look at the individual fields to be closer to a real world situation where $y_{\max}$ is not averaged. Figure 3.26 a), for example, is based on a mass anomaly located at 2 m depth while the assumed depth ranges from 0.5 m to 5 m. The maximum of those ten $y_{\max}$ values, namely $\underset{\cdots}{y}_{\max}$ (3.54), is determined. Figure 3.26 a) shows a histogram of the $\underset{\cdots}{y}_{\max}$ based on 1000 different background fields. In 32.9 % of the cases, $\underset{\cdots}{y}_{\max}$ occurs at an assumed depth of 2 m, which coincides with the simulated actual depth. If a deviation of 0.5 m is accepted the results at 1.5 m and 2.5 m depths are included and the percentage increases to 77.2 %. That means in 77.2 % of the 1000 cases $\underset{\cdots}{y}_{\max}$ appears where the assumed depth is correct or only 0.5 m off. Figure 3.26 b) through d) represent the corresponding histograms based on the actual depths of 2.5 m, 3 m, and 3.5 m, respectively. Figure 3.26 b) through d) reveal a high accumulation of $\underset{\cdots}{y}_{\max}$ at the assumed depths of 0.5 m and 2.5 m, which is unexpected for Figure 3.26 c) and d), where the simulated prism is located at 3 m and 3.5 m, respectively. However, those solutions might not necessarily be successful in the detection of the mass anomaly. For that reason, all unsuccessful detections (x_1 outside the range of $x_1 = 30\,\text{m} \pm 2\,\text{m}$) are removed from the data set. The remaining maxima of $y_{\max}$, i.e. the updated $\underset{\cdots}{y}_{\max}$, are presented in the updated histograms (Figure 3.27). Obviously, the deeper

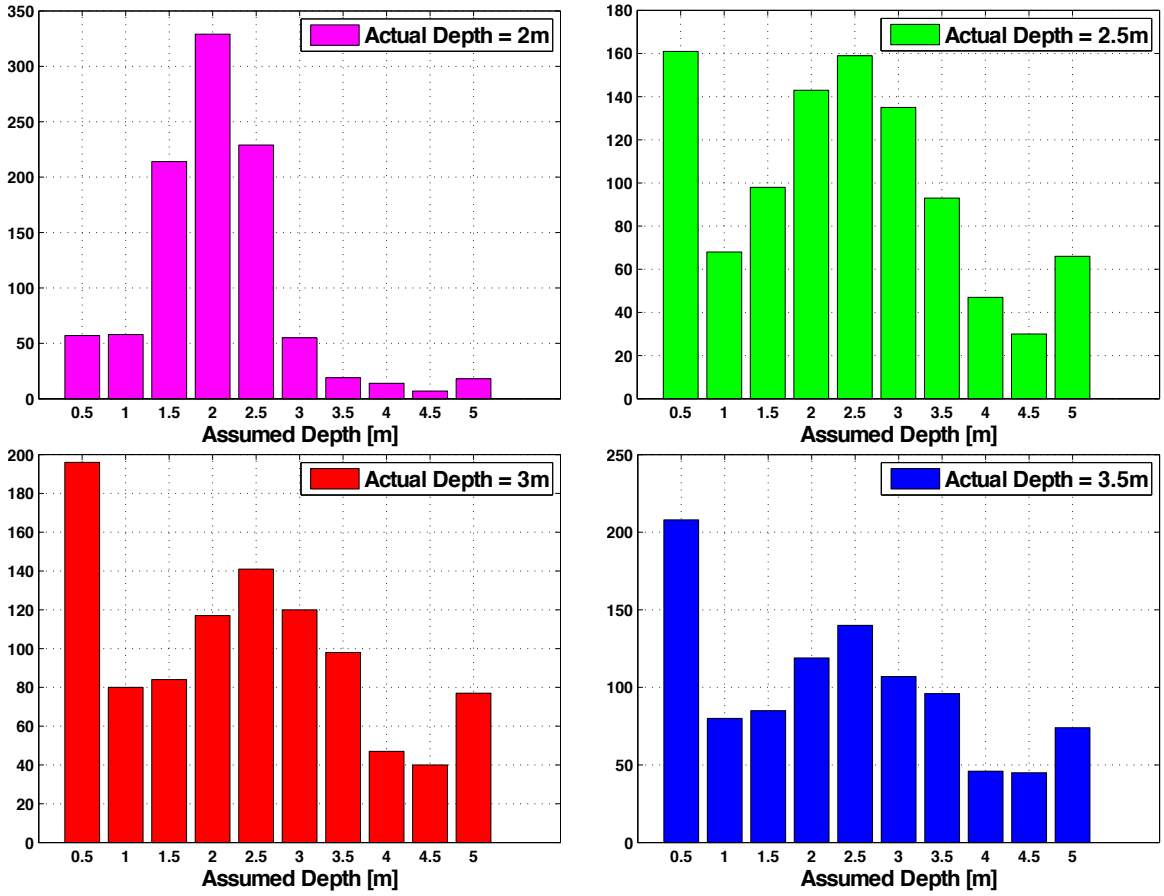

Figure 3.26: Detection Histogram of $\underset{\cdots}{y}_{\max}$ based on Γ_{13} and Depth of a) 2 m b) 2.5 m c) 3 m d) 3.5 m

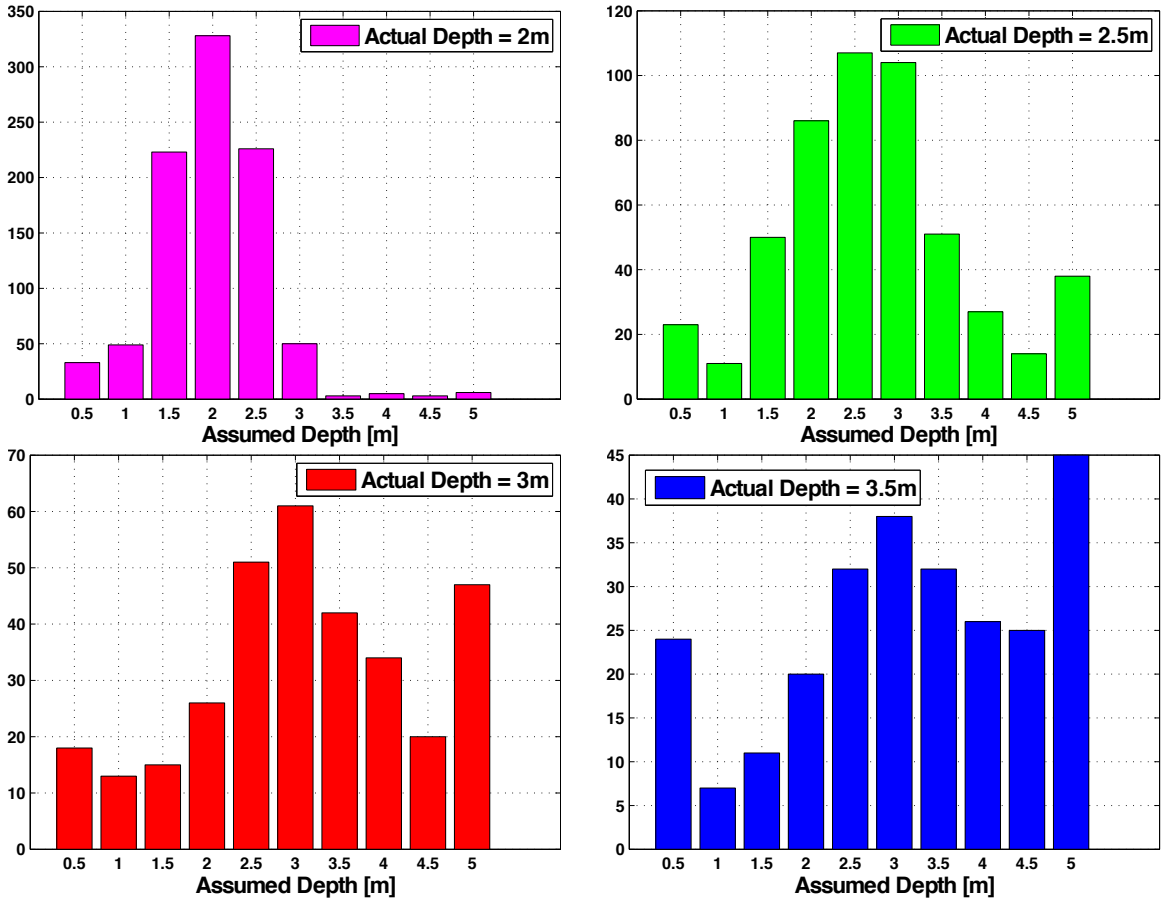

Figure 3.27: Successful Detection Histogram of $\underset{\cdots}{y}_{\max}$ based on Γ_{13} based on Γ_{13} and Depth of a) 2 m b) 2.5 m c) 3 m d) 3.5 m

the actual depth, the lower the number of correct detections but in addition to that, the remaining data show a clear accumulation at the correctly assumed depth. One exception is Figure 3.27 d), which similar to Figure 3.24 does not have a maximum at $d = 3.5\,\mathsf{m}$. A possible explanation is the strength of the background signal compared to the decreasing strength of the sought signal generated by the mass anomaly. It is interesting to notice that $\underset{\cdots}{y}_{\max}$ also accumulates at the assumed depth of $5\,\mathsf{m}$ when the actual depth is deep. This finding, however, cannot be observed in the curves based on the overall mean of $y_{\max}$ in Figure 3.25. Observing the same profile several times or including multiple parallel profiles might, therefore, eliminate this edge effect in practice.

This section has shown that, although the implemented MF is only two-dimensional, its performance is clearly sensitive to the estimated depth in the sought signal. It seems, therefore, to be possible to develop a reasonable algorithm that estimates the depth of the anomaly. A possible scenario in a real world application could be, for example, to run the MF with various assumed depths and to determine the most likely horizontal position of the void, i.e. its x_1-coordinate, based on those MF results. The filter outputs assumed to be false can be deleted from the computed solutions and the corresponding assumed depths are ruled out. The maximum of the remaining maximum filter outputs is the updated $\underset{\cdots}{y}_{\max}$ and is likely an indicator of the correct depth (here up to $0.5\,\mathsf{m}$). This method becomes less applicable if the signal strength decreases (increase in depth) with respect to the strength of the background noise. Taking several measurements of the same or parallel profiles and averaging their $y_{\max}$, might make this method more stable though. The simulation in Figure 3.24 can almost be reproduced by averaging as little as 10 filter outputs.

The MF performance is clearly linked to the $y_{\max}$ parameter. It does not only help to estimate the depth of the mass anomaly but it also provides a test quantity for the statistical interpretation of the suggested horizontal solution. Knowing the quality of the localization will help to rule out the possible false detections at various assumed depths. The statistical details are presented in Chapter 4.

3.3.4 Non-Stationarity and Anisotropy in the Background

The covariance model applied in the MF assumes that the background noise is a stationary process. Furthermore, the covariances for the disturbing potential, ϕ_T, and the covariances for its radial derivatives, ϕ_{g_3} and $\phi_{\Gamma_{33}}$, as well as their cross-covariances are isotropic. The following study intends to answer the question if the applied MF method is still valid in case that stationarity and isotropy are not guaranteed.

The standard MF procedure is applied to the different data types: g_3, Γ_{33}, Γ_{13}, B. Four different cases are compared to the standard MF simulation. In the first case, a positive linear trend along the x_1-direction is added to the noise, n, generated by the background. The minimum and maximum value of the trend is defined by

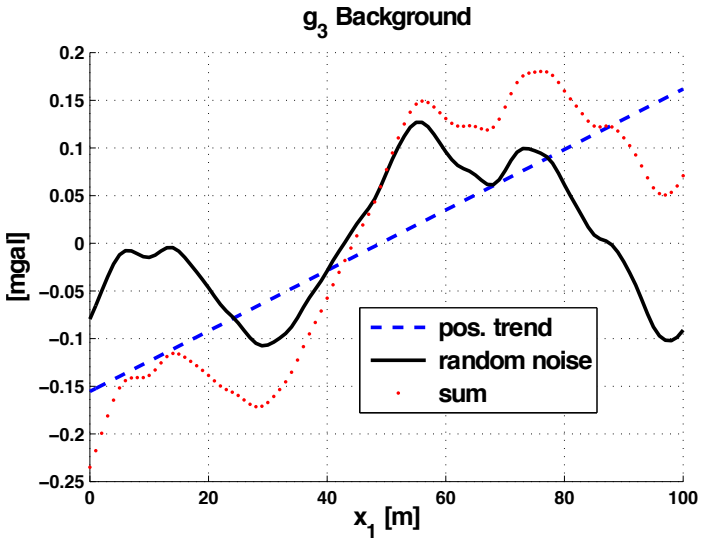

Figure 3.28: Positive Trend in the g_3 Background

the minimum and maximum of the simulated background field. As a result, the trend varies for each field. One example for a trend added to the random noise of a gravity field is shown in the Figure 3.28. In the second case, the trend is reversed and becomes negative along the x_1-direction. In the third and fourth case, an anomaly is added or subtracted to the background, respectively. The anomaly is computed by the following equations:

$$A = \max(n) \tag{3.55}$$

$$\begin{aligned} \sigma_{x_1} &= 40 \\ \sigma_{x_2} &= 20 \end{aligned} \tag{3.56}$$

$$\Theta = \frac{\pi}{6} \tag{3.57}$$

$$\tilde{a} = \frac{\cos^2\Theta}{2\sigma_{x_1}^2} + \frac{\sin^2\Theta}{2\sigma_{x_2}^2} \tag{3.58}$$

$$\tilde{b} = \frac{-\sin 2\Theta}{4\sigma_{x_1}^2} + \frac{\sin 2\Theta}{4\sigma_{x_2}^2} \tag{3.59}$$

$$\tilde{c} = \frac{\sin^2\Theta}{2\sigma_{x_1}^2} + \frac{\cos^2\Theta}{2\sigma_{x_2}^2} \tag{3.60}$$

$$\begin{aligned} x_0 &= \frac{N_1}{2} + 10 \\ y_0 &= \frac{N_2}{2} - 5 \end{aligned} \tag{3.61}$$

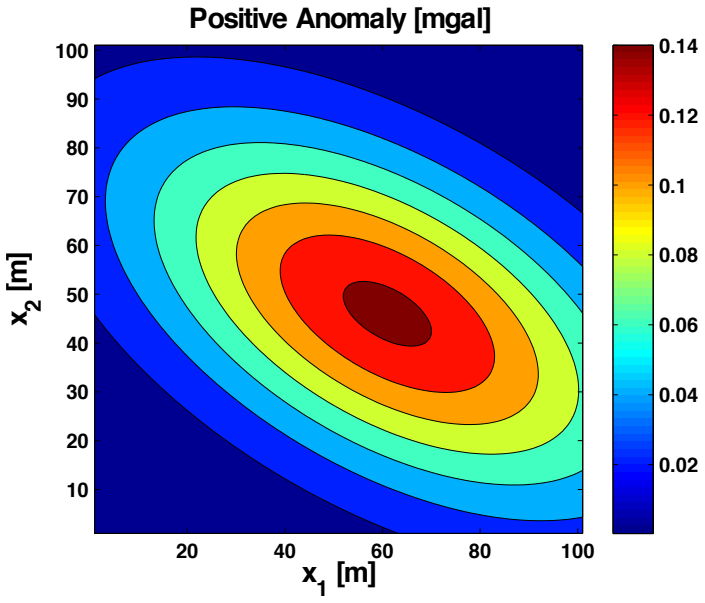

Figure 3.29: Positive Anomaly in the g_3 Background Field

$$\begin{aligned} x_1 &= 0, \ \ldots, \ (N_1 - 1) \\ x_2 &= 0, \ \ldots, \ (N_2 - 1) \end{aligned} \tag{3.62}$$

$$\begin{aligned} n_{\text{Anomaly}} &= A \cdot e^{-L} \\ L &= \tilde{a}\,(x_1 - x_0)^2 + 2\tilde{b}\,(x_1 - x_0)\,(x_2 - y_0) + \tilde{c}\,(x_2 - y_0)^2\,, \end{aligned} \tag{3.63}$$

where the magnitude of the anomaly depends on the maximum value of the particular background field. One example for an anomaly in a gravity field is presented in Figure 3.29. The horizontal profile at $x_2 = 37\,\mathsf{m}$ is extracted and added to the random observation noise (Figure 3.30). Figure 3.31 compares the MF output based on g_3 in the standard case to the case where a positive trend has been introduced to the background noise. While the standard case correctly detects the sought signal (maximum output at $x_1 = 30\,\mathsf{m}$), the positive trend causes a large maximum in the MF output at the beginning of the profile and a corresponding minimum at the end of the profile. This can be explained by the fact that the sought signal is a negative lobe (gravity above a void) and that the trend leads to an increase of numbers towards the end of the observation profile. The positions for maximum and minimum MF output are reversed if the negative trend is added instead. This can again be explained by the corresponding fact that the negative trend generates higher values at the beginning of the profile. The same effects but even more distinct are identified by the simulations utilizing Γ_{33} as shown in Figure 3.32. The positive trend applied to Γ_{13} and B data sets are presented in Figure 3.33. The MF output contains one dominant global

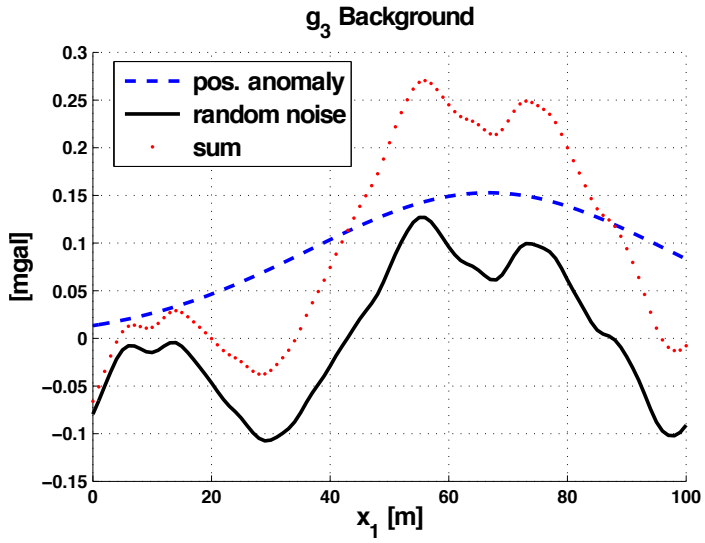

Figure 3.30: Positive Anomaly in the g_3 Background Profile

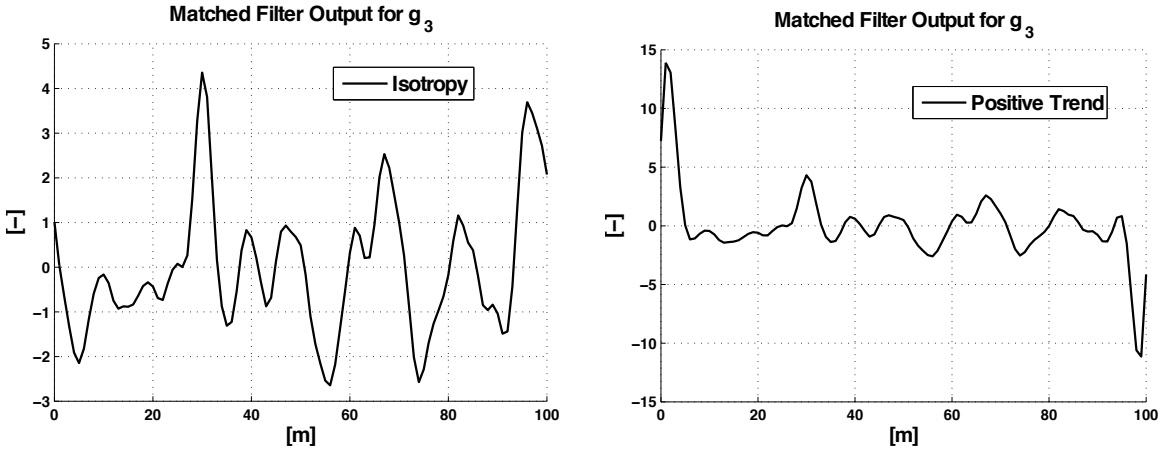

Figure 3.31: g_3 Background for a) Isotropy b) Positive Trend

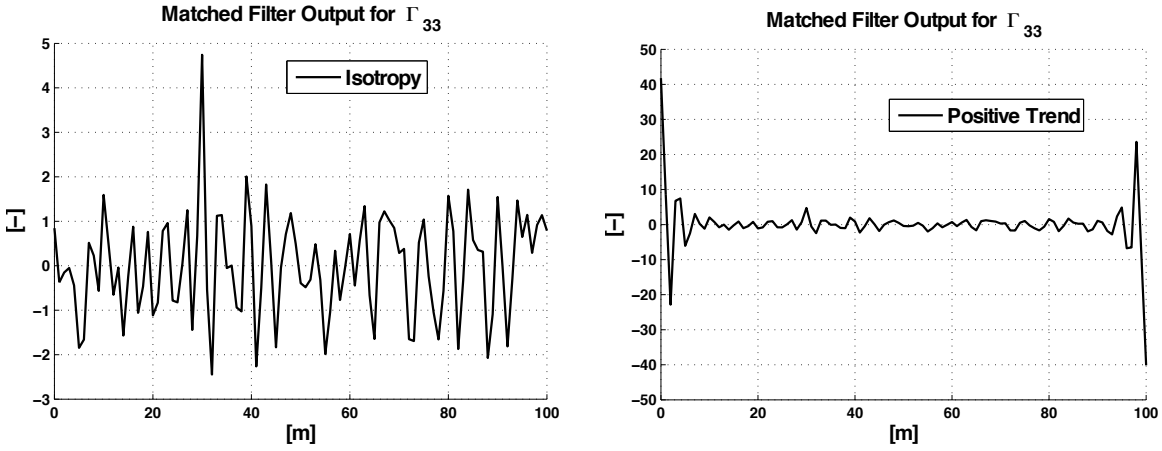

Figure 3.32: Γ_{33} Background for a) Isotropy b) Positive Trend

maximum at the beginning of the profile in case of Γ_{13}, and one dominant global minimum at the end of the profile in case of B. Beside this, the two side-lobes of the overall maximum/minimum still overpower the maximum caused by the sought signal in both cases. The effects of an anisotropic background field as generated by the introduced positive or negative anomaly (Figure 3.34) are similar to the effects caused by the positive or negative trend. However, as it is to be expected, the effects are not as strong. All four cases of different background noise reveal that the introduction of a trend or an additional anomaly cause undesired maxima at the edges of the MF output profile as the overall trend of the added noise interferes with the shape of the sought anomaly. In order to avoid those false detection results, the edges of the output can be omitted when selecting the maximum. This requires that the sought signal does not occur at the edge of the profile. Tests based on 1000 simulated data sets suggest to cut off about 10 % (ten points) on either side of the MF output to avoid these edge effects. If the background noise contains a positive or negative trend, the MF is unable to detect the sought signal because the maximum filter output is always at the edge of the profile. If the values at those edges of the filter output are set to zero, the MF results resemble the results of the standard stationary case. As observed above, the introduced anomaly in the background triggers similar effects as the introduced trend. In the same way, the detection problems can be avoided by setting the edges of y to zero. In contrast to the trend, the anomaly still allows for a few correct detections out of 1000 simulations even if the edges are not set to zero. The success rate of the standard stationary case slightly increases by setting the edges to zero, which is obvious as the number of possible wrong locations (the sought signal is at $x_1 = 30\,\mathsf{m}$) is reduced. This seems to be the only reason for the increase in success of the detection as the improvement is only marginal. It can, therefore, be

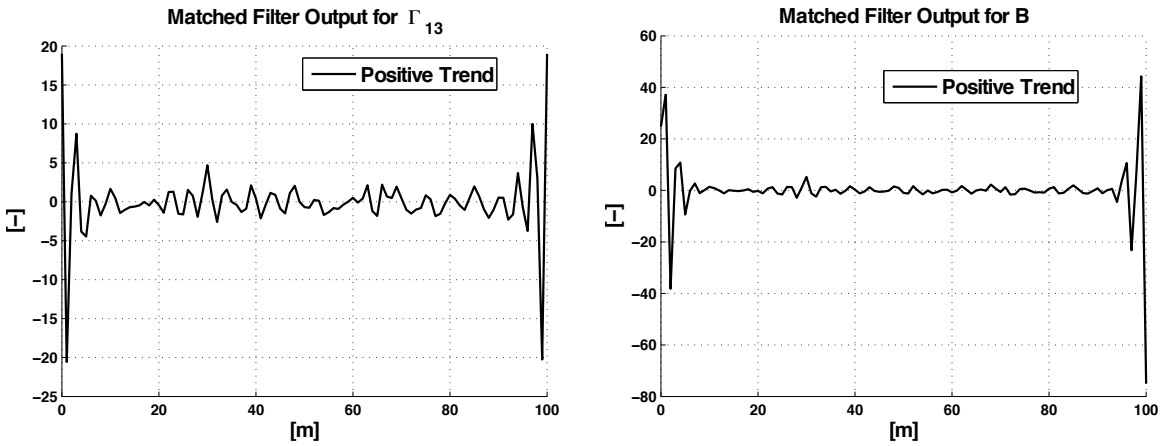

Figure 3.33: Positive Trend in the Background for a) Γ_{13} b) B

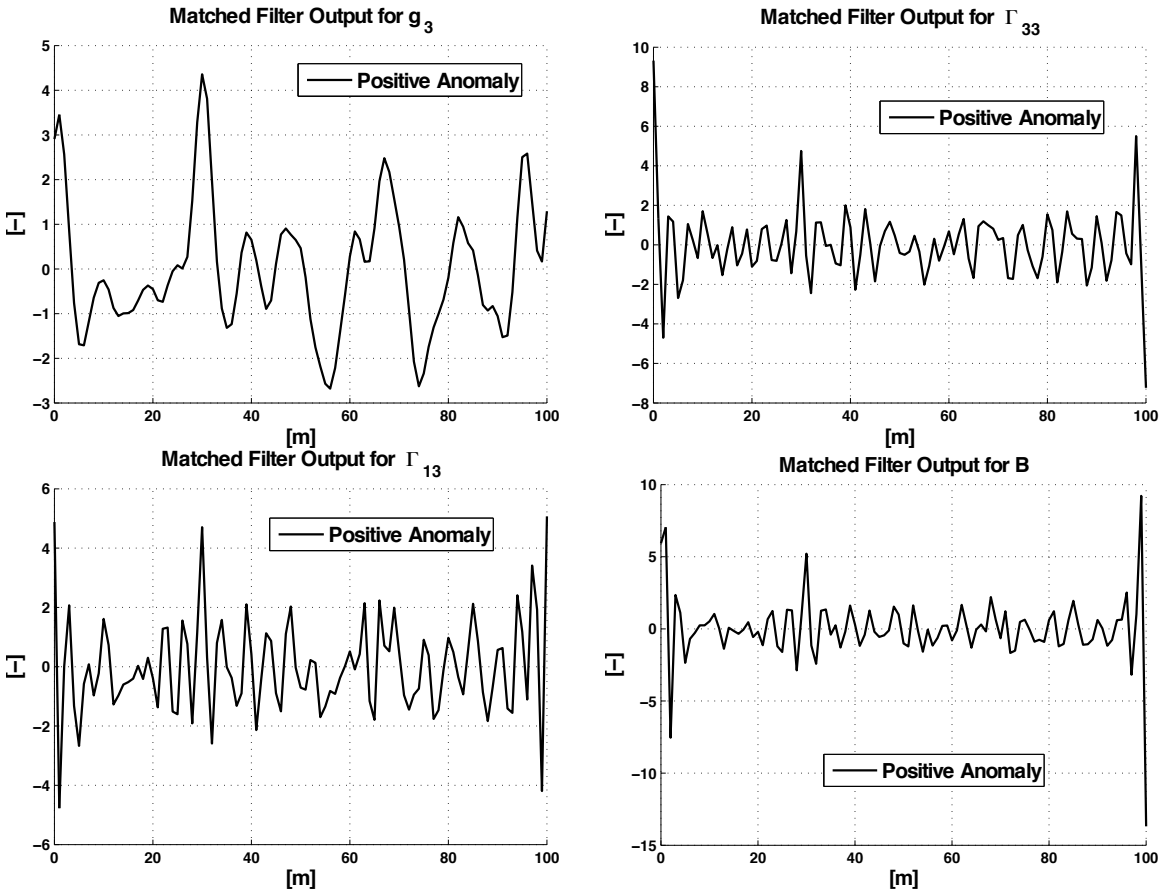

Figure 3.34: Positive Anomaly in the Background for a) g_3 b) Γ_{33} c) Γ_{13} d) B

concluded that a stationary background field does not lead to edge effects in the MF output as generated by the trend or anomaly.

The described edge effects are the only problems that arise due to the additional noise (trend or anisotropic anomaly) and can easily be overcome. For that reason, it is justified to continue with the introduced covariance model although it is only designed for stationary data.

3.3.5 Sensitivity to Covariance Model

Up to this section, all MF results are derived from simulations of the background field, which is based on the same model as the covariances. In order to verify the validity of the utilized covariance model, the background field in this section is taken from a set of real field measurements.

In July 2008, Bell Geospace Inc. (BGI) observed the Vinton Dome area to test their three-dimensional Full Tensor Gravity Gradiometry (FTG) platform in an airborne mission [BGI, 2008]. The Vinton Dome is located in southwestern Louisiana near the Texas border. The survey area covers approximately $196.2\,\mathsf{km}^2$ and lies between latitudes 30.07° and 30.23° North and longitudes 93.66° and 93.53° West. Figure 3.35 plots the survey lines, which were flown in North-South direction, and several perpendicular to that. The survey lines are about $250\,\mathsf{m}$ apart from each other. This data set is now used to simulate the background field in the current MF simulations. In contrast to local measurements on the ground, the airborne survey is more challenging. The position, orientation, and speed of the aircraft have to be determined and aligned via time stamps with the actual gravity gradient measurements. Further steps are the downward continuation of the signal to the ground, the terrain correction, and the correction for the gravity gradients generated by the aircraft and instrument platform. The Vinton Dome data set provided by BGI is already preprocessed, i.e. leveled, de-noised, and corrected for topography. More details about the applied corrections can be found in [BGI, 2008]. Despite the extra challenges, airborne gravity gradiometry has the advantage to cover a large area in a short time span. Since the signal strength and the resolution in airborne gradiometry is lower than in a local application, this method is designed to find larger mass anomalies than the prism described in Section 3.1.1. The usage of either airborne or ground gradiometry is a question of the scale the application requires. For that reason, the analysis of the Vinton Dome data set will also hold for the local MF case as the computational difference is represented by only a scale factor.

The free air Γ_{33} of the data set is mapped in Figure 3.36, where the center of the map clearly marks the outline of the Vinton Dome. The profile L881 is the profile with North-South expansion that is furthest east in the observed area. It can be treated as a real example of an observed gravity gradient field without the influence

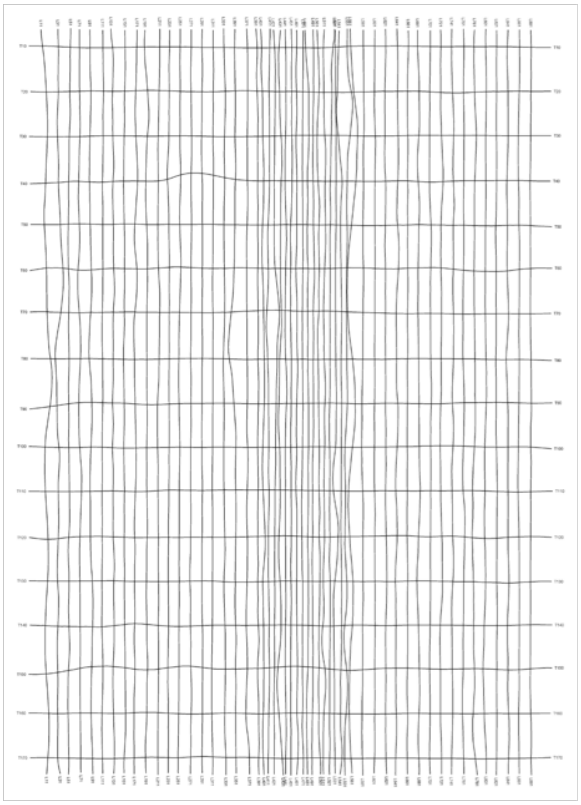

Source: BGI

Figure 3.35: Vinton Dome Flight Tracks

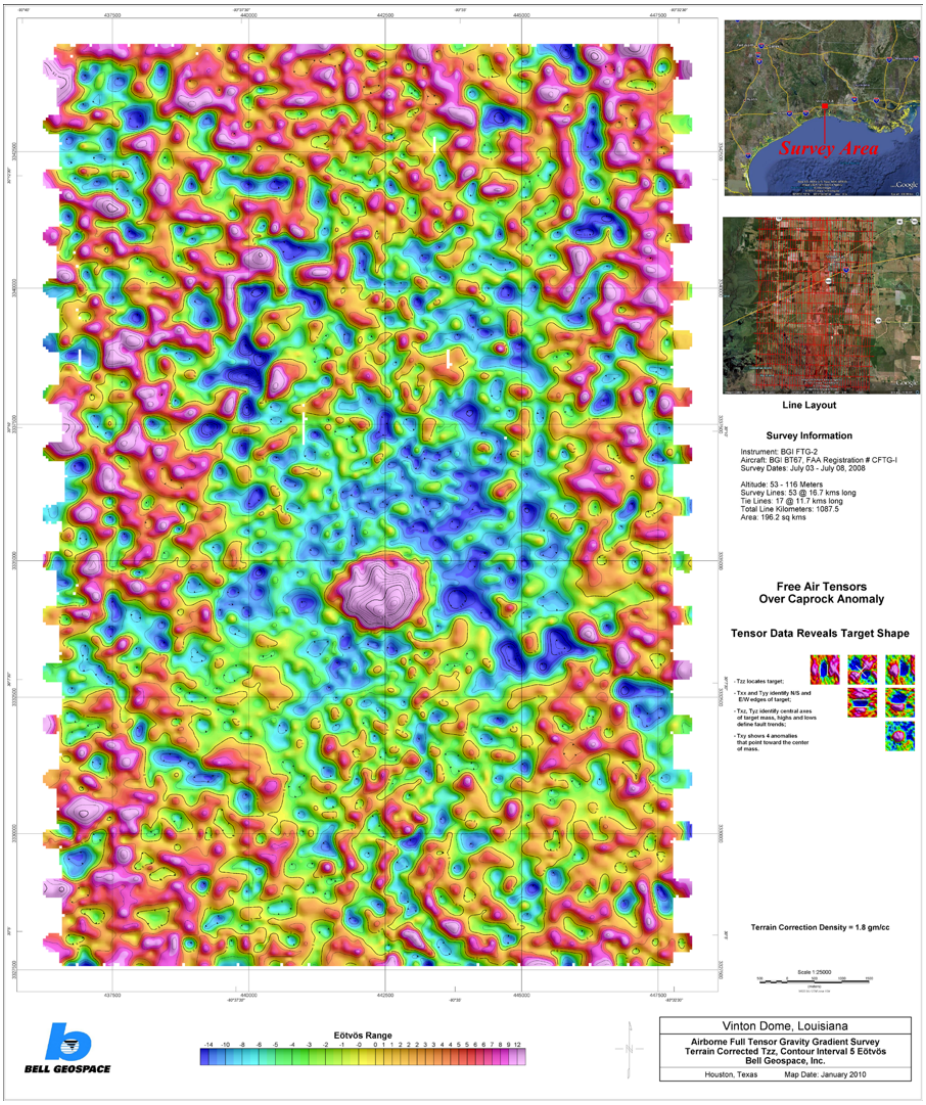

Source: BGI

Figure 3.36: Vinton Dome Free Air Γ_{33}

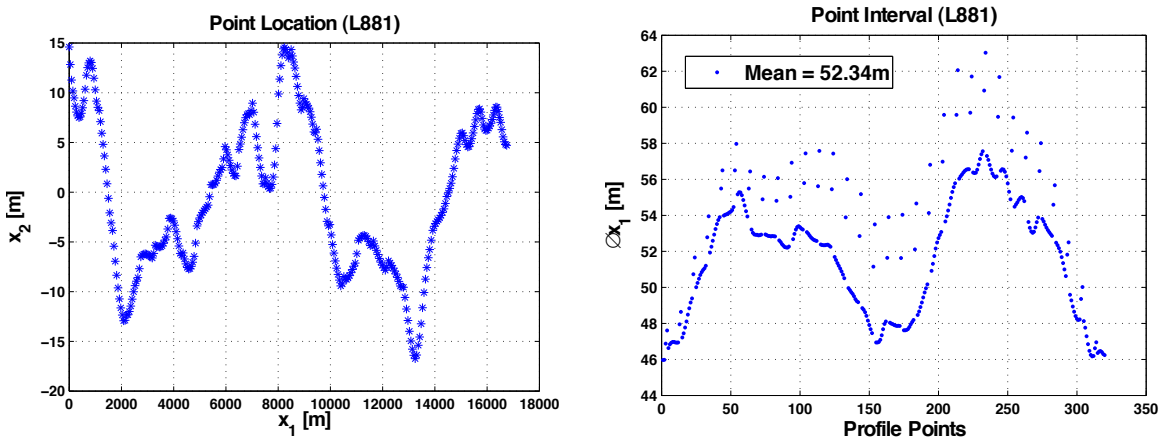

Figure 3.37: Vinton Dome a) Horizontal Coordinates b) Profile Point Interval

of a distinctive mass anomaly such as the dome, which lies only in the center of the observed area.

Figure 3.37 a) shows the horizontal coordinates of the observed L881 profile points (reduced to the coordinates of the first point). The North-South direction is declared as x_1. The profile length is about 17 km and points deviate from a straight profile line by no more than 20 m (in x_2). Figure 3.37 b) presents the interval in meters between the 321 points of the profile. Two consecutive points are between 46 m and 64 m apart along the profile direction. The average point interval is 52.34 m.

For practical reasons, it is assumed that all points are located on a straight profile ($x_2 = 0\,\mathsf{m}$), at constant height ($x_3 = 0\,\mathsf{m}$), and with a constant point interval ($\Delta x_1 = 52.34\,\mathsf{m}$). The data set provides measurements of all gravity gradients. However, only the gravity gradient component Γ_{33} will be discussed here and is plotted in Figure 3.38. In order to adjust the MF simulations to the Vinton Dome example, the dimensions of the prism that generates the sought signal is modified to $a = 10\,\mathsf{m}$, $b = 10000\,\mathsf{m}$, and $c = 4\,\mathsf{m}$. The center of the prism is now located at $x_{m_1} = 100 \cdot \Delta x_1 = 5234\,\mathsf{m}$ and the depth to the top of the prism is $d = 22\,\mathsf{m}$. The altitude of the airborne data is thereby neglected and assumed to be zero. The large depth of the simulated prism is chosen to decrease the signal strength of the sought signal since the signal strength of the background field is comparatively low. An alternative simulation would be, for example, to decrease the width of the prism, a, however, this might get too small for the resolution of the observed profile. The density contrast of the prism is here $\Delta\rho = -1.8\,\mathsf{g/cm^3}$ as this magnitude was also used in the terrain correction of the Vinton Dome data file.

The sought signal in [E] is generated and added to the observed profile L881 resulting in the observation vector in [E] of the MF simulation plotted in Figure 3.39.

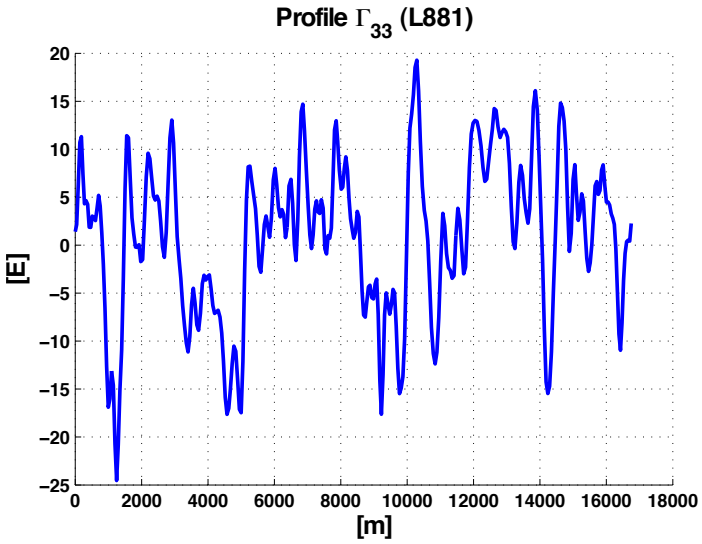

Figure 3.38: Γ_{33} of Vinton Dome Profile L881

The resulting MF output is unitless $[-]$ and multiplied by 50 for visual reasons, clearly locates the mass anomaly of the prism by $y_{\max}$ at 5234 m. However, the local maxima at 1361 m is almost of the same size as $y_{\max}$. This shows that the MF detection in this example is successful but also very fragile. The slightest decrease of the sought signal strength might lead to a higher output at the local background anomaly than at the location of the sought signal. A further indication for the vulnerability of this particular example is the low $\lambda = 0.195$. The above MF computation contains the covariance matrix (3.21) as described in Section 3.2. The matrix of instrument noise variances, Φ_i, is for now identical to that used in the previous simulations. The horizontal coordinate differences (3.17) that enter the covariance function for the matrix of the background noise, Φ_{bg}, are in this case computed by assuming a constant point interval of $\Delta x_1 = 52.34\,\mathsf{m}$. For the gravity gradient component Γ_{33}, the covariance function is described by the variance $\mathrm{Var} = \phi(0) = 8879.7\,\mathsf{E}^2$ and the correlation length $\mathrm{CL} = 13.2\,\mathsf{m}$. The correlation length as it is defined in [Moritz, 1989, p.174] determines the distance between two points for which the covariance has decreased to half the value of its variance:

$$\phi(\mathrm{CL}) = \frac{1}{2}\phi(0)\,. \tag{3.64}$$

Simulations show that the MF performance can be improved drastically when modifying the covariance function while the sought signal and observation vector remain the same as above. Increasing the correlation length from 13.2 m to 690.5 m under the same variance leads to a more distinct MF output (Figure 3.40). The filter output

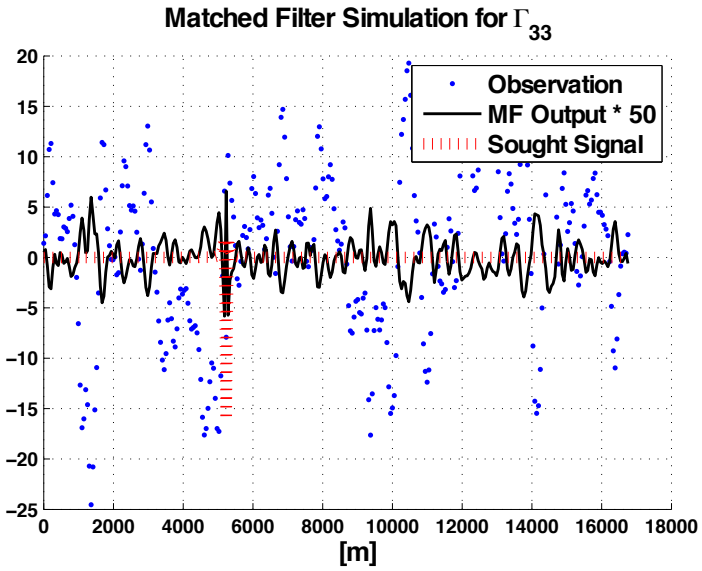

Figure 3.39: MF Simulation of Vinton Dome Profile L881

is still multiplied by 50 just to be consistent with the filter output in Figure 3.39. The increase of the CL interprets data to be higher correlated to each other, which in this particular case corresponds to the assumption that the point interval is only $\Delta x_1 = 1\,\mathsf{m}$. The result is an increase of λ from 0.195 to 4.01.

In order to better understand the covariance model, the empirical covariances are derived from the L881 observations. The gravity gradients of two points, x_i and y_i, with the same distance, l, to each other (within a precision of Δx_1) are grouped together and their corresponding empirical covariance is estimated by

$$\phi_{x,y}(l) = \left\{ \frac{1}{N} \sum_{i=1}^{N} (x_i - \mu)(y_i - \mu) \right\}_l \tag{3.65}$$

where N is the number of point combinations within a group of same (similar) l and μ is the mean value of the entire profile. Obviously, the longer the distance, the fewer samples there are to contribute to the estimate of the covariance. Figure 3.41 plots the empirical covariances over l. The covariances are cut off after approximately $l = 2000\,\mathsf{m}$, while the covariance function crosses zero at around $l = 1000\,\mathsf{m}$. The variance is $67.6\,\mathsf{E}^2$ with $\mathrm{CL} = 209.5\,\mathsf{m}$.

Figure 3.42 finally compares the empirical covariances, the analytic covariances, and the analytic covariances stretched to a $\mathrm{CL} = 690.5\,\mathsf{m}$. The empirical covariances do not match to the model unless they are multiplied by 100, which alters the scale. The overall MF performance should not be affected. Minor differences can occur

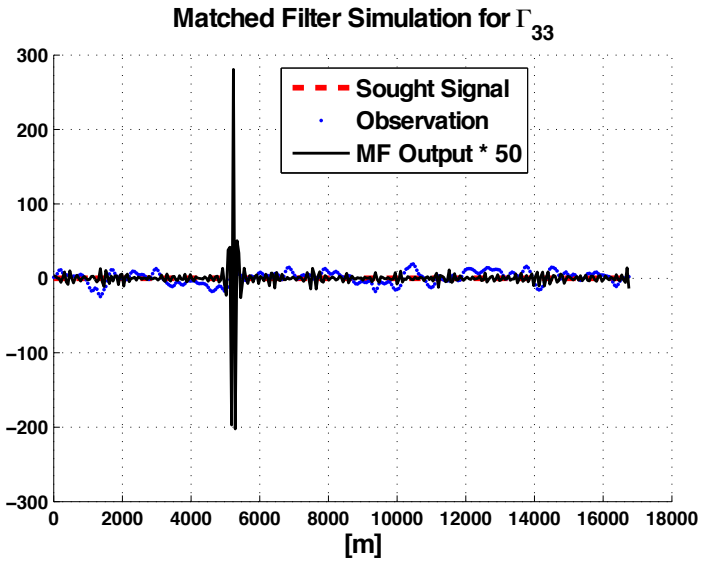

Figure 3.40: MF Simulation of Vinton Dome Profile L881 with CL = 690.5 m

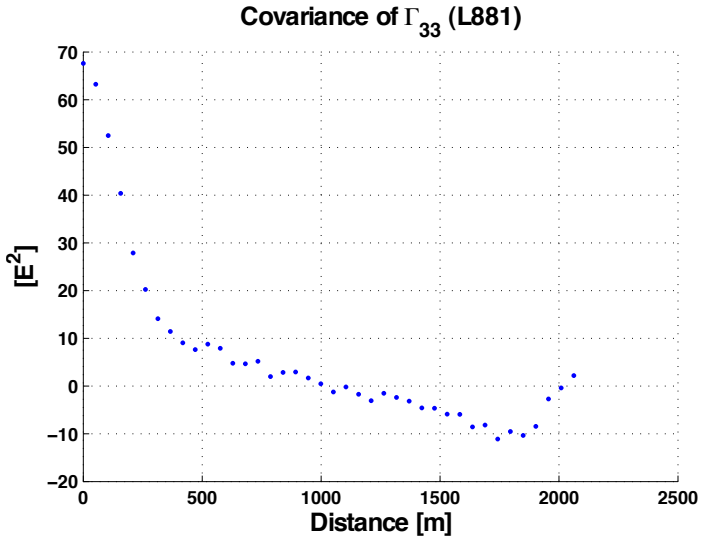

Figure 3.41: Empirical Covariance Function of Vinton Dome Profile L881

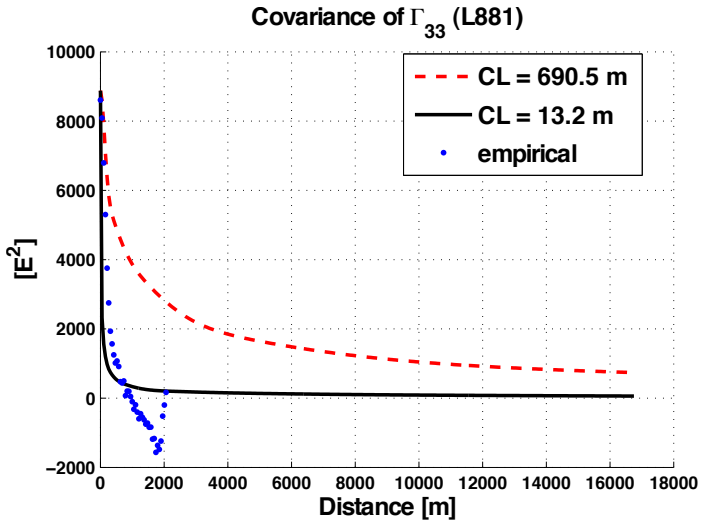

Figure 3.42: Model vs. L881 Empirical Covariance Function

though, as Φ_i remains the same in both cases and the new scale is, therefore, not entirely constant for the entire covariance matrix.

A second profile of the Vinton Dome data set is selected. It is labeled L471. This profile is also measured in North-South direction but it crosses the center of the dome. L471 consists of 317 observation points and has an average point interval of $\Delta x_1 = 52.93\,\mathsf{m}$. Figure 3.43 presents the gravity gradient Γ_{33} of the profile. The Vinton Dome generates a clear maximum within the data set. However, the question is in what way the dome interferes with the localization of a void, which generates a minimum in the Γ_{33} signal. Due to that, the sign of the observed profile is intentionally reversed in the simulations, generating an interfering minimum. The results of the MF under this setup are summarized in Figure 3.44. First of all, there are no edge effects visible compared to those generated by the noise anomaly (3.63). This might be explained by the smaller width of the Vinton Dome anomaly so that the major part of the dome signal is not stretched over the entire profile. It is difficult to provide a more specific explanation at this point as the actual data, in contrast to the Monte Carlo simulations, only provide one realization. The MF fails to detect the sought signal of the prism ($x_1 = 5234\,\mathsf{m}$) as the maximum output is located above the dome ($x_1 = 6563\,\mathsf{m}$). However, the second highest output locates the sought prism. This example emphasizes that even if the global maximum delivers the wrong result it is still worth investigating the local maxima. The shapes of the two maxima (above prism and dome) also indicate that the sharper one is generated by the sought prism.

In contrast to the simulation above, Figure 3.45 shows the results if the covariance matrix is replaced by a simple identity matrix. Again, the global maximum of the

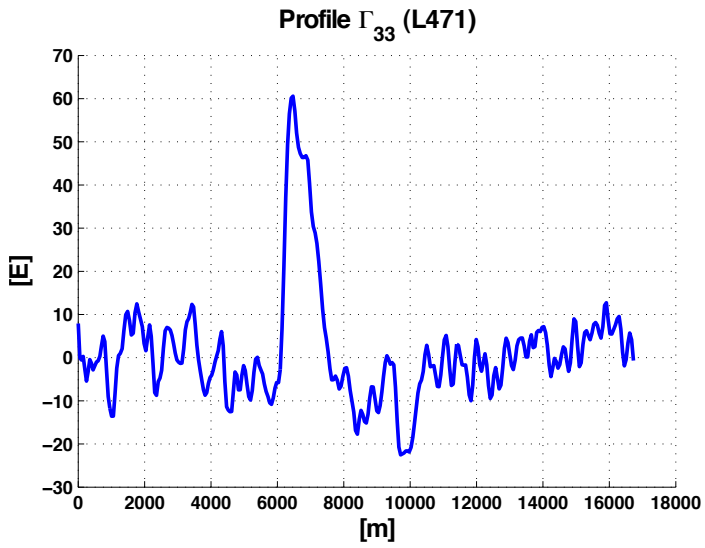

Figure 3.43: Γ_{33} of Vinton Dome Profile L471

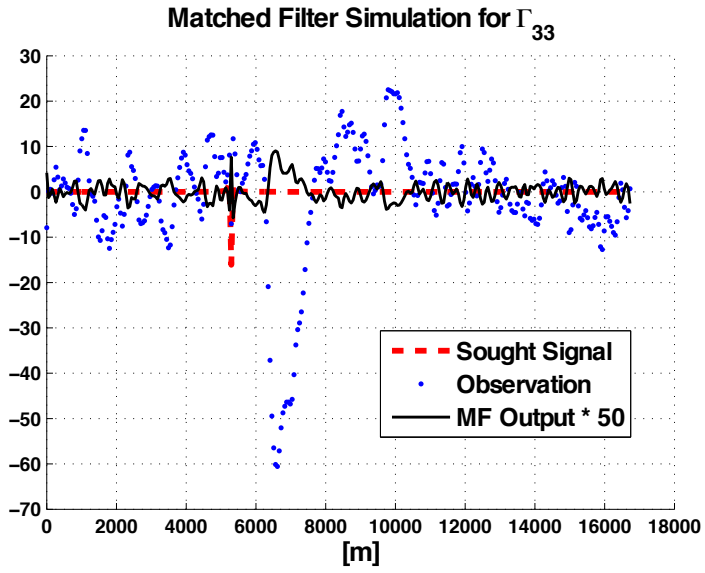

Figure 3.44: MF Simulation of Vinton Dome Profile L471

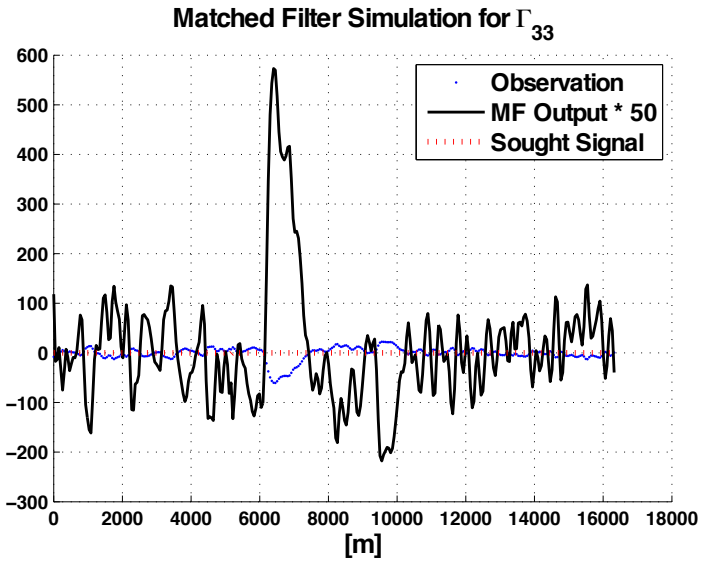

Figure 3.45: MF Simulation of Vinton Dome Profile L471 with Identity Covariance Matrix

filter output lies above the dome but otherwise no distinctive local maximum can be detected. This emphasizes the importance of an appropriate covariance model. If the covariance matrix for the L471 case is replaced by a covariance matrix based on the function with CL = 690.5 m, the sought signal is easily detected by the MF (compare Figure 3.46). The dome seems to have no major influence. Edge effects occur in the filter output that look similar to those observed in Section 3.3.4. The first and last 5 points of the filter output are, therefore, deleted. Since the choice of correlation length in the covariance function has such a huge impact on the performance of the MF, the following simulations are based on different CLs of the covariance model. The assumed point intervals in the computation of the sought signal are always the actual average point intervals of the corresponding observed profile. The prism for the 321-point profile (L881) is located at $x_1 = 5234.38$ m and the prism for the 317-point profile (L471) is located at $x_1 = 5292.75$ m.

A comparison of the results based on the standard covariance function (CL = 13.2 m) and the modified covariance function (CL = 690.5 m), shows that the latter leads to a more distinct and powerful localization of the sought anomaly. One characteristic is thereby the higher value of $y_{\max}$. However, a high $y_{\max}$ is not necessarily an indication for a successful and distinct detection, as a local maximum of the same filter output might be high as well. In that case it becomes unclear if $y_{\max}$ is generated by the sought signal or by a random anomaly in the background field. A Maximum

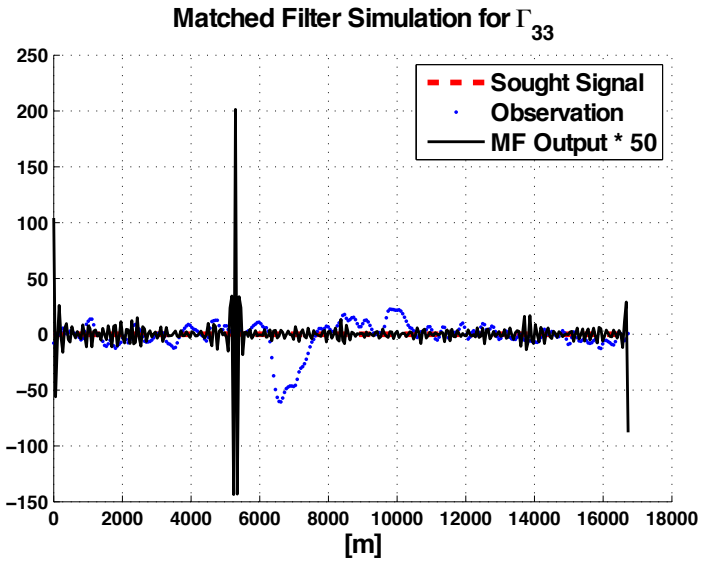

Figure 3.46: MF Simulation of Vinton Dome Profile L471 with CL = 690.5 m

Comparison Ratio is, therefore, defined by

$$\mathrm{MCR} = \frac{y_{\max}}{\frac{1}{3\%N}\sum_{i=1}^{3\%N} y_i^{\text{local maximum}}} \tag{3.66}$$

that takes into account $y_{\max}$ with respect to 3 % of the next highest values of the profile. That means, for the number of points $N \approx 300$, $y_{\max}$ will be divided by the average of 10 side maxima, $y_i^{\text{local maximum}}$. A high MCR stands for a distinct MF output.

Table 3.4 lists the $y_{\max}$ and MCR values of L881 and L471 with respect to the different CLs that were applied in the computation of the covariances. The maxima of $y_{\max}$ and MCR over all cases are in bold. Both parameters are compared to demonstrate that considering $y_{\max}$ only would lead to a different conclusion than to what the MCR suggests. Considering $y_{\max}$ would lead to the interpretation that the strongest filter output is given by CL = 1385.2 m, while the MCR reveals that CL = 690.5 m leads to the most distinct MF output. In addition to the two profiles introduced above, the profile L841 with $\Delta x_1 = 51.64$ m is included. It runs closely parallel to L881. The MF successfully locates the sought signal except in the cases that are starred. The starred cases of L471 mean that the dome has been detected instead. A first impression is that the larger CLs of the covariance model result in a higher filter output. However, the MCR indicates for all three profiles that the covariance function with CL = 690.5 m gives the best results. Best results means here

CL [m]	$y_{\max}$ [−]			MCR [−]		
	L881	L841	L471	L881	L841	L471
7012.5	201.47*	214.10	**243.83***	1.24*	1.50	1.43*
2313.4	196.22	246.60	220.84	2.35	2.67	2.62
1385.2	**239.74**	**257.01**	226.64	4.61	4.37	4.21
863.1	223.74	228.75	226.79	9.09	7.81	8.48
690.5	201.84	203.81	201.47	**10.73**	**10.08**	**10.08**
575.4	174.79	177.24	175.75	9.34	8.80	8.58
460.8	127.07	128.97	128.18	6.04	5.94	6.13
345.2	54.66	55.92	55.28	5.23	5.25	5.46
172.7	13.57	15.79	14.56	4.05	5.13	4.20
115.1	10.77	13.23	11.86	2.93	3.95	2.99
86.4	10.03	12.44	11.15	2.80	3.81	2.76
69.1	9.64	12.00	10.70	2.74	3.75	2.60
34.5	8.26	10.69	9.26	2.26	3.33	1.95
23.0	7.52	10.09	8.53	1.95	3.01	1.57
17.3	7.02	9.72	8.15*	1.72	2.75	1.34*
13.8	6.66	9.47	8.86*	1.55	2.55	1.35*
13.2	6.59	9.42	9.05*	1.52	2.51	1.36*
12.6	6.52	9.37	9.18*	1.48	2.46	1.36*
11.5	6.41	9.29	9.46*	1.43	2.40	1.36*
10.6	6.31	9.23	9.73*	1.39	2.33	1.36*

* false detection, e.g. dome $x_1 = 6563\,\mathsf{m}$

Table 3.4: Vinton Dome Simulations based on a Variation in CL

that the maximum filter output is very distinct and robust to large background noise. The achieved improvement in the MF performance becomes visible, for example, for the L471 profile. There, the MF is able to detect the sought signal if CL = 690.5 m but falsely detects the dome where either the original CL or the CL generating the largest $y_{\max}$ is used as part of the covariance function.

As mentioned before, the covariance matrix of the instrument noise is given by a diagonal matrix with the variance, $\sigma_i^2 = \sigma_{\Gamma_{33}}^2 = 9\,\mathsf{E}^2$, on the diagonal (Table 3.1). Assuming different standard deviations for the instrument noise leads to the effects (for L881) listed in Table 3.5, which compares the MCRs with respect to various σ_i. The table distinguishes between the results based on the original background noise covariance function and its modification for correlation length and instrument noise. A change in σ_i has clearly an effect on the MCR, however, in all cases it becomes also obvious that the MCR is much higher for the modified covariance function. The

$\sigma_i[\mathsf{E}]$	MCR [−]	
	CL = 13.2 m	CL = 690.5 m
1	1.52	8.52
3	1.52	10.73
10	1.51	8.39
20	1.47	5.95

Table 3.5: MCR under the Influence of Instrument Noise in Vinton Dome Simulations

improvement of the MF performance if CL = 690.5 m, is, therefore, obvious, regardless of the covariance matrix describing the instrument noise.

The proceeding MF computations analyze if the simulation setup that one observation point is always centered above the modeled mass anomaly influences the outstanding improvement in detection. For that reason, the origin of the mass anomaly is now placed at $x_{m_1} = 100 \cdot \Delta x_1 - 20\,\mathsf{m} = 5214.38\,\mathsf{m}$ of the L881 profile. That means the center of the prism is placed 20 m to the south from the closest observation point, which reduces the observed signal strength of the sough mass anomaly. The observation vector, the sought signal, and the MF output based on the original covariance function are plotted in Figure 3.47 a). $y_{\max}$ is located at $x_1 = 1361\,\mathsf{m}$, which is not the location of the sought anomaly but of a random background anomaly. This is also the local maxima in Figure 3.39 and demonstrates how fragile the detection is in this case. If the interval between the observation points is too large, so that the distance of the void to the nearest observation point is relatively far, the MF might fail and be corrupted by the local background noise. Figure 3.47 b) shows a close-up of the location around the void. The MF output is still sensitive to the sought signal but overpowered by the background signal. If the same shift of 20 m is simulated again but now in combination with the covariance function of CL = 690.5 m, the MF is able to clearly detect the void as shown in Figure 3.48. The MCR is 3.96 versus 10.73 (Table 3.4) in the case where one observation point falls above the center of the prism. Placing the maximum of the sought signal between two observation points decreases, of course, the strength of the sought signal part in the observation vector and results in a weaker MF performance (smallerMCR). However, the above simulations still show the same positive effect by modifying the correlation length of the covariance function.

The question is if these findings are also reflected in the simulations designed in Section 3.1. For that reason, the previous Monte Carlo simulations based on Γ_{33} are carried out again but with covariance matrices varying in CL. Only 3 side maxima of the filter output enter (3.66) since the number of profile points is reduced to 101.

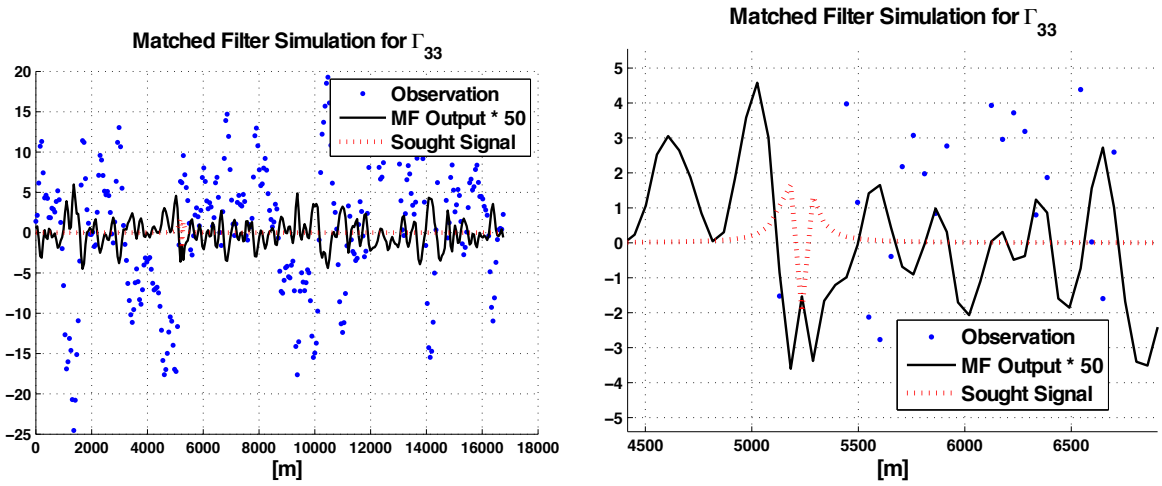

Figure 3.47: Center of Signal shifted from L881 Observation Point a) Profile b) Close-Up

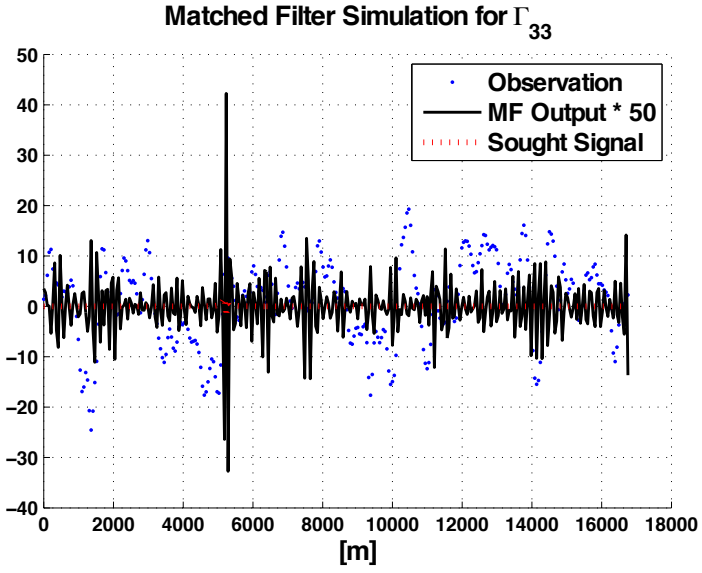

Figure 3.48: Center of Signal shifted with CL = 690.5 m

CL [m]	λ [−]	$\overline{y}_{\max}$ [−]	%	$\overline{\text{MCR}}$ [−]
132.9	**39.320**	**71.014**	25.0	1.153
66.7	32.283	55.243	27.7	1.201
44.4	24.918	39.679	28.4	1.235
33.3	18.739	27.154	34.3	1.256
26.1	13.963	18.249	42.1	1.296
21.9	10.407	12.219	54.0	1.351
18.8	7.811	8.496	65.0	1.445
16.5	5.934	6.176	75.0	1.558
14.7	4.588	4.688	82.3	1.679
13.2	3.627	3.690	**84.9**	**1.747**
12.0	2.947	3.014	82.6	1.724
11.0	2.479	2.564	78.0	1.640
10.2	2.134	2.282	68.9	1.546
9.5	1.901	2.118	61.9	1.462
8.8	1.738	2.024	54.4	1.394
8.3	1.624	1.973	47.9	1.341
7.8	1.544	1.950	42.9	1.302
7.3	1.487	1.942	40.3	1.273
6.9	1.447	1.944	38.0	1.252
6.6	1.419	1.950	37.0	1.238

Table 3.6: Monte Carlo Simulations based on a Variation in CL

The results are summarized in Table 3.6, which lists the square root of the SNR, the mean of 1000 maximum filter outputs, the percentage of successful detections and the mean of all the Maximum Comparison Factors. The largest value of each column is bold. It should be noted that the mean of the maximum filter output does not only account for the successful detections but includes the maxima for all 1000 simulations. A successful detection is here defined in the range of $\pm 2\Delta x_1 = \pm 2\,\mathsf{m}$ from the correct location at $x_{m_1} = 30 \cdot \Delta x_1 = 30\,\mathsf{m}$. Again, the longest correlation length generates the highest maximum filter output as well as SNR but the highest MCR is provided by the covariance function with a correlation length of CL = 13.2 m. This case also stands for the most successful detection of the mass anomaly. It is interesting to realize that it is also the case where the difference between λ and $\overline{y}_{\max}$ is the smallest. These Monte Carlo simulations analyze the detections where the best results are achieved if the simulated point interval and the correlation length of the covariance model coincide. That means a change in CL from the natural one does not enhance the detection.

CL [m]	λ [−]	$\overline{y}_{\max}$ [−]	%	$\overline{\text{MCR}}$ [−]
6600.0	**53.389**	**56.678**	72.6	1.581
2200.0	50.330	52.571	78.3	1.663
1320.0	47.034	48.782	82.0	1.696
825.0	41.489	43.232	82.0	1.684
660.0	37.272	39.034	80.1	1.637
550.0	32.479	34.477	76.3	1.543
440.0	23.709	25.774	71.6	1.383
330.0	10.318	11.136	72.8	1.396
165.0	3.066	3.136	**88.6**	**1.816**
110.0	2.616	2.683	86.3	1.781
82.5	2.475	2.539	86.4	1.778
66.0	2.388	2.449	86.4	1.777
33.0	2.137	2.197	85.1	1.760
22.0	2.031	2.090	84.1	1.748
16.5	1.965	2.028	83.3	1.727
13.2	1.921	1.989	81.6	1.707
12.0	1.892	1.964	81.1	1.692
11.0	1.905	1.975	80.4	1.699
10.2	1.881	1.955	80.0	1.686

Table 3.7: Monte Carlo Simulations based on a Variation in CL and 50 m Spacing

The next set of tests (Table 3.7) are a mixture of the simulations of Table 3.4 and Table 3.6 as the following results are based on a Monte Carlo simulation with 101 observations points and a point interval of $\Delta x_1 = 50\,\mathsf{m}$ resulting in a profile of 5 km length. The size of the prism is also $a = 10\,\mathsf{m}$, $b = 10000\,\mathsf{m}$, and $c = 4\,\mathsf{m}$. The prism is only at a depth of $d = 6\,\mathsf{m}$ and located at $x_{m_1} = 30 \cdot \Delta x_1 = 1500\,\mathsf{m}$. A successful detection is defined as a detection within a range of $\pm 2\Delta x_1 = \pm 100\,\mathsf{m}$ from the actual location. The maximum values in the columns of Table 3.7 are again given in bold. In contrast to the previous analysis where the optimal CL coincides with the original CL = 13.2 m modeled for a point interval $\Delta x_1 = 1\,\mathsf{m}$, this modified simulation suggests an optimal CL of 165 m . However, the differences in the $\overline{\text{MCR}}$ are relatively small and the improvement in a successful detection with respect to the point interval of the observations increases only by 7 %. Furthermore, the standard deviation of the MCR,

$$\sigma_{\text{MCR}} = \sqrt{\frac{1}{N-1}\sum_{i=1}^{N}\left(\text{MCR}\,(i) - \overline{\text{MCR}}\right)^2}, \tag{3.67}$$

over $N = 1000$ realizations in the standard simulations (Table 3.6) is 0.458 for CL = 13.2 m, and the corresponding standard deviation in the modified simulation (Table 3.7) is 0.483 for CL = 165 m. Those standard deviations are relatively high and, therefore, less emphasis should be put on the small differences in $\overline{\text{MCR}}$ if only a single realization is available. However, further simulations based on the same settings as for Table 3.7 show that even if the simulated observation point interval is altered to either $\Delta x_1 = 30\,\text{m}$, $\Delta x_1 = 100\,\text{m}$, or $\Delta x_1 = 150\,\text{m}$ the most successful detection is provided by applying the covariance model of CL = 165 m. Success is thereby measured by a large MCR and a high detection rate. The question why the optimal CL is not more sensitive to the simulated point interval is a task for future studies.

In conclusion, there is no apparent reason in theory that requires a covariance function of a modified large CL. The simulations of the Vinton Dome profiles reveal though that the modified CL has a huge impact on the MF performance while the simulated profiles only gain a minor improvement if any. A possible reason for these different effects is that the Vinton Dome data in contrast to the simulated background is airborne and, therefore, smoother, which consequently leads to a higher correlation. The narrow anomaly introduces a short-wavelength signal, which sticks out if the surrounding background is highly correlated.

The practical conclusion from these tests is that one way to further advance the MF performance is to add a sought signal to the observed data and to determine the best covariance for the detections based on various CLs. This covariance matrix can then be used for the entire data set. The generated sought signal should either be placed in an area where it is known that no other signal exists or it should be different from the actual signal of interest to avoid interferences. The gained improvement becomes especially apparent if the instrument noise is high, interference from a strong background anomaly exists, and no observation point is directly placed above the sought anomaly.

3.3.6 Multiple Profiles

The major scope of this dissertation is to locate a mass anomaly along a straight profile, hence the extended shape of the prism in x_2-direction. However, the MF formulas in Chapter 2 are designed such that a two-dimensional search for a mass anomaly limited in both x_1- and x_2-dimensions is possible as well. A new set of Monte Carlo simulations computes three profiles along the x_1-direction, that are parallel to each other and $\Delta x_2 = 3\,\text{m}$ apart. The observation point interval along the profile remains $\Delta x_1 = 1\,\text{m}$. Due to the designed extension of the void ($b = 100\,\text{m}$), the task remains a one-dimensional search (location of the anomaly along x_1) but the task is now to see if the observations of a grid rather than a profile are able to improve this detection. The global maximum filter output determines the location of the mass

Observation Type	Detection Rate [%]			
	2 m	3 m	4 m	5 m
Gravity Gradient Γ_{13}	99.4	24.7	13.6	10.8

Table 3.8: MF Detection with 3 Profiles for Various Depths of the Anomaly

anomaly, however, due to the long shape of the prism, all three profiles are expected to have a local maximum at $x_1 = 30\,\mathsf{m}$. The output domain of the MF is here 3×101.

Out of 1000 MF runs the observation based on Γ_{13} have the following success rate depending on the depth of the void (see Table 3.8). All detections, which are determined by the global maximum filter output, have improved in comparison to the single profile simulations (see Table 3.2). Even though the profiles are highly correlated, adding two more profiles improves the MF performance. This result is similar to combining the Γ_{13} observations with two further gravity gradient components, where Γ_{11} and Γ_{33} are negatively correlated to each other. Figure 3.49 compares the successful detection rate for a single profile, three profiles, and a single profile with three components with respect to the anomaly depth. It is interesting to notice that the curve of the three profiles is similar to the one for one profile with three components only up to a depth of 3 m. Beyond that, the three components are more successful while there is hardly any difference between the solutions based on the three or on the one profile anymore. Adding more observation profiles seems to have only a positive effect in the very shallow subsurface. One issue that arises in this case is that the three profiles are highly correlated to each other in x_2-direction (across-track), which results in a high correlation of the MF outputs, y. This complicates a statistical interpretation of the MF output as described in Chapter 4.

3.3.7 Orientation of Source

The MF simulations are based on several assumptions to detect a mass anomaly. In order to solve for the geophysical inverse problem and to implement an MF, the properties of the sought signal must be known or estimated a priori. Those properties are the shape and size of the anomaly (prism parameters), the depth (or signal strength), the density and magnetic contrast, and the orientation of the anomaly. The above simulations assume that the prism lies in the horizontal plane and its long side is perpendicular to the observed profile. In the following MF simulations the prism is rotated around the vertical axis, x_3, by the angle, γ_{rot}. The pivot point lies thereby above the center of the prism (Figure 3.50). That means the pivot point is at the

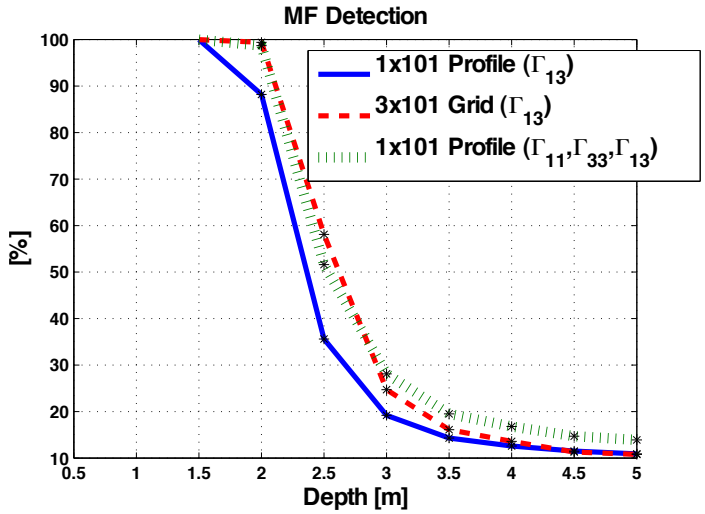

Figure 3.49: MF Detection with 1 or 3 Profiles

origin of the local coordinate system when deriving the sought signal. When modeling the signal in the observation field (3.1) the coordinates of the pivot point are $\left[\begin{array}{ccc} x_1 & x_2 & x_3 \end{array}\right]^T = \left[\begin{array}{ccc} 30\,\mathrm{m} & 37\,\mathrm{m} & 0\,\mathrm{m} \end{array}\right]^T$. The same equations (3.1) hold that compute the three-dimensional prism in Chapter 3.1.1 in the local x–coordinate system. However, in order to change the orientation of the prism, the input coordinates are rotated by the angle γ_{rot}. For example, the previous 101×101 grid points of the sought signal, $x_1 = x_2 = -50, \ldots, 50$, now become the grid points in the rotated u-coordinate system

$$\left[\begin{array}{c} u_1 \\ u_2 \\ u_3 \end{array}\right] = \mathbf{R_3}\left(\gamma_{rot}\right) \left[\begin{array}{c} x_1 \\ x_2 \\ x_3 \end{array}\right] \tag{3.68}$$

with the rotation matrix

$$\mathbf{R_3}\left(\gamma_{rot}\right) = \left[\begin{array}{ccc} \cos\left(\gamma_{rot}\right) & \sin\left(\gamma_{rot}\right) & 0 \\ -\sin\left(\gamma_{rot}\right) & \cos\left(\gamma_{rot}\right) & 0 \\ 0 & 0 & 1 \end{array}\right]. \tag{3.69}$$

As the rotation is defined in the horizontal plane, the vertical coordinate remains zero, $u_3 = x_3 = 0$. The coordinates of the rotated u-system enter the equations for the gravity gradients above a prism (3.1). In order to yield the same gravity gradients in the x–coordinate system, the entire tensor matrix is transformed back to the original system by

$$\left[\begin{array}{ccc} \Gamma_{11} & \Gamma_{12} & \Gamma_{13} \\ \Gamma_{21} & \Gamma_{22} & \Gamma_{23} \\ \Gamma_{31} & \Gamma_{32} & \Gamma_{33} \end{array}\right]_{\text{x - system}} = \mathbf{R_3^T}\left(\gamma_{rot}\right) \left[\begin{array}{ccc} \Gamma_{11} & \Gamma_{12} & \Gamma_{13} \\ \Gamma_{21} & \Gamma_{22} & \Gamma_{23} \\ \Gamma_{31} & \Gamma_{32} & \Gamma_{33} \end{array}\right]_{\text{u - system}} \mathbf{R_3}\left(\gamma_{rot}\right). \tag{3.70}$$

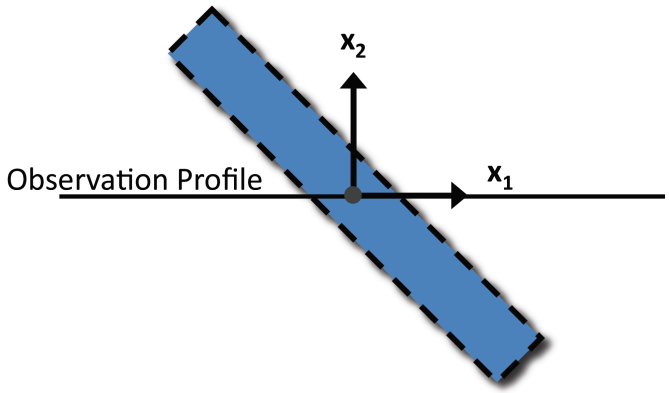

Figure 3.50: Horizontal Rotation of Prism

The magnetic field generated by a rotated prism is derived by applying Poisson's Relation (2.40) to the gravity gradients on the left-hand side of (3.70). A comparison of the sought signal of, for example Γ_{13} and Γ_{22}, based on the original simulation setup, where the prism is perpendicular to the profile ($\gamma_{\text{rot}} = 0\,^\circ$), and based on $\gamma_{\text{rot}} = 45\,^\circ$ are plotted in Figure 3.51. In the case of Γ_{13}, the rotation produces a slightly broader and weaker signal while in the case of Γ_{22}, the sought signal changes from almost being zero to a sharp peak of about 43 E.

Again, 1000 test runs are simulated and their results presented in Figure 3.52. It plots the percentage of a successful detection against the rotation angle γ_{rot}, which goes from $0\,^\circ$ to $45\,^\circ$. Beyond $45\,^\circ$, the profile should be heading from East to West (x_2-direction) as the location of the prism is in that case rather defined by the x_2- than the x_1-coordinate. The interval between two consecutive rotations is $2.5\,^\circ$. The dashed line in Figure 3.52 is based on the gravity gradient component Γ_{13} and a simulated mass anomaly at 2 m depth. As it is to be expected, the performance of the MF decreases with an increase in γ_{rot}. The MF is able to detect the prism in 88.2 % of the cases where $\gamma_{\text{rot}} = 0\,^\circ$ (compare Table 3.2) but only 27.3 % where $\gamma_{\text{rot}} = 45\,^\circ$. On the other hand, the gravity gradient component Γ_{22} improves the performance (line of vertical stripes) with an increase in γ_{rot}, correspondingly. This gradient component was neglected so far since it is very small (zero if $b = \infty$), however, the rotations result in a gravity change along the x_2-direction. The solid line describes the MF performance when the two gradients are combined in the detection process. The performance of the combination always exceeds the single gradient solution at any point. The successful detection does not fall below 64 %. This supports the conclusion that the more gravity gradients are combined the better the detection as presented in Table 3.3. The minimum of the (Γ_{13}, Γ_{22}) detection line is at the same angle where the Γ_{13} detection line and the Γ_{22} detection line cross.

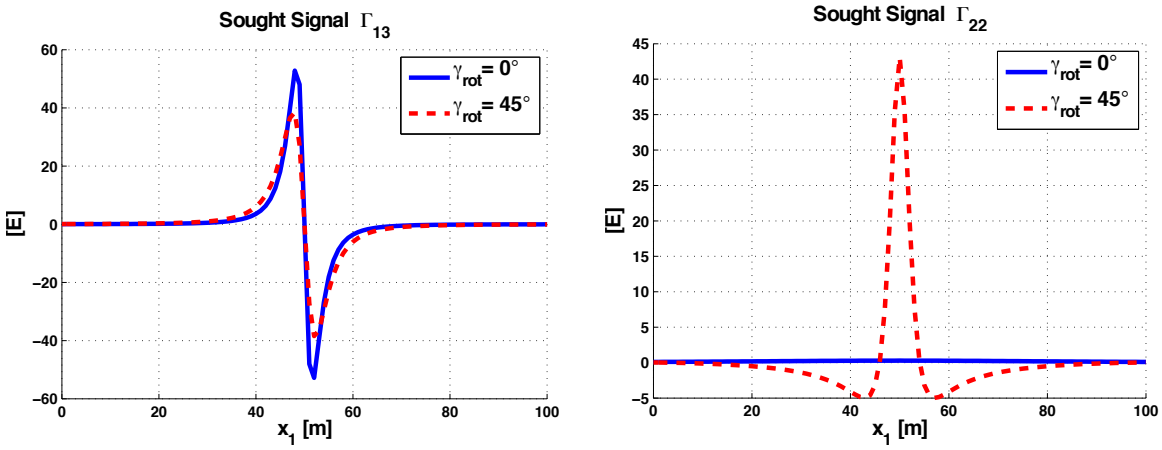

Figure 3.51: Effect on Prism Rotation on a) Γ_{13} b) Γ_{22}

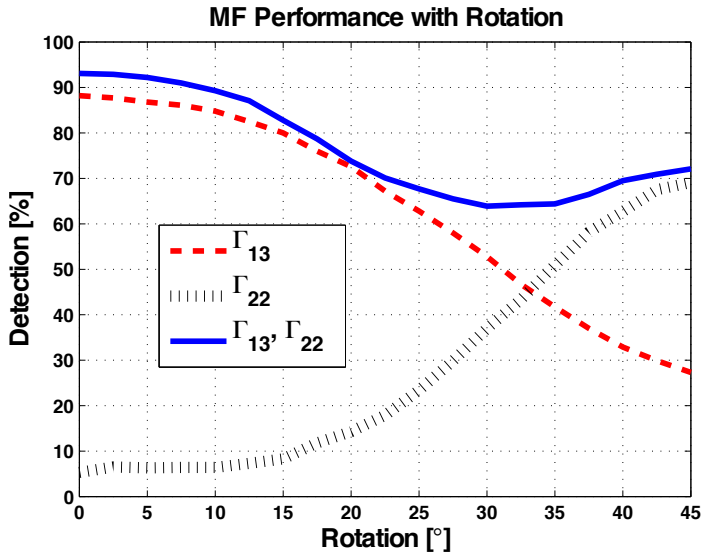

Figure 3.52: MF Performance under Rotation of the Prism

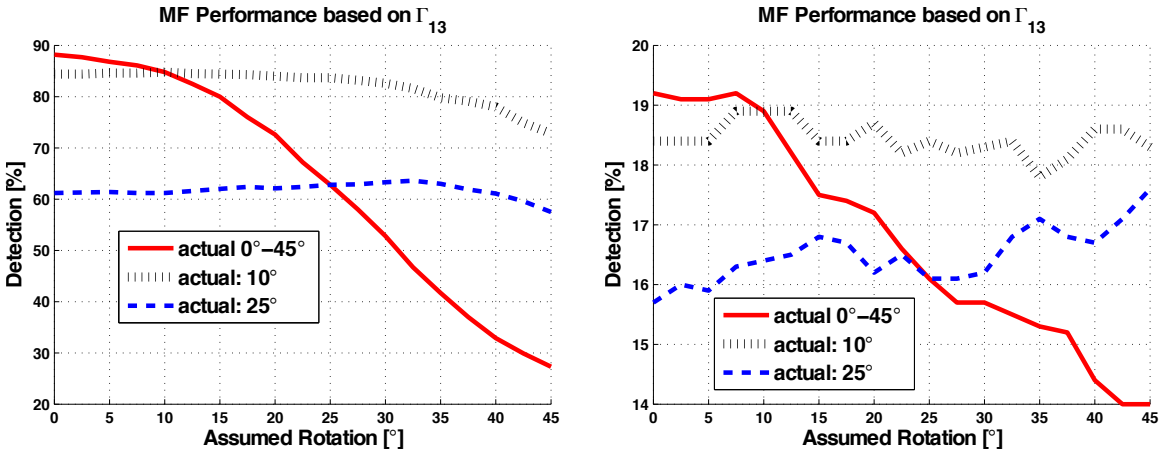

Figure 3.53: Estimation of Rotation with Prism Depth at a) 2 m b) 3 m

The follow-up question is how sensitive is the MF performance to a falsely assumed rotation angle, γ_{rot}, in the design of the sought signal, s. Figure 3.53 demonstrates the effects for Γ_{13} observations where the anomaly is placed at 2 m and 3 m depth, respectively. The line of vertical stripes contains observations based on $\gamma_{\text{rot}} = 10\,^\circ$ and the dashed line contains observations based on $\gamma_{\text{rot}} = 25\,^\circ$ as the true orientation of the sought signal. The assumed γ_{rot} in the sought signal ranges from $0\,^\circ$ to $45\,^\circ$ with an interval of $2.5\,^\circ$. The solid line serves as a reference where γ_{rot} in the observation, z, and the sought signal, s, are the same, hence the crossing points at $10\,^\circ$ and $25\,^\circ$. That also means that the solid curve in Figure 3.53 is identical to the dashed curve in Figure 3.52.

The MF detection performance is clearly less sensitive to the discrepancy of the rotation angles between the modeled signal and the signal contained in the observations than it is to the discrepancy of the assumed and actual prism depths (Section 3.3.3). Here, there is no distinctive maximum in the performance where the assumed γ_{rot} matches the actual γ_{rot}. A difference of up to $20\,^\circ$ in both of those angles hardly diminishes the MF performance. If data are collected along several parallel profiles (see Section 3.3.6), the maximum of the MF output, y, in each line will delineate the prism according to its orientation. Only in the case of $\gamma_{\text{rot}} = 0\,^\circ$ the maximum is supposed to be at $x_1 = 30\,\text{m}$ in each line. A rough estimate of the assumed rotation angle in the design of the sought signal should be sufficient. Otherwise, an iteration of assumed γ_{rot} further improves the delineation of the prism [Jekeli and Abt, 2010].

Chapter 4: Statistical Analysis

The Matched Filter (MF) maximizes the Signal-to-Noise Ratio (SNR) and the maximum of the filter output indicates the location of the sought signal, s. That means the MF will always declare a location for the sought signal because there is always a maximum value even if the sought signal does not exist. In such a case, the maximum in the filter output is generated by a random local anomaly in the background noise. Sometimes, the sought signal does exist but is too weak to be detected, e.g. if the generating source is buried too deeply under the ground. Again, the maximum of the filter output might be generated by a local background feature. In general, the MF provides the most likely location of the sought signal but the question of how likely is only answered by looking into statistical details.

In statistics, binary hypothesis tests are designed to determine if either one choice or the other is true (Null Hypothesis, H_0, versus Alternative Hypothesis, H_1). Here, the decision is to be made if the maximum filter output locates the sought anomaly or not. This decision is derived by a test of likelihood ratio based on the observations and its comparison to a defined threshold. Two fundamental types of hypothesis tests are commonly in use where the threshold is either designed by the Bayes criterion or by the Neyman-Pearson criterion ([Kay, 1998], [Middleton, 1960], [Srinivasan, 2002]). The Bayes criterion requires an estimate of the a priori probability of the observations in order to determine the decision threshold. Since, in the case of the presented MF application, it is unknown if the sought signal even exists, modeling a priori probabilities becomes challenging. The Neyman-Pearson criterion, however, defines the threshold not by a priori probabilities but by a constraint as stated below and is, therefore, applied to the given MF example.

4.1 Neyman-Pearson Criterion

The Neyman-Pearson criterion tests the hypotheses while minimizing the probability of a Type II error, denoted β, for a given probability of a Type I error, denoted α. The Type I error is defined as the wrong rejection of the Null Hypothesis, and the Type II error is defined as the wrong acceptance of the Null Hypothesis. The decision process is a tradeoff between the probabilities of those two errors. In contrast to Bayes, Neyman-Pearson cannot reduce both probabilities simultaneously.

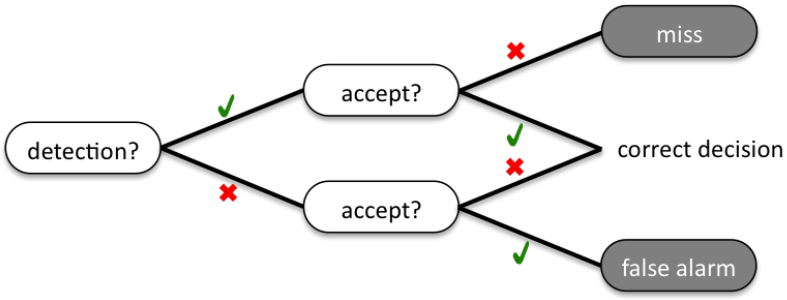

Figure 4.1: Probabilities based on Decisions

Two different approaches are possible to formulate the Null Hypothesis. Under Setup A, the Null Hypothesis states that there is no signal, and under Setup B, the Null Hypothesis sates, that there is a signal. The Alternative Hypotheses change accordingly.

Setup A

$H_0^{(A)}$: There is no (detectable) signal in the observations.

$H_1^{(A)}$: There is a (detectable) signal in the observations.

Setup B

$H_0^{(B)}$: There is a (detectable) signal in the observations.

$H_1^{(B)}$: There is no (detectable) signal in the observations.

The purpose why both setups are considered is that Setup A allows to determine the Probability Of a Miss (POM) and Setup B allows to determine the Probability Of a False alarm (POF). A miss is the error that occurs when the MF output has correctly detected the sought signal but the selected hypothesis declares that there is no signal. A false alarm occurs when the MF output has not detected the sought signal but the selected hypothesis declares that the filter output locates the signal. Both probabilities are illustrated in Figure 4.1. Whether Setup A or Setup B is more appropriate depends on the specific application. When detecting hazardous areas, it is more important not to miss any hazards even if it increases the number of false alarms. When detecting a mineral for mining, it is more important to avoid cost intensive false alarms even if it increases the chance of missing some sources. Setup A and B are mostly inverse to each other but will here still be discussed separately in more details. All probabilities are thereby theoretically derived and do not depend on empirical or simulated data sets.

4.1.1 Setup A

The Neyman-Pearson criterion compares a likelihood ratio, LR, to a threshold, ψ_0, defined by probabilities. In case of Setup A, LR is defined as the ratio between the a posteriori probability densities, f, for the observations, z, where either $H_1^{(A)}$ or $H_0^{(A)}$ is true

$$\mathrm{LR} = \frac{f_{z|H_1^{(A)}}\left(z|\, H_1^{(A)}\right)}{f_{z|H_0^{(A)}}\left(z|\, H_0^{(A)}\right)}. \tag{4.1}$$

The decision whether $H_0^{(A)}$ is accepted or rejected is based on a constant threshold, $\psi_0^{(A)}$.

$$\begin{aligned} &\text{If } \mathrm{LR} \geq \psi_0^{(A)} \Longrightarrow \text{reject } H_0^{(A)} \\ &\text{If } \mathrm{LR} < \psi_0^{(A)} \Longrightarrow \text{accept } H_0^{(A)} \end{aligned} \tag{4.2}$$

LR is linearly related to the maximum filter output, $y_{\max}$, given by

$$\ln\left(\mathrm{LR}\right) = \lambda y_{\max} - \frac{1}{2}\lambda^2 \tag{4.3}$$

under the assumption that the background noise is Gaussian [Jekeli and Abt, 2010]. An appropriate threshold can, therefore, simply be compared to $y_{\max}$ instead of LR. As described in Section 3.1.2 and 3.2, the background noise is considered to be approximately a stationary Gaussian process. Consequently, the observation (2.47) is also approximately Gaussian distributed and since the MF is a linear filter, the filter output, y, will also be Gaussian with the statistical mean (2.70) and a unit standard deviation (2.71). If the sought signal is strong (reject $H_0^{(A)}$ and accept $H_1^{(A)}$) the maximum filter output, $y_{\max}$, will not vary in location among all, r, with different realizations. Consequently, $y_{\max}$ will also be Gaussian and its probability density under hypothesis $H_1^{(A)}$ can be expressed as

$$f_{y_{\max}|H_1^{(A)}}\left(y_{\max}|\, H_1^{(A)}\right) = \frac{1}{\sqrt{2\pi}} e^{-\frac{1}{2}(y_{\max}-\lambda)^2}, \tag{4.4}$$

[Bronshteĭn, 2007, p.758].

If there is no signal (accept $H_0^{(A)}$ and reject $H_1^{(A)}$) the maximum filter output, $y_{\max}$, is not Gaussian anymore but will follow the concepts of order statistics [Nevzorov, 2001], [Srinivasan, 2002]. If the filter outputs, y, are identically and independently distributed for all r, the probability density function is defined by

$$f_{y_{\max}}\left(y_{\max}\right) = N\left(F_y\left(y_{\max}\right)\right)^{N-1} f_y\left(y_{\max}\right) \tag{4.5}$$

where N is the number of points, r, and f_y stands for the density function of y. The function F is called Cumulative Distribution Function (CDF) and represents the

probability that $y \leq y_{\max}$ is true [Evans et al., 2000]. Following this theory, F is a continuous variable depending on the parameter $y_{\max}$.

The MF outputs, y, are identically distributed (Gaussian, zero-mean, unit standard deviation) in the absence of a signal. This fulfills the condition of order statistics but, in general, the background noise has some correlation and in addition, the observation vector, z, is convolved with the same sought signal, s, for all realizations. This has the effect that the MF outputs are no longer independently distributed. However, since the signal shape is rather sharp (Figure 3.3, Figure 3.4) and zero most of the time, the MF outputs are here assumed as approximately independently distributed [Jekeli and Abt, 2010] so that the theory of order statistics can still be applied. Inserting the density function

$$f_{y|H_0^{(A)}}\left(y_{\max}|\, H_0^{(A)}\right) = \frac{1}{\sqrt{2\pi}} e^{-\frac{1}{2}y_{\max}^2} \tag{4.6}$$

and the CDF for the standard normal distribution [Bronshteĭn, 2007, p.759],

$$F_{y|H_0^{(A)}}\left(y_{\max}|\, H_0^{(A)}\right) = \frac{1}{2} + \frac{1}{2}\operatorname{erf}\left(\frac{y_{\max}}{\sqrt{2}}\right), \tag{4.7}$$

into (4.5), the probability density for y under $H_0^{(A)}$ is presented by

$$f_{y_{\max}|H_0^{(A)}}\left(y_{\max}|\, H_0^{(A)}\right) = N\left(\frac{1}{2} + \frac{1}{2}\operatorname{erf}\left(\frac{y_{\max}}{\sqrt{2}}\right)\right)^{N-1} \frac{1}{\sqrt{2\pi}} e^{-\frac{1}{2}y_{\max}^2} \tag{4.8}$$

where erf stands for the error function.

The probabilities of a Type I error, α, and a Type II error, β, determined by the Neyman-Pearson hypothesis test are derived as

$$\begin{aligned} \alpha^{(A)} &= \int_{\psi_0^{(A)}}^{\infty} f_{y_{\max}|H_0^{(A)}}\left(y_{\max}|\, H_0^{(A)}\right) \mathrm{d}y_{\max} \\ &= \frac{N}{\sqrt{2\pi}} \int_{\psi_0^{(A)}}^{\infty} \left(\frac{1}{2} + \frac{1}{2}\operatorname{erf}\left(\frac{y_{\max}}{\sqrt{2}}\right)\right)^{N-1} e^{-\frac{1}{2}y_{\max}^2} \mathrm{d}y_{\max} \end{aligned} \tag{4.9}$$

and

$$\begin{aligned} \beta^{(A)} &= \int_{-\infty}^{\psi_0^{(A)}} f_{y_{\max}|H_1^{(A)}}\left(y_{\max}|\, H_1^{(A)}\right) \mathrm{d}y_{\max} \\ &= \frac{1}{2} + \frac{1}{2}\operatorname{erf}\left(\frac{\psi_0^{(A)} - \lambda}{\sqrt{2}}\right) \end{aligned} \tag{4.10}$$

where $\psi_0^{(A)}$ is the constant threshold under Setup A (4.2). As stated above, the Neyman-Pearson criterion minimizes β for a given α. Setting $\alpha^{(A)}$ to a certain value, (4.9) can be numerically solved for the threshold $\psi_0^{(A)}$.

4.1.2 Setup B

The likelihood ratio, LR, in Setup B is the reverse of the ratio in Setup A (4.1) and becomes

$$\mathrm{LR} = \frac{f_{z|H_0^{(B)}}\left(z|\, H_0^{(B)}\right)}{f_{z|H_1^{(B)}}\left(z|\, H_1^{(B)}\right)}. \tag{4.11}$$

The decision making process changes accordingly to

$$\begin{aligned} &\text{If } \mathrm{LR} \geq \psi_0^{(B)} \Longrightarrow \text{reject } H_0^{(B)} \\ &\text{If } \mathrm{LR} < \psi_0^{(B)} \Longrightarrow \text{accept } H_0^{(B)}. \end{aligned} \tag{4.12}$$

Under both Setup A and B, the LR or $y_{\max}$ must be greater or equal to the corresponding threshold in order to declare the maximum filter output as a detected signal.

The probability densities for $y_{\max}$ under $H_0^{(B)}$ and $H_1^{(B)}$ in Setup B are also reversed to those of Setup A and can be expressed as

$$f_{y_{\max}|H_0^{(B)}}\left(y_{\max}|\, H_0^{(B)}\right) = f_{y_{\max}|H_1^{(A)}}\left(y_{\max}|\, H_1^{(A)}\right) \tag{4.13}$$

and

$$f_{y_{\max}|H_1^{(B)}}\left(y_{\max}|\, H_1^{(B)}\right) = f_{y_{\max}|H_0^{(A)}}\left(y_{\max}|\, H_0^{(A)}\right). \tag{4.14}$$

This results in the following probabilities of a Type I error

$$\begin{aligned} \alpha^{(B)} &= \int_{-\infty}^{\psi_0^{(B)}} f_{y_{\max}|H_0^{(B)}} \mathrm{d}y_{\max} \\ &= \frac{1}{2} + \frac{1}{2}\,\mathrm{erf}\left(\frac{\psi_0^{(B)} - \lambda}{\sqrt{2}}\right) \end{aligned} \tag{4.15}$$

and a Type II error

$$\begin{aligned} \beta^{(B)} &= \int_{\psi_0^{(B)}}^{\infty} f_{y_{\max}|H_1^{(B)}}\left(y_{\max}|\, H_1^{(B)}\right) \mathrm{d}y_{\max} \\ &= \frac{N}{\sqrt{2\pi}} \int_{\psi_0^{(B)}}^{\infty} \left(\frac{1}{2} + \frac{1}{2}\,\mathrm{erf}\left(\frac{y_{\max}}{\sqrt{2}}\right)\right)^{N-1} e^{-\frac{1}{2}y_{\max}^2} \mathrm{d}y_{\max}, \end{aligned} \tag{4.16}$$

which are opposite to those of Setup A.

The threshold under Setup B is determined by choosing a value for $\alpha^{(B)}$ and solving (4.15) for $\psi_0^{(B)}$:

$$\psi_0^{(B)} = \lambda + \sqrt{2}\,\mathrm{erf}^{-1}\left(2\alpha^{(B)} - 1\right). \tag{4.17}$$

Table 4.1 summarizes the POMs and POFs under Setup A and B.

Error Probability	Setup A	Setup B
α (Type I)	theoretical POF	theoretical POM
β (Type II)	theoretical POM	theoretical POF

Table 4.1: Theoretical Error Probabilities

4.2 Statistical Interpretation of MF Simulations

The performance of the Matched Filter is tested by implementing the Monte Carlo simulation with 1000 test runs of the track of $N = 101$ points. Based on this, the empirical, here more precisely the simulated, POMs and POFs are derived and compared to the theoretically computed probabilities. If $y_{\max}$ is greater or equal to the corresponding threshold of Setup A or B, the MF filter output is accepted as a successful detection. If $y_{\max}$ is less than the corresponding threshold the MF filter output is rejected and no signal is found. The empirical POM is the number of all wrongly rejected successes divided by the total number of successes,

$$\text{POM} = \frac{\#\,\text{successes when } y_{\max} < \psi_0}{\#\,\text{successes}}. \tag{4.18}$$

The empirical POF is the number of all wrongly accepted failures divided by the total number of failures,

$$\text{POF} = \frac{\#\,\text{failures when } y_{\max} > \psi_0}{\#\,\text{failures}}. \tag{4.19}$$

Setting the probability of a Type I error under Setup A to $\alpha^{(A)} = 5\,\%$ gives the following threshold $\psi_0^{(B)} = 3.287$ based on $N = 101$ profile points. The threshold is numerically derived from Figure 4.2 which is the discrete realization of equation (4.9).

Table 4.3 shows the MF results for the gravity gradient component Γ_{33} where the sought signal is buried at $1\,\mathsf{m}$ to $5\,\mathsf{m}$ depth. The threshold for Setup B is computed by (4.17) and presented in Table 4.2. Table 4.3 shows the percentage of the 1000 test runs that correctly detect the sought signal and the percentage of the MF output that is accepted based on Setup A and B, respectively. Furthermore, the empirical POMs and POFs are compared to their theoretical values. The theoretical probabilities are computed from theoretical values only.

The MF simulations show that Setup A and Setup B have an opposite trend. As the sought signal becomes weaker (increase in depth), Setup A accepts fewer MF outputs. Setup B, on the other hand, accepts more MF outputs. Setup B is, therefore, counterintuitive.

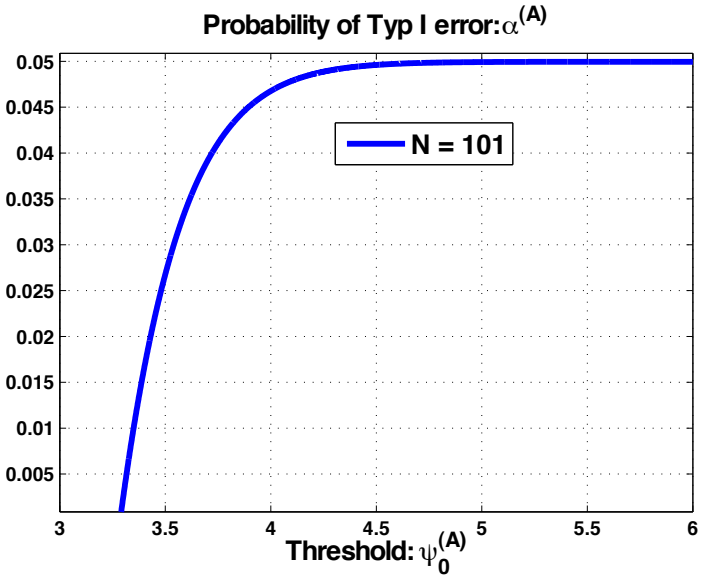

Figure 4.2: Decision Threshold Under Setup A

Depth [m]	1	2	3	4	5
λ [−]	22.996	3.627	1.055	0.517	0.330
$\psi_0^{(B)}$ [−]	21.351	1.983	−0.590	−1.1275	−1.3148

Table 4.2: Decision Threshold Setup B

Depth		[m]	1	2	3	4	5
Detection		[%]	100	84.9	16	10.5	8.6
Setup A	Accept	[%]	100	63.7	6.5	3.9	2.9
	POF	[%]	-	13.2	5.1	3.9	2.9
	POM	[%]	0	27.3	86.3	96.2	95.3
	α	[%]	5				
	β	[%]	0	36.7	98.7	99.7	99.8
Setup B	Accept	[%]	95.5	99.5	100	100	100
	POF	[%]	4.5	0.1	0	0	0
	POM	[%]	-	97.4	100	100	100
	α	[%]	5				
	β	[%]	0	91.2	100	100	100

Table 4.3: Comparison Setup A and Setup B Results

Depth	[m]	1	2	3	4	5
λ	[−]	22.9958	3.6274	1.0551	0.5174	0.3301
$\psi_0^{(B)}$	[−]	22.611	3.241	0.670	0.132	−0.055

Table 4.4: Decision Threshold Setup B ($\alpha^{(B)} = 35\,\%$)

Setup A is more reasonable than Setup B if the error α is set to 5 %. Comparing again the case of 2 m depth, (4.10) leads to $\beta^{(A)} = 36.7\,\%$ and the numerical computation of (4.16) results in $\beta^{(B)} = 91.2\,\%$. However, in order to show that Setup A and B are corresponding to each other, $\alpha^{(B)}$ is now set to 35 % in (4.15) resulting in $\beta^{(B)} = 5.8\,\%$. The corresponding results are listed in Table 4.4 and Table 4.5.

The probabilities in the case of Γ_{33} based on the 2 m depth are presented in Figure 4.3 a) for Setup A and Figure 4.3 b) for Setup B.

Those figures clearly illustrate the asymmetry in the density function of the maximum output compared to the symmetric Gaussian function. The following Figure 4.4 is the same example of Setup B except that $\alpha^{(B)}$ is set to 35 % instead of 5 % (compare (4.17)). In order to evaluate the performance of the likelihood ratio test the Receiver

Depth		[m]	1	2	3	4	5
Detection		[%]	100	84.9	16	10.5	8.6
Setup B	Accept	[%]	63.6	65.1	100	100	100
	POM	[%]	36.4	25.8	0	0	0
	POF	[%]	-	13.9	100	100	100
	α	[%]	35				
	β	[%]	0	5.8	100	100	100

Table 4.5: Setup B Results ($\alpha^{(B)} = 35\,\%$)

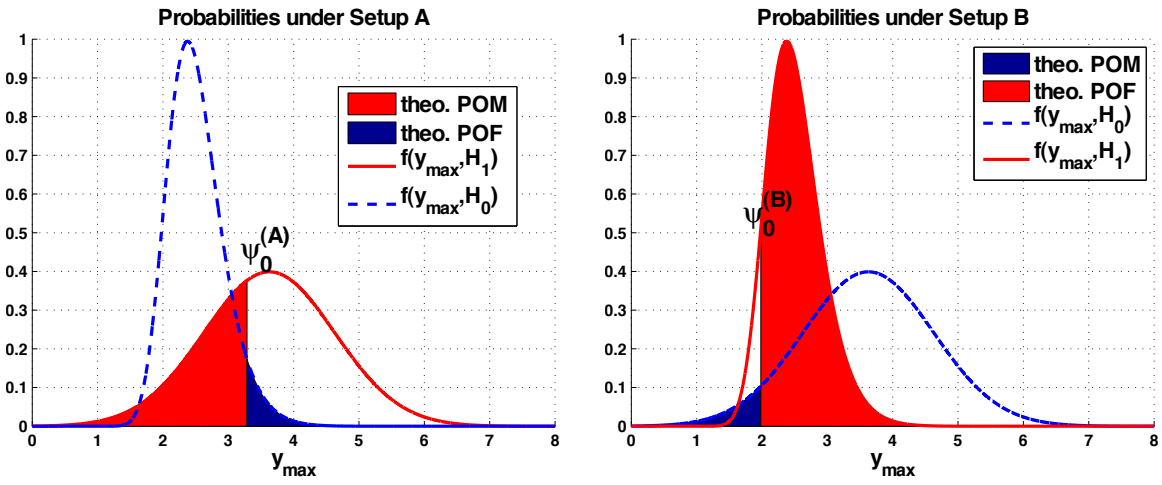

Figure 4.3: Probabilities under a) Setup A b) Setup B

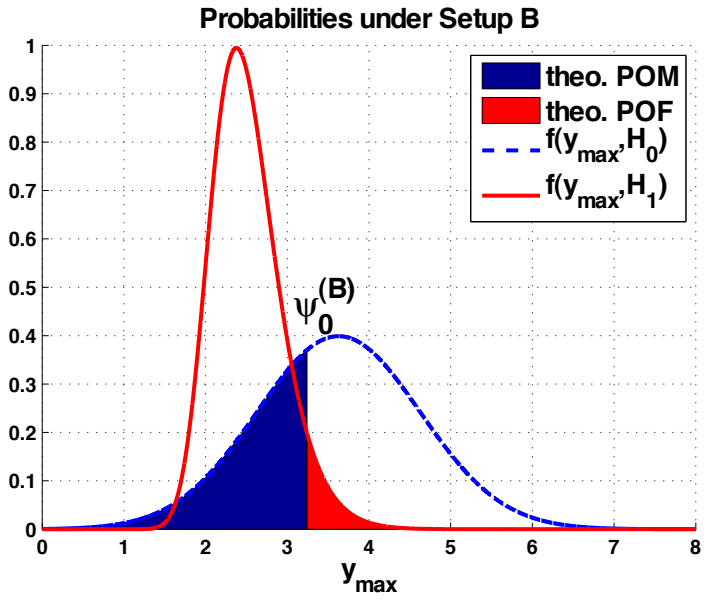

Figure 4.4: Probabilities under Setup B with $\alpha^{(B)}$=35 %

Operating Characteristic (ROC) curves are computed [Kay, 1998, p.74]. The power of the test is thereby defined as $1-\beta$ and plotted against α where α again denotes the probability of a Type I error and β stands for the probability of a Type II error (Table 4.1). Any point on the curve represents, therefore, a specific pair of power and corresponding error probability. It is obvious that in order to receive a stronger power of the test, a higher probability of a Type I error needs to be accepted, i.e. the test significance level increases. The decision threshold ψ_0 corresponds to a certain location on the curve. The ROC curves for the above simulations in Table 4.3 are shown in Figure 4.5. It becomes obvious that Setup A and Setup B are the same and are just mirrored along the diagonal axes of their intersection. Minor differences are caused by the numerical integration in Setup A. If α is a priori defined to be lower than 20 %, Setup A is the more powerful test statistic.

One issue that arises with the presented statistical interpretation is that it cannot easily be applied to the case of multiple tracks described in Section 3.3.6. The probability density function derived from order statistics (4.5) requires that all MF outputs are independently distributed. However, the three profiles are highly correlated in x_2-direction (across-track) and are, therefore, no longer independent. A new statistical analysis is required. Since decorrelation of the three profiles is challenging, a simpler approach is to look at each profile individually for the statistical interpretation.

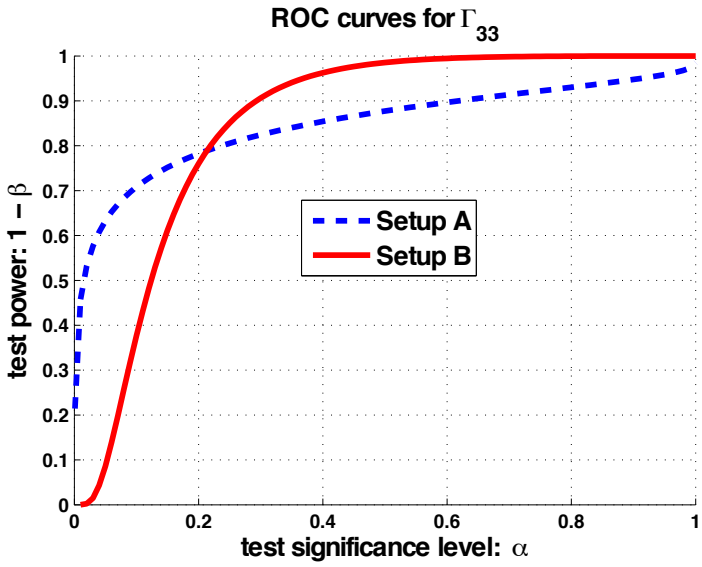

Figure 4.5: Receiver Operating Characteristic Curves for Setup A and B

Chapter 5: Conclusion

The localization of an underground mass anomaly such as a void is an essential task in a broad spectrum of real world applications. Avoiding urban constructions over voids that possibly cause a collapse of land, finding archeological features prior to excavations, and scientific research in caves on Mars, are just some of the purposes that require the beforehand detection of voids. This dissertation is the result of a general study that benefits the entire spectrum. While researchers apply a range of different geophysical sensors, the scope is here only put on the fundamental quantities of the Earth, gravity, gravity gradients, and the magnetic field, which also imply a relatively easy data acquisition. All data are combined as input to a single detection solution. The relationship between gravity, gravity gradients and the magnetic field is here, therefore, mathematically developed, including the derivation of their covariances. The covariance function that describes the geologic background noise is of importance as it is part of the Matched Filter (MF) function. The covariances are either determined by a Power Spectral Density model, derived from covariance propagation, or based on the periodogram method. A detailed description of the simulation setup, as well as the results and statistical interpretations are provided. The focus of this study is the detection using the MF with possible opportunities to estimate selected parameters such as depth and orientation of the anomaly, along with a probabilistic assessment.

The simulations in this dissertation clearly show how the MF is able to detect the mass anomaly modeled as a linear feature in a single profile of observations, even if the background noise is visually predominant. The MF proves to be a promising tool as it correctly locates the sought void not in just one example but in most of the 1000 cases of varying background, where each time the void would not be visible to an operator inspecting the raw data. The rate of successful detections with respect to the number of simulations creates here the major criterion to validate the MF performance.

It is concluded from the output of the simulations that the gravity data are the least effective in comparison to gravity gradients and the magnetic field. The two explanations for that are the relatively high instrument noise of the gravimeter leading to a weak Signal-to-Instrument-Noise ratio and the signal shape of gravity, which is not as sharp as those of its gradients and, therefore, less distinct in the background

noise. The magnetic field data result in a similar strong performance as the gravity gradient data. It has to be noted, though, that magnetic data depend on the direction of magnetization, which can easily be interfered by an outside magnetic source. This research encourages the use of gravity gradiometers as they seem to be advantageous for the detection problem in the shallow subsurface. Combining several gradient components leads to the best result, especially if the sought mass anomaly has a limited extension in each direction of the coordinate system. Adding the magnetic data makes the MF detection even stronger with feasible additional effort, however, it has to be tested if Poisson's Relation is applicable in the specific area. A further finding is that if the background noise provides non-stationary or anisotropic conditions, edge effects may occur in the filter output. In order to avoid this interference the edges of the MF output can be simply eliminated.

The detection of an underground mass anomaly based on gravity and magnetic data poses the geophysical inverse problem, which is non-unique. That means the same observed data can be generated from different kinds of mass anomalies (different shape, depth, density, and so on). This difficulty is sidestepped by utilizing an MF as it requires that the sought signal is known. This additional constraint leads to a unique solution resulting in the localization of the anomaly. Two sets of simulations in this dissertation study the impact on the detection if the sought signal is falsely estimated by modeling either the wrong depth or the wrong orientation in the filter function. This also leads to the question if an unknown depth or orientation can be derived from matched filtering. The two-dimensional filter is designed to find the horizontal location of the mass anomaly but simulations reveal that it is also sensitive to the depth parameter. The depth can be estimated after the horizontal position has been determined. First, the MF is applied to the observations with varying depths in the filter function. The next steps are to determine the horizontal position of the anomaly based on an overview of all MF solutions and to eliminate those solutions that deviate from this horizontal position. The correct depth is finally assumed to be the one with the largest value of the remaining maximum filter outputs.

The MF is less sensitive to a horizontal rotation of the mass anomaly, which is, therefore, difficult to estimate. Simulations show that even if the assumed orientation differs from the true orientation, the MF is still able to locate the anomaly. In order to better delineate the anomaly, i.e. finding its orientation, multiple profiles are necessary. Each of these profiles defines a maximum that represents the center of the anomaly along the corresponding profile. Based on that the orientation of the anomaly can be extracted. If the sought anomaly has a more advanced feature than the simple three-dimensional prism, the anomaly needs to be modeled by an appropriate combination of several prisms. This is outside the scope of this dissertation but poses an interesting task for the ongoing research. If the MF is implemented in order to not only search for the position of the sought signal but also for its unknown orientation, the observation of multiple profiles is useful. In any other case the increase in number

of profiles is not necessarily justified with regard to the additional work caused during data acquisition. The result of each profile is considered almost redundant and is only helpful in the rare examples where the main profile does not locate the anomaly but any of the additional profiles does. It is rather recommended to add magnetic data (or another gravity gradient component) to the original profile than increasing the number of profiles. The contribution to the MF solution in that case is similar but a single profile has the benefit that its MF output can be statistically interpreted with the Neyman-Pearson hypothesis test.

One interesting outcome of this dissertation is the conclusion that the correlation length of the covariance function has in some cases a huge impact on the MF performance. In contrast to the common preprocessing step to whiten, i.e. to decorrelate, the observations, a new approach has been introduced that moves in the opposite direction. By increasing the correlation length of the covariance function, the observations are treated as higher correlated than they actually are. While whitening turns the covariance matrix into a simple diagonal matrix (with appropriate reductions applied to the observations), the new approach results in a covariance matrix with higher off-diagonal elements (cross-covariances). The result is a drastic improvement in the MF performance. The relation between the correlation length and the success of the localization yields an important topic for future research. So far, it can be stated that the drastic effect in the filter output seems to be independent of the variances that are assumed to describe the white instrument noise. Modifying the placing of the observation points along the profile or coping with a large anomaly in the background field influences the overall performance of the detection but does not change the fact that an increase in the correlation length can lead to an enormous improvement of the MF result. As those findings mainly occur with the actual gravity gradient but not so much with the simulated data sets, the next step continuing this research would be the analysis of more real data profiles in various areas. Furthermore, real magnetic data should be included in order to validate the practicality of Poisson's Relation in the real world. The posed question is thereby how large the area is that fulfills the required constant magnetization to density ratio.

The key aspect of future research is, therefore, to focus on actual observations with the background and understandings developed from the simulations in this dissertation. In an overall conclusion, the simulations demonstrate that the MF is a powerful technique and encourage the observation of ground gravity gradients. An even stronger detection performance is gained by combining gravity and magnetic data on a local level.

Appendix A: Covariance Model Parameter

$$\sigma_1^2 = 100000 \, \frac{\mathsf{m}^4}{\mathsf{s}^4} \tag{A.1}$$

$$\sigma_2^2 = 3500 \, \frac{\mathsf{m}^4}{\mathsf{s}^4} \tag{A.2}$$

$$\sigma_3^2 = 778 \, \frac{\mathsf{m}^4}{\mathsf{s}^4} \tag{A.3}$$

$$\sigma_4^2 = 300 \, \frac{\mathsf{m}^4}{\mathsf{s}^4} \tag{A.4}$$

$$\sigma_5^2 = 20 \, \frac{\mathsf{m}^4}{\mathsf{s}^4} \tag{A.5}$$

$$\sigma_6^2 = 0.2 \, \frac{\mathsf{m}^4}{\mathsf{s}^4} \tag{A.6}$$

$$\sigma_7^2 = 0.02 \, \frac{\mathsf{m}^4}{\mathsf{s}^4} \tag{A.7}$$

$$\sigma_8^2 = 0.003 \, \frac{\mathsf{m}^4}{\mathsf{s}^4} \tag{A.8}$$

$$\sigma_9^2 = 3 \cdot 10^{-4} \, \frac{\mathsf{m}^4}{\mathsf{s}^4} \tag{A.9}$$

$$\sigma_{10}^2 = 9 \cdot 10^{-6} \, \frac{\mathsf{m}^4}{\mathsf{s}^4} \tag{A.10}$$

$$\sigma_{11}^2 = 4 \cdot 10^{-7} \, \frac{\mathsf{m}^4}{\mathsf{s}^4} \tag{A.11}$$

$$\sigma_{12}^2 = 4 \cdot 10^{-8} \, \frac{\mathsf{m}^4}{\mathsf{s}^4} \tag{A.12}$$

$$\sigma_{13}^2 = 5 \cdot 10^{-9} \, \frac{\mathsf{m}^4}{\mathsf{s}^4} \tag{A.13}$$

$$\sigma_{14}^2 = 6 \cdot 10^{-11} \, \frac{\mathsf{m}^4}{\mathsf{s}^4} \tag{A.14}$$

$$\sigma_{15}^2 = 5 \cdot 10^{-12} \, \frac{\mathsf{m}^4}{\mathsf{s}^4} \tag{A.15}$$

$$\sigma_{16}^2 = 5 \cdot 10^{-13} \, \frac{\mathsf{m}^4}{\mathsf{s}^4} \tag{A.16}$$

$$\alpha_1 = 3 \cdot 10^{-7} \, \frac{1}{\mathsf{m}} \tag{A.17}$$

$$\alpha_2 = 7.7 \cdot 10^{-7} \, \frac{1}{\mathsf{m}} \tag{A.18}$$

$$\alpha_3 = 3 \cdot 10^{-6} \, \frac{1}{\mathsf{m}} \tag{A.19}$$

$$\alpha_4 = 8.5 \cdot 10^{-6} \, \frac{1}{\mathsf{m}} \tag{A.20}$$

$$\alpha_5 = 2 \cdot 10^{-5} \, \frac{1}{\mathsf{m}} \tag{A.21}$$

$$\alpha_6 = 6 \cdot 10^{-5} \, \frac{1}{\mathsf{m}} \tag{A.22}$$

$$\alpha_7 = 1 \cdot 10^{-4} \, \frac{1}{\mathsf{m}} \tag{A.23}$$

$$\alpha_8 = 2 \cdot 10^{-4} \, \frac{1}{\mathsf{m}} \tag{A.24}$$

$$\alpha_9 = 4.8 \cdot 10^{-4} \, \frac{1}{\mathsf{m}} \tag{A.25}$$

$$\alpha_{10} = 1.3 \cdot 10^{-3} \, \frac{1}{\mathsf{m}} \tag{A.26}$$

$$\alpha_{11} = 3 \cdot 10^{-3} \, \frac{1}{\mathsf{m}} \tag{A.27}$$

$$\alpha_{12} = 5 \cdot 10^{-3} \, \frac{1}{\mathsf{m}} \tag{A.28}$$

$$\alpha_{13} = 1.1 \cdot 10^{-2} \, \frac{1}{\mathsf{m}} \tag{A.29}$$

$$\alpha_{14} = 3 \cdot 10^{-2} \, \frac{1}{\mathsf{m}} \tag{A.30}$$

$$\alpha_{15} = 5 \cdot 10^{-2} \, \frac{1}{\mathsf{m}} \tag{A.31}$$

$$\alpha_{16} = 1.2 \cdot 10^{-1} \, \frac{1}{\mathsf{m}} \tag{A.32}$$

Appendix B: Gravity Gradients and Magnetic Field Covariances

$$\phi_{\Gamma_{11},B_1} = \frac{\mu_0 \chi H}{4\pi G\rho} \left(\alpha\phi_{\Gamma_{11},\Gamma_{11}} + \beta\phi_{\Gamma_{11},\Gamma_{12}} + \gamma\phi_{\Gamma_{11},\Gamma_{13}}\right) \tag{B.1}$$

$$\phi_{\Gamma_{11},B_2} = \frac{\mu_0 \chi H}{4\pi G\rho} \left(\alpha\phi_{\Gamma_{11},\Gamma_{12}} + \beta\phi_{\Gamma_{11},\Gamma_{22}} + \gamma\phi_{\Gamma_{11},\Gamma_{23}}\right) \tag{B.2}$$

$$\phi_{\Gamma_{11},B_3} = \frac{\mu_0 \chi H}{4\pi G\rho} \left(\alpha\phi_{\Gamma_{11},\Gamma_{13}} + \beta\phi_{\Gamma_{11},\Gamma_{23}} + \gamma\phi_{\Gamma_{11},\Gamma_{33}}\right) \tag{B.3}$$

$$\phi_{\Gamma_{22},B_1} = \frac{\mu_0 \chi H}{4\pi G\rho} \left(\alpha\phi_{\Gamma_{22},\Gamma_{11}} + \beta\phi_{\Gamma_{22},\Gamma_{12}} + \gamma\phi_{\Gamma_{22},\Gamma_{13}}\right) \tag{B.4}$$

$$\phi_{\Gamma_{22},B_2} = \frac{\mu_0 \chi H}{4\pi G\rho} \left(\alpha\phi_{\Gamma_{22},\Gamma_{12}} + \beta\phi_{\Gamma_{22},\Gamma_{22}} + \gamma\phi_{\Gamma_{22},\Gamma_{23}}\right) \tag{B.5}$$

$$\phi_{\Gamma_{22},B_3} = \frac{\mu_0 \chi H}{4\pi G\rho} \left(\alpha\phi_{\Gamma_{22},\Gamma_{13}} + \beta\phi_{\Gamma_{22},\Gamma_{23}} + \gamma\phi_{\Gamma_{22},\Gamma_{33}}\right) \tag{B.6}$$

$$\phi_{\Gamma_{33},B_1} = \frac{\mu_0 \chi H}{4\pi G\rho} \left(\alpha\phi_{\Gamma_{33},\Gamma_{11}} + \beta\phi_{\Gamma_{33},\Gamma_{12}} + \gamma\phi_{\Gamma_{33},\Gamma_{13}}\right) \tag{B.7}$$

$$\phi_{\Gamma_{33},B_2} = \frac{\mu_0 \chi H}{4\pi G\rho} \left(\alpha\phi_{\Gamma_{33},\Gamma_{12}} + \beta\phi_{\Gamma_{33},\Gamma_{22}} + \gamma\phi_{\Gamma_{33},\Gamma_{23}}\right) \tag{B.8}$$

$$\phi_{\Gamma_{33},B_3} = \frac{\mu_0 \chi H}{4\pi G\rho} \left(\alpha\phi_{\Gamma_{33},\Gamma_{13}} + \beta\phi_{\Gamma_{33},\Gamma_{23}} + \gamma\phi_{\Gamma_{33}}\right) \tag{B.9}$$

$$\phi_{\Gamma_{12},B_1} = \frac{\mu_0 \chi H}{4\pi G\rho} \left(\alpha\phi_{\Gamma_{12},\Gamma_{11}} + \beta\phi_{\Gamma_{12},\Gamma_{12}} + \gamma\phi_{\Gamma_{12},\Gamma_{13}}\right) \tag{B.10}$$

$$\phi_{\Gamma_{12},B_2} = \frac{\mu_0 \chi H}{4\pi G\rho} \left(\alpha\phi_{\Gamma_{12},\Gamma_{12}} + \beta\phi_{\Gamma_{12},\Gamma_{22}} + \gamma\phi_{\Gamma_{12},\Gamma_{23}}\right) \tag{B.11}$$

$$\phi_{\Gamma_{12},B_3} = \frac{\mu_0 \chi H}{4\pi G\rho} \left(\alpha\phi_{\Gamma_{12},\Gamma_{13}} + \beta\phi_{\Gamma_{12},\Gamma_{23}} + \gamma\phi_{\Gamma_{12},\Gamma_{33}}\right) \tag{B.12}$$

$$\phi_{\Gamma_{23},B_1} = \frac{\mu_0 \chi H}{4\pi G\rho} \left(\alpha\phi_{\Gamma_{23},\Gamma_{11}} + \beta\phi_{\Gamma_{23},\Gamma_{12}} + \gamma\phi_{\Gamma_{23},\Gamma_{13}}\right) \tag{B.13}$$

$$\phi_{\Gamma_{23},B_2} = \frac{\mu_0 \chi H}{4\pi G\rho} \left(\alpha\phi_{\Gamma_{23},\Gamma_{12}} + \beta\phi_{\Gamma_{23},\Gamma_{22}} + \gamma\phi_{\Gamma_{23},\Gamma_{23}}\right) \tag{B.14}$$

$$\phi_{\Gamma_{23},B_3} = \frac{\mu_0 \chi H}{4\pi G\rho} \left(\alpha\phi_{\Gamma_{23},\Gamma_{13}} + \beta\phi_{\Gamma_{23},\Gamma_{23}} + \gamma\phi_{\Gamma_{23},\Gamma_{33}}\right) \tag{B.15}$$

$$\phi_{\Gamma_{13},B_1} = \frac{\mu_0 \chi H}{4\pi G\rho} \left(\alpha\phi_{\Gamma_{13},\Gamma_{11}} + \beta\phi_{\Gamma_{13},\Gamma_{12}} + \gamma\phi_{\Gamma_{13},\Gamma_{13}}\right) \tag{B.16}$$

$$\phi_{\Gamma_{13},B_2} = \frac{\mu_0 \chi H}{4\pi G\rho} \left(\alpha\phi_{\Gamma_{13},\Gamma_{12}} + \beta\phi_{\Gamma_{13},\Gamma_{22}} + \gamma\phi_{\Gamma_{13},\Gamma_{23}}\right) \tag{B.17}$$

$$\phi_{\Gamma_{13},B_3} = \frac{\mu_0 \chi H}{4\pi G\rho} \left(\alpha\phi_{\Gamma_{13},\Gamma_{13}} + \beta\phi_{\Gamma_{13},\Gamma_{23}} + \gamma\phi_{\Gamma_{13},\Gamma_{33}}\right) \tag{B.18}$$

$$\phi_{B_1,\Gamma_{11}} = \frac{\mu_0 \chi H}{4\pi G\rho} \left(\alpha\phi_{\Gamma_{11},\Gamma_{11}} + \beta\phi_{\Gamma_{12},\Gamma_{11}} + \gamma\phi_{\Gamma_{13},\Gamma_{11}}\right) \tag{B.19}$$

$$\phi_{B_1,\Gamma_{22}} = \frac{\mu_0 \chi H}{4\pi G\rho} \left(\alpha\phi_{\Gamma_{11},\Gamma_{22}} + \beta\phi_{\Gamma_{12},\Gamma_{22}} + \gamma\phi_{\Gamma_{13},\Gamma_{22}}\right) \tag{B.20}$$

$$\phi_{B_1,\Gamma_{33}} = \frac{\mu_0 \chi H}{4\pi G\rho} \left(\alpha\phi_{\Gamma_{11},\Gamma_{33}} + \beta\phi_{\Gamma_{12},\Gamma_{33}} + \gamma\phi_{\Gamma_{13},\Gamma_{33}}\right) \tag{B.21}$$

$$\phi_{B_1,\Gamma_{12}} = \frac{\mu_0 \chi H}{4\pi G\rho} \left(\alpha\phi_{\Gamma_{11},\Gamma_{12}} + \beta\phi_{\Gamma_{12},\Gamma_{12}} + \gamma\phi_{\Gamma_{13},\Gamma_{12}}\right) \tag{B.22}$$

$$\phi_{B_1,\Gamma_{23}} = \frac{\mu_0 \chi H}{4\pi G\rho} \left(\alpha\phi_{\Gamma_{11},\Gamma_{23}} + \beta\phi_{\Gamma_{12},\Gamma_{23}} + \gamma\phi_{\Gamma_{13},\Gamma_{23}}\right) \tag{B.23}$$

$$\phi_{B_1,\Gamma_{13}} = \frac{\mu_0 \chi H}{4\pi G\rho} \left(\alpha\phi_{\Gamma_{11},\Gamma_{13}} + \beta\phi_{\Gamma_{12},\Gamma_{13}} + \gamma\phi_{\Gamma_{13},\Gamma_{13}}\right) \tag{B.24}$$

$$\phi_{B_2,\Gamma_{11}} = \frac{\mu_0 \chi H}{4\pi G\rho} \left(\alpha\phi_{\Gamma_{12},\Gamma_{11}} + \beta\phi_{\Gamma_{22},\Gamma_{11}} + \gamma\phi_{\Gamma_{23},\Gamma_{11}}\right) \tag{B.25}$$

$$\phi_{B_2,\Gamma_{22}} = \frac{\mu_0 \chi H}{4\pi G\rho} \left(\alpha\phi_{\Gamma_{12},\Gamma_{22}} + \beta\phi_{\Gamma_{22},\Gamma_{22}} + \gamma\phi_{\Gamma_{23},\Gamma_{22}}\right) \tag{B.26}$$

$$\phi_{B_2,\Gamma_{33}} = \frac{\mu_0 \chi H}{4\pi G\rho} \left(\alpha\phi_{\Gamma_{12},\Gamma_{33}} + \beta\phi_{\Gamma_{22},\Gamma_{33}} + \gamma\phi_{\Gamma_{23},\Gamma_{33}}\right) \tag{B.27}$$

$$\phi_{B_2,\Gamma_{12}} = \frac{\mu_0 \chi H}{4\pi G\rho} \left(\alpha\phi_{\Gamma_{12},\Gamma_{12}} + \beta\phi_{\Gamma_{22},\Gamma_{12}} + \gamma\phi_{\Gamma_{23},\Gamma_{12}}\right) \tag{B.28}$$

$$\phi_{B_2,\Gamma_{23}} = \frac{\mu_0 \chi H}{4\pi G\rho} \left(\alpha\phi_{\Gamma_{12},\Gamma_{23}} + \beta\phi_{\Gamma_{22},\Gamma_{23}} + \gamma\phi_{\Gamma_{23},\Gamma_{23}}\right) \tag{B.29}$$

$$\phi_{B_2,\Gamma_{13}} = \frac{\mu_0 \chi H}{4\pi G\rho} \left(\alpha\phi_{\Gamma_{12},\Gamma_{13}} + \beta\phi_{\Gamma_{22},\Gamma_{13}} + \gamma\phi_{\Gamma_{23},\Gamma_{13}}\right) \tag{B.30}$$

$$\phi_{B_3,\Gamma_{11}} = \frac{\mu_0 \chi H}{4\pi G\rho} \left(\alpha\phi_{\Gamma_{13},\Gamma_{11}} + \beta\phi_{\Gamma_{23},\Gamma_{11}} + \gamma\phi_{\Gamma_{33},\Gamma_{11}}\right) \tag{B.31}$$

$$\phi_{B_3,\Gamma_{22}} = \frac{\mu_0 \chi H}{4\pi G\rho} \left(\alpha\phi_{\Gamma_{13},\Gamma_{22}} + \beta\phi_{\Gamma_{23},\Gamma_{22}} + \gamma\phi_{\Gamma_{33},\Gamma_{22}}\right) \tag{B.32}$$

$$\phi_{B_3,\Gamma_{33}} = \frac{\mu_0 \chi H}{4\pi G\rho} \left(\alpha\phi_{\Gamma_{13},\Gamma_{33}} + \beta\phi_{\Gamma_{23},\Gamma_{33}} + \gamma\phi_{\Gamma_{33}}\right) \tag{B.33}$$

$$\phi_{B_3,\Gamma_{12}} = \frac{\mu_0 \chi H}{4\pi G\rho} \left(\alpha\phi_{\Gamma_{13},\Gamma_{12}} + \beta\phi_{\Gamma_{23},\Gamma_{12}} + \gamma\phi_{\Gamma_{33},\Gamma_{12}}\right) \tag{B.34}$$

$$\phi_{B_3,\Gamma_{23}} = \frac{\mu_0 \chi H}{4\pi G\rho} \left(\alpha\phi_{\Gamma_{13},\Gamma_{23}} + \beta\phi_{\Gamma_{23},\Gamma_{23}} + \gamma\phi_{\Gamma_{33},\Gamma_{23}}\right) \tag{B.35}$$

$$\phi_{B_3,\Gamma_{13}} = \frac{\mu_0 \chi H}{4\pi G\rho} \left(\alpha\phi_{\Gamma_{13},\Gamma_{13}} + \beta\phi_{\Gamma_{23},\Gamma_{13}} + \gamma\phi_{\Gamma_{33},\Gamma_{13}}\right) \tag{B.36}$$

$$\phi_{\Gamma_{11},B} = \alpha\phi_{\Gamma_{11},B_1} + \beta\phi_{\Gamma_{11},B_2} + \gamma\phi_{\Gamma_{11},B_3} \tag{B.37}$$

$$\phi_{\Gamma_{22},B} = \alpha\phi_{\Gamma_{22},B_1} + \beta\phi_{\Gamma_{22},B_2} + \gamma\phi_{\Gamma_{22},B_3} \tag{B.38}$$

$$\phi_{\Gamma_{33},B} = \alpha\phi_{\Gamma_{33},B_1} + \beta\phi_{\Gamma_{33},B_2} + \gamma\phi_{\Gamma_{33},B_3} \tag{B.39}$$

$$\phi_{\Gamma_{12},B} = \alpha\phi_{\Gamma_{12},B_1} + \beta\phi_{\Gamma_{12},B_2} + \gamma\phi_{\Gamma_{12},B_3} \tag{B.40}$$

$$\phi_{\Gamma_{23},B} = \alpha\phi_{\Gamma_{23},B_1} + \beta\phi_{\Gamma_{23},B_2} + \gamma\phi_{\Gamma_{23},B_3} \tag{B.41}$$

$$\phi_{\Gamma_{13},B} = \alpha\phi_{\Gamma_{13},B_1} + \beta\phi_{\Gamma_{13},B_2} + \gamma\phi_{\Gamma_{13},B_3} \tag{B.42}$$

$$\phi_{B,\Gamma_{11}} = \alpha\phi_{B_1,\Gamma_{11}} + \beta\phi_{B_2,\Gamma_{11}} + \gamma\phi_{B_3,\Gamma_{11}} \tag{B.43}$$

$$\phi_{B,\Gamma_{22}} = \alpha\phi_{B_1,\Gamma_{22}} + \beta\phi_{B_2,\Gamma_{22}} + \gamma\phi_{B_3,\Gamma_{22}} \tag{B.44}$$

$$\phi_{B,\Gamma_{33}} = \alpha\phi_{B_1,\Gamma_{33}} + \beta\phi_{B_2,\Gamma_{33}} + \gamma\phi_{B_3,\Gamma_{33}} \tag{B.45}$$

$$\phi_{B,\Gamma_{12}} = \alpha\phi_{B_1,\Gamma_{12}} + \beta\phi_{B_2,\Gamma_{12}} + \gamma\phi_{B_3,\Gamma_{12}} \tag{B.46}$$

$$\phi_{B,\Gamma_{23}} = \alpha\phi_{B_1,\Gamma_{23}} + \beta\phi_{B_2,\Gamma_{23}} + \gamma\phi_{B_3,\Gamma_{23}} \tag{B.47}$$

$$\phi_{B,\Gamma_{13}} = \alpha\phi_{B_1,\Gamma_{13}} + \beta\phi_{B_2,\Gamma_{13}} + \gamma\phi_{B_3,\Gamma_{13}} \tag{B.48}$$

Appendix C: Magnetic Field Covariances

$$\phi_{B_1} = \left(\frac{\mu_0 \chi H}{4\pi G\rho}\right)^2 \left(\alpha^2 \phi_{\Gamma_{11}} + 2\alpha\beta\phi_{\Gamma_{11},\Gamma_{12}} + \beta^2\phi_{\Gamma_{12}} + \gamma^2\phi_{\Gamma_{13}}\right) \tag{C.1}$$

$$\phi_{B_2} = \left(\frac{\mu_0 \chi H}{4\pi G\rho}\right)^2 \left(\alpha^2 \phi_{\Gamma_{12}} + 2\alpha\beta\phi_{\Gamma_{12},\Gamma_{22}} + \beta^2_{\Gamma_{22}} + \gamma^2_{\Gamma_{23}}\right) \tag{C.2}$$

$$\phi_{B_3} = \left(\frac{\mu_0 \chi H}{4\pi G\rho}\right)^2 \left(\alpha^2 \phi_{\Gamma_{13}} + 2\alpha\beta\phi_{\Gamma_{13},\Gamma_{23}} + \beta^2\phi_{\Gamma_{23}} + \gamma^2\phi_{\Gamma_{33}}\right) \tag{C.3}$$

$$\phi_{B_1,B_2} = \left(\frac{\mu_0 \chi H}{4\pi G\rho}\right)^2 \left(\alpha^2 \phi_{\Gamma_{11},\Gamma_{12}} + 2\alpha\beta\phi_{\Gamma_{11},\Gamma_{22}} + \beta^2\phi_{\Gamma_{12},\Gamma_{22}} + \gamma^2\phi_{\Gamma_{13},\Gamma_{23}}\right) \tag{C.4}$$

$$\phi_{B_1,B_3} = \left(\frac{\mu_0 \chi H}{4\pi G\rho}\right)^2 \left(\alpha^2 \phi_{\Gamma_{11},\Gamma_{13}} + 2\alpha\beta\phi_{\Gamma_{11},\Gamma_{23}} + \beta^2\phi_{\Gamma_{12},\Gamma_{23}} + \gamma^2\phi_{\Gamma_{13},\Gamma_{33}}\right) \tag{C.5}$$

$$\phi_{B_1,B} = \alpha\phi_{B_1,B_1} + \beta\phi_{B_1,B_2} + \gamma\phi_{B_1,B_3} \tag{C.6}$$

$$\phi_{B_2,B_1} = \phi_{B_1,B_2} \tag{C.7}$$

$$\phi_{B_2,B_3} = \left(\frac{\mu_0 \chi H}{4\pi G\rho}\right)^2 \left(\alpha^2 \phi_{\Gamma_{12},\Gamma_{13}} + 2\alpha\beta\phi_{\Gamma_{12},\Gamma_{23}} + \beta^2\phi_{\Gamma_{22},\Gamma_{23}} + \gamma^2\phi_{\Gamma_{23},\Gamma_{33}}\right) \tag{C.8}$$

$$\phi_{B_2,B} = \alpha\phi_{B_2,B_1} + \beta\phi_{B_2,B_2} + \gamma\phi_{B_2,B_3} \tag{C.9}$$

$$\phi_{B_3,B_1} = -\phi_{B_1,B_3} \tag{C.10}$$

$$\phi_{B_3,B_2} = -\phi_{B_2,B_3} \tag{C.11}$$

$$\phi_{B_1,B} = \alpha\phi_{B_3,B_1} + \beta\phi_{B_3,B_2} + \gamma\phi_{B_3,B_3} \tag{C.12}$$

$$\phi_{B,B_1} = \alpha\phi_{B_1,B_1} + \beta\phi_{B_2,B_1} + \gamma\phi_{B_3,B_1} \tag{C.13}$$

$$\phi_{B,B_2} = \alpha\phi_{B_1,B_2} + \beta\phi_{B_2,B_2} + \gamma\phi_{B_3,B_2} \tag{C.14}$$

$$\phi_{B,B_3} = \alpha\phi_{B_1,B_3} + \beta\phi_{B_2,B_3} + \gamma\phi_{B_3,B_3} \tag{C.15}$$

$$\phi_B = \alpha^2\phi_{B_1} + 2\alpha\beta\phi_{B_1,B_2} + \beta^2\phi_{B_2} + \gamma^2\phi_{B_3} \tag{C.16}$$

Bibliography

[Abt et al., 2011] Abt, T., Huang, O., and Jekeli, C. (2011). Combination of Local Gravimetry and Magnetic Data to Detect Subsurface Anomalies Using a Matched Filter. *Proceedings of the International Association of Geodesy Scientific Assembly IAG 2009*.

[Allen et al., 2008] Allen, L., Birrell, L., Browski, K., Korth, S., Obermeyer, N., and Tesla, E. (2008). Technologies for the detection and monitoring of clandestine underground tunnels. *Global Innovation and Strategy Center*.

[Benito et al., 1995] Benito, G., Pérez del Campo, P., Guitérrez-Elorza, M., and Sancho, C. (1995). Natural and human-induced sinkholes in gypsum terrain and associated environmental problems in NE Spain. *Environmental Geology*.

[Beres et al., 2001] Beres, M., Luetscher, M., and Olivier, R. (2001). Integration of ground-penetrating radar and micro-gravimetric methods to map shallow caves. *Journal of Applied Geophysics*.

[BGI, 2008] BGI (2008). Final Report, Processing and Acquisition of Air-FTG Data - Vinton Dome. *Bell Geospace, INC.*

[Blakely, 1996] Blakely (1996). *Potential Theory in Gravity Magnetic Applications*. Cambridge University Press.

[Bronshteĭn, 2007] Bronshteĭn, I. N. (2007). *Handbook of mathematics*. Springer, Berlin, 5th edition.

[Burger et al., 2006] Burger, H. R., Sheehan, A. F., Jones, C. H., and Burger, H. R. (2006). *Introduction to applied geophysics: exploring the shallow subsurface*. W.W. Norton, New York.

[Butler, 1984] Butler, D. K. (1984). Microgravity and grvity gradient techniques for detection of subsurface cavities. *Journal of Geophysics*, 49(7).

[Carter et al., 1994] Carter, W., Peter, G., Sasagawa, G., Klopping, F., Berstis, K., Hilt, R., Nelson, P., Christy, G., Niebauer, T., Hollander, W., Seeger, H., Richter, B., Wilmes, H., and Lothammer, A. (1994). New Gravity Meter Improves Measurements. *EOS, Transactions American Geophysical Union*, 75(8):90.

[Chamberlain et al., 2000] Chamberlain, A. T., Sellers, W., Proctor, C., and Coard, R. (2000). Cave Detection in Limestone using Ground Penetrating Radar. *Journal of Archaeological Science*.

[Chicken et al., 2008] Chicken, E., Chalise, P., and Loper, D. E. (2008). Conduit Prevalence in the Woodville Karst Plain. *Geotechnical Special Publication*, (183).

[Crouch et al., 1980] Crouch, T. M., Collins, H. R., and Helgesen, J. O. (1980). Abandoned subsurface coal mines as a source of water for coal conversion in Eastern Ohio.

[Dobbs et al., 2005] Dobbs, M., Pruitt, J., Blume, N., Gregory, D., and Sharp, W. (2005). Matched Filter enhanced fiber-based LIDAR for Earth, Weather and Exploration.

[Dobrin and Savit, 1988] Dobrin, M. B. and Savit, C. H. (1988). *Introduction to geophysical prospecting*. McGraw-Hill Book Co., New York, 4th edition.

[Dumrongchai, 2007] Dumrongchai, P. (2007). *Small Anomalous Mass Detection from Airborne Gradiometry*. PhD thesis, Geodetic Science and Surveying, The Ohio State University.

[El-Qady et al., 2005] El-Qady, G., Hafez, M., Abdalla, M. A., and Ushijima, K. (2005). Imaging Subsurface Cavities using Geoelectric Tomography and Ground-Penetrating Radar. *Journal of Cave and Karst Studies*.

[Evans et al., 2000] Evans, M., Hastings, N., and Peacock, B. (2000). *Statistical Distributions*. Wiley Series in Probability and Statistics. John Wiley Sons, Inc., 3rd edition.

[FHWA, 2005] FHWA (2005). Subsurface Imaging of Lava Tubes – Roadway Applications. *Federal Highway Administration*, (FHWA-CFL/TD-05-005).

[Fishbane et al., 2005] Fishbane, P. M., Gasiorowicz, S., and Thornton, S. T. (2005). *Physics for scientists and engineers*. Pearson Prentice Hall, Upper Saddle River, N.J., 3rd edition.

[Fountain, 1976] Fountain, L. S. (1976). Subsurface cavity detection; field evaluation of gravity, radar, and earth resistivity methods. *Highway Geology Symposium, Orlando, Florida*.

[Ghatge and Waldner, 1991] Ghatge, S. L. and Waldner, J. S. (1991). Detection of an Abandoned Mine Using High-Resolution Geophysical Methods in Randolph Township, Morris County, New Jersey. *New Jersey Geological Survey, Open-File Report*, (OFR 91-1).

[Gritto, 2005] Gritto, R. (2005). Subsurface Void Detection using Seismic Tomographic Imaging. *Geophysical Technologies for Detecting Underground Coal Mine Voids: An Interactive Forum*.

[Gural et al., 2005] Gural, P. S., Larsen, J. A., and Gleason, A. E. (2005). Matched Filter Processing for Asteroid Detection. *The Astronomical Journal*, 130:1951–1960.

[Halliday et al., 2001] Halliday, D., Resnick, R., and Walker, J. (2001). *Fundamentals of Physics*. John Wiley Sons, New York, 6th edition.

[Heath, 2007] Heath, P. (2007). *Analysis of Potential Field Gradient Tensor Data: Forward Modelling, Inversion and Near-Surface exploration*. PhD thesis, The Universtity of Adelaide.

[Heiskanen and Moritz, 1967] Heiskanen, W. A. and Moritz, H. (1967). *Physical geodesy*. W. H. Freeman, San Francisco.

[IAGA, 2010] IAGA (2010). International Geomagnetic Reference Field: the eleventh generation. *Geophysical Journal International*, 183(3):1216–1230.

[Inazaki et al., 2004] Inazaki, T., Yamanaka, Y., Kawamura, S., and Tazawa, O. (2004). High-resolution seismic reflection survey using Land Streamers for near-surface cavity detection. *Proceedings of the 7th SEGJ International Symposium*, pages 427–480.

[Jekeli, 1988] Jekeli, C. (1988). The Gravity Gradiometer Survey System (GGSS). *EOS, Transactions, American Geophysical Union*, 69(8):105, 116–117.

[Jekeli, 2003a] Jekeli, C. (2003a). Formulas for the Gravitational Gradient due to a Rectangular Block. *The Ohio State University*.

[Jekeli, 2003b] Jekeli, C. (2003b). Statistical Analysis of Moving-Base Gravimetry and Gravity Gradiometry. *OSU Report*, (466).

[Jekeli, 2006] Jekeli, C. (2006). Airborne Gradiometry Error Analysis. *Surveys in Geophysics*, 27:257–275.

[Jekeli, 2009] Jekeli, C. (2009). Poisson's Relationship – Space and Frequency Domain Formulations. *The Ohio State University*.

[Jekeli and Abt, 2010] Jekeli, C. and Abt, T. (2010). The Statistical Performance of the Matched Filter for Anomaly Detection Using Gravity Gradients. *OSU Report*, (494).

[Jekeli and Abt, 2011] Jekeli, C. and Abt, T. (2011). Locating Anomalies by Gravity Gradiometry using the Matched Filter with a Probabilistic Assessment. *Studia Geophysica et Geodaetica*, 55(1):1–19.

[Jekeli et al., 2011] Jekeli, C., Huang, O., and Abt, T. (2011). Local and Regional Comparisons of Gravity and Magnetic Fields. *Proceedings of the International Association of Geodesy Scientific Assembly IAG 2009*.

[Kay, 1998] Kay, S. M. (1998). *Fundamentals of statistical signal processing*. Prentice-Hall PTR, Englewood Cliffs, N.J.

[Keating, 1995] Keating, P. (1995). A simple technique to identify magnetic anomalies due to kimberlite pipes. *Exploration and Mining Geology*, 4:121–125.

[Linford, 1998] Linford, N. (1998). Geophysical survey at boden vean, cornwall, including an assessment of the microgravity technique for the location of suspected archaeological void features. *Archaeometry*.

[Luke et al., 1997] Luke, B. A., Begley, C. T., Chase, D. S., Ross, A. J., and Brady, J. E. (1997). Rapid-Response Geophysical Site Investigations at a pre-Columbian Settlement in Honduras. *Symposium on the Application of Geophysics to Engineering and Environmental Problems*, 2.

[Luke and Chase, 1997] Luke, B. A. and Chase, D. S. (1997). Detecting caves using seismic surface waves: A feasibility study. *University of Nevada Las Vegas, Nev., USA*.

[Lundberg and Gu, 1999] Lundberg, M. and Gu, I. Y. H. (1999). A 3-D matched filter for detection of land mines using spatio-temporal thermal modeling. *Department of Signals and Systems, Chalmers University of Technology, Sweden*.

[McCann et al., 1987] McCann, D., Jackson, P., and Culshaw, M. (1987). The use of geophysical surveying methods in the detection of natural cavities and mineshafts. *Journal of Geology and Hydrogeology, Geological Society of London*.

[Middleton, 1960] Middleton, D. (1960). *An Introduction to Statistical Communication Theory*. International Series in Pure and Applied Physics. McGraw-Hill Book Company, Inc.

[Mochales et al., 2008] Mochales, T., Casas, A., Pueyo, E., Pueyo, O., Román, M., Pocovi, A. Soriano, M., and Ansón, D. (2008). Detection of underground cavities

by combining gravity, magnetic and ground penetrating radar surveys: a case study from the Zaragoza area, NE Spain. *Environmental Geology*.

[Moritz, 1989] Moritz, H. (1989). *Advanced Physical Geodesy*. Wichmann, Karlsruhe, 2nd edition.

[Munk and Sheets, 1997] Munk, J. and Sheets, R. A. (1997). Detection of Underground Voids. *U.S. Geological Survey, Water-Resources Investigations*, (Report 97-4221).

[Murphy, 2004] Murphy, C. A. (2004). The Air-FTG airborne gravity gradiometer system. *ASEG-PESA, Airborne Gravity 2004 Workshop, Geoscience Australia*.

[Naudy, 1971] Naudy, H. (1971). Automatic Determination of Depth on aeromagnetic Profiles. *Journal of Geophysics*, 36(4).

[Nevzorov, 2001] Nevzorov, V. B. (2001). Mathematical Theory. *Translations of Mathematical Monographs, American Mathematical Society*, 194.

[Niebauer et al., 1995] Niebauer, T., Sasagawa, G., Faller, J., Hilt, R., and Kloppin, F. (1995). A New Generation of Absolute Gravimeters. *Metrologia*, 32:159–180.

[Parasnis, 1997] Parasnis, D. S. (1997). *Principles of applied geophysics*. Chapman and Hall, London, 5th edition.

[Poisson, 1826] Poisson, S. (1826). Mémoire sur la théorie du magnétisme. *Mémoires de l'Académie Royale des Sciences de l'Institut de France*, pages 247–348.

[Reigber et al., 2003] Reigber, C., Lühr, H., and Schwintzer, P. (2003). *First CHAMP Mission Results for Gravity*. Magnetic and Atmospheric Studies.

[Romaides et al., 2001] Romaides, A. J., Battis, J. C., Sands, R. W., Zorn, A., Benson Jr, D. O., and DiFrancesco, D. J. (2001). A comparison of gravimetric techniques for measuring subsurface void signals. *Journal of Physics D: Applied Physics*.

[Rummel et al., 2000] Rummel, R., Müller, J., Oberndorfer, H., and Sneeuw, N. (2000). Satellite Gravity Gradiometry with GOCE. *IAG Symposium 120*, pages 66–72.

[Rybakov et al., 2005] Rybakov, M., Rotstein, Y., Shirman, B., and Al-Zoubi, A. (2005). Cave detection near the Dead Sea – a micromagnetic feasibility study. *The Leading Edge*.

[SCINTREXLimited, 1997] SCINTREXLimited (1997). CG-5 Scintrex Autograv System. *Operation Manual*, (867700).

[Sharma, 1976] Sharma, P. (1976). *Geophysical methods in geology*. Elsevier Scientific Publishing Company.

[Sharma, 1997] Sharma, P. (1997). *Environmental an engineering geophysics*. Cambridge University Press.

[Sogade et al., 1999] Sogade, J., Vichabian, Y., and Morgan, F. D. (1999). Induced polarization in the detection of cave systems. *Proceedings of SAGEEP*.

[Srinivasan, 2002] Srinivasan, R. (2002). *Importance Sampling: Applications in Communications and Detection*. Springer.

[Styles et al., 2005] Styles, P., McGrath, R., Thomas, E., and Cassidy, N. (2005). The use of microgravity for cavity characterization in karstic terrains. *Journal of Engineering Geology and Hydrogeology*.

[Tapley et al., 2004] Tapley, B., Bettadpur, S., Watkins, M., and Reigber, C. (2004). The Gravity Recovery and Climate Experiment: Mission Overview and Early Results. *Geophysical Research Letters*, 31(L09607).

[Telford et al., 1990] Telford, W., Geldart, L., Sheriff, R., and Keys, D. (1990). *Applied Geophysics*. Cambridge University Press.

[Torge, 1989] Torge, W. (1989). *Gravimetry*. W. de Gruyter, Berlin.

[Torge, 2001] Torge, W. (2001). *Geodesy*. W. de Gruyter, Berlin, 3rd completely rev. and extended edition.

[Vichabian and Morgan, 2002] Vichabian, Y. and Morgan, F. D. (2002). Self potentials in cave detection. *Massachusetts Institute of Technology*.

[White et al., 1983] White, J., Sailor, R., Lazarewicz, A., and Leschack, A. (1983). Detection of seamount signatures in SEASAT altimeter data using matched filters. *Journal of Geophysical Research*, 88(C3):1541–1551.

[Wynne et al., 2009] Wynne, J. J., Titus, T. N., Diaz, G. C., Colpitts, C., Hicks, W. L., Hill, D., Ruby, D. W., and Tambley, C. (2009). Cave Microclimate Data Retrieval and Volumetric Mapping, 2009 Atacama Desert Expedition, Chile, Earth-Mars Cave Detection Project. *Explorers Club Flag Report*.

[Zebker, 2000] Zebker, H. A. (2000). Studying the Earth with Interferometric Radar. *Earth System Science, IEEE*.